MELLANIE NABAK ROCHA

EXPERIMENTAL ANALYSIS OF COLD WORK IN AN OVERLAP JOINT OF ALUMINUM ALLOY FOR A WING-TO-WING ASSEMBLY

FEDERAL UNIVERSITY OF UBERLANDIA
MECHANICAL ENGINEERING FACULTY
UNDERGRADUATE COURSE IN AERONAUTICAL ENGINEERING
2018

MELLANIE NABAK ROCHA

EXPERIMENTAL ANALYSIS OF COLD WORK IN AN OVERLAP JOINT OF ALUMINUM ALLOY FOR A WING-TO-WING ASSEMBLY

Final graduation thesis submitted to the faculty of Undergraduate Program of Aeronautical Engineering at Federal University of Uberlandia in partial fulfillment of the requirements for the degree of **BACHELOR IN AERONAUTICAL ENGINEERING**.

Advisor: Professor Ruham Pablo Reis, PhD.
Coadvisor: Professor Núbia dos Santos Saad, PhD.

UBERLANDIA, MG
2018

MELLANIE NABAK ROCHA

EXPERIMENTAL ANALYSIS OF COLD WORK IN AN OVERLAP JOINT OF ALUMINUM ALLOY FOR A WING-TO-WING ASSEMBLY

Final graduation thesis **APPROVED** by the examiners of the Undergraduate Program of Aeronautical Engineering for the fulfillment of the requirements for the degree of Bachelor in Aeronautical Engineering. It was judged and approved at its final form.

Examiners:

_____

Prof. Ruham Pablo Reis, PhD. – FEMEC/UFU – Advisor

_____

Prof. Núbia dos Santos Saad, PhD. – FEMEC/UFU – Coadvisor

_____

Prof. Tobias Souza Morais, PhD. – FEMEC/UFU

Uberlandia, November 26th, 2018.

I dedicate this work to my family, who made everything possible in my life.

ACKNOWLEDGEMENTS

I would like to thank God for giving me an amazing life, and my parents, who stood by me during my time at college, even far away. They are my inspiration to be a better person and a great professional.

I want to say thank you to all my colleagues and friends, from CSULB, UFU and USP, who gave me support and courage to go further during my time at each university. I would like to say a special thanks to Juliana Amorim, for all the time dedicated reviewing my papers and to the 7th aeronautical engineering class of UFU, for being the best.

For the engineers of EMBRAER, I want to say this experiment became a reality only because of you. I want to especially thank Alexandre Roschel, Flávio Cremonezi, Frederico Kawano, Marcelo Corbani, Orlando Henrique and Zeeshan Burhani for the opportunities, support, and unmeasurable help offered to me.

Finally, I want to thank my advisors, Núbia Saad and Ruham Reis, for all your dedication making this experiment attainable. Thank you for all the patience and guidance.

ROCHA, M. N. **Experimental analysis of cold work in an overlap joint of aluminum alloy for a wing-to-wing assembly.** 2018. 107 p. Final graduation thesis – Undergraduate Program of Aeronautical Engineering at Federal University of Uberlandia, MG.

RESUMO

Cold work é uma ferramenta utilizada para o aumento da vida em fadiga de componentes aeronáuticos através da geração de tensão residual pelo encruamento de grãos na região de descontinuidades em uma peça. Formas tradicionais de cold work são aplicadas em larga escala na indústria aeronáutica, mas demandam tempo produtivo para sua execução. Estudos recentes apontam o cold work causado pelo próprio prendedor, com mudança de classe de furação em furos de juntas estruturais, como tendo resultado similar ou até mesmo superior que o do cold work tradicional. Desta forma, este experimento foi realizado utilizando Método de Elementos Finitos do software CATIA®, comparação bibliográfica e ciclagem de fadiga, visando comprovar o ganho de vida em fadiga esperado ao se aplicar o cold work em uma classe especial de furação, com pinos do tipo Pull-Stem em uma junta sobreposta – fidedigna à junção asa-asa de uma aeronave EMBRAER – em comparação com a mesma junta com pinos do tipo Hi-Lite.

Palavras-chave: classe de furação, cold work, juntas, método de elementos finitos, tensão residual, vida em fadiga.

ROCHA, M. N. **Experimental analysis of cold work in an overlap joint of aluminum alloy for a wing-to-wing assembly.** 2018. 107 p. Final graduation thesis – Undergraduate Program of Aeronautical Engineering at Federal University of Uberlandia, MG.

ABSTRACT

Cold work is a method used to increase the fatigue life in aeronautical components, through the residual stress creation. This is a result of grain hardening on the discontinuity area. Traditional cold work approaches are largely applied on aeronautical industry but demand excessive time to be completed. Recent studies have shown that the cold work caused by the fastener riveting, along with drilling class changes presented similar or superior results than the traditional cold work forms for structural joints. Therefore, this experiment was performed using Finite Element Model of software CATIA®, literature comparison, and fatigue cycling, to prove that cold work applied on a special drilling class with Pull-Stem pins in an overlap joint – similar to a wing-to-wing assembly of an EMBRAER aircraft – could result in the expected fatigue life improvement, in comparison to the same joint with Hi-Lite pins.

Keywords: cold work, drilling class, fatigue life, finite element model, joints, residual stress.

LIST OF FIGURES

LIST OF TABLES

LIST OF SYMBOLS AND ACRONYMS

AC	Advisory Circulars	
AD	Airworthiness Directives	
m	Allowable minimum margin between rivet and plate border	[mm]
s_s	Allowable shear stress of rivet	$[N/mm^2]$
s_t	Allowable tensile stress of plate	$[N/mm^2]$
N_i	Average number of cycles to failure	
θ	Bearing distribution factor	
K_{th}	Bearing stress concentration factor	
$\boldsymbol{F_{BP}}$	Bypass force	[N]
P	Bypass load	[N]
CAD	Computer-aided design and drafting	
$^{e}/_{d}$	Edge distance ratio	[mm/mm]
K_{eff}	Effective stress intensity factor	
EMBRAER	Empresa Brasileira de Aeronaves	
EASA	European Aviation Safety Agency	
D	Fastener diameter	[mm]
α	Fastener hole condition factor	
FAA	Federal Aviation Administration	
FEM	Finite Element Model	
$\boldsymbol{F_0}$	Force applied on plates	[N]
C	Fraction of life consumed	
HST	HI-LITE pins	
HST	HI-LOKE pins	
β	Hole filling factor	
LOV	Limits of Validity	
ΔP	Load transfer through fastener	[N]
$\boldsymbol{F_{LT}}$	Load-Transfer force	[N]
σ_2	Local stress caused by bypass load	$[N/mm^2]$
σ_1	Local stress caused by load transfer	$[N/mm^2]$
CATIA®	Multi-platform software suite for CAD, CAE & CAM	

MED	Multiple-element damage	
MSD	Multiple-site damage	
n_i	Number of cycles accumulated at stress	
p	Pitch	[mm]
t	Plate thickness	[mm]
ν	Poisson Coefficient	
HSL	PULL-STEM pins	
σ	Reference stress in the structure	$[N/mm^2]$
K_{res}	Residual stress intensity factor	
SB	Service Bulletins	
SF	Severity Factor	
A_0	Specimen cross-sectional area	$[mm^2]$
L_0	Specimen length	[mm]
ϵ_e	Strain	[mm/mm]
K_{tg}	Stress concentration factor	
K_{app}	Stress intensity factor caused by external applied load	
σ_{ij}	Tensile load mods	$[N/mm^2]$
ΔK_f	Variation in the effective stress intensity factor	
WFD	Widespread Fatigue Damage	
W	Width of the plate	[mm]
E	Young's modulus	$[N/mm^2]$

TABLE OF CONTENTS

1 INTRODUCTION

Since the accident with Aloha Airlines flight 243 in 1988, which caused the fuselage to lose huge sections, as shown in Figure 1, the fatigue life of structural components in the aeronautical field and widespread fatigue damage had started being widely studied. New materials and manufacturing processes were introduced as a solution to increase the fatigue life through basic fatigue and fracture mechanics studies. Ever since, many different experiments have been conducted to analyze how the performance of structural components have been affected. A relatively new one, the cold work, is a promising fatigue life improver process that may present relative improvements of 28 times the regular drilling process (Yucan, 2015).

Figure 1- Aloha airlines Boeing 737-200 N73711 - flight 243 - after accident. Source: Aerotime News Hub, 2017.

The cold expansion is an innovative manufacturing process that look towards the fatigue life improvement for structural drilled components. It allows an increase of residual

compressive stresses around the holes of a plate, due to the higher interference caused by the process.

1.1 Motivation

In order to implement riveted or bolted joints, the components need to be drilled to create fastener holes, which causes geometrical discontinuities and entail local stress (or strain) concentration during loading. Investigations showed that there were several accidents caused by fatigue failures initiating from fastened joints. According to statistics, fatigue fractures of fasten holes account for 50‑90% of fractures of aging planes (Yucan, 2015).

One of the primary challenges is to increase the residual compressive stress in order to improve the fatigue life. Nonetheless, this type of stress is proportional to the design properties of the drilled component. Due to main bearing structures size and cycling loads life, they present a great need for safety and fatigue resistance, which makes the improvement more desirable. The cold work process may be a potential solution to increase the residual stresses, extend the aircraft's fatigue life, increase the component fatigue life, and prevent early crack initiation.

Moreover, the cold work was discovered as a method that can be created while the fasteners are being installed, due to its own riveting process. It can reduce the productive time by eight minutes per hole (EMBRAER, 2018). Implementing this change could guarantee more endurance to the process while the benefits of cold work will still be effective.

The rivets chosen for the project were PULL-STEM Pins and HI-LITE Pins, already in use for the selected program due to their installation method, which reduces damages to the structural components. In both cases analyzed, the same diameter fastener was used but the normative charter guarantees different ranges for each. However, the same loads were applied for the tests and improvement was noted for the cold work process, achieved through the riveting process in comparison to the lack of cold work. The prototypes were shown in Figure 2.

Figure 2 - Specimens model after done. Source: author.

1.2 Objectives

The primary objective of this experiment was to analyze how the cold expansion through the drilling process affects the fatigue life of an overlapping riveted joint made of 7050 enriched aluminum alloy.

Other specific goals are:

1. Analyze, by means of fatigue experiments, the effects of different riveted joints;

2. Understand the cold expansion effect;

3. Compare the experimental conclusions with previous conclusions on the literature.

The main object of this experiment is to offer an innovative solution to reduce the negative effects of the drilling process on components of aircraft structures, by modifying their cold work manufacturing process.

Once all the parameters were determined, the next step was to construct the specimens. Two different configurations were selected to analyze the influence of different hole diameters and manufacturing paths on the component. This process aimed at finding the best configuration comparing the data collected in all the cases.

After the manufacture of those configurations, they were tested in a tensile test machine at the Laboratory of Mechanical Structures, LMEst, at Federal University of Uberlandia, UFU, Mechanical Engineering Faculty, FEMEC.

1.3 Structure of the work

In the following, Chapter 2 presents a summary of the main structural and manufacturing concepts applied on this work, also the literature review of previous works about Cold expansion.

Chapter 3 brings cases of interest that conducted to the actual studies, airworthiness directives, and development on fatigue life of aeronautical parts.

Chapter 4 presents the finite element simulation, through Software CATIA®, and the methodology applied.

Chapter 5 consists on the description of the materials and methods used to develop this work, the construction of the models, the experimental features, and the techniques used, while Chapter 6 exhibit the series of results acquired through the measurements, and the related discussions.

Finally, Chapter 7 consists on the summary of the conclusions obtained after completing all the tests and the suggestions for future work, followed by the references and the appendices.

2 LITERATURE SURVEY

2.1 Structures Background

2.1.1 Joints

A joint is the spot between two or more plates attached. The common types of joints are: top joints, angle joints, corner joints, edge joints, and overlapping joints. For the last one, it is regular to find single, double or butt joints, in the specific case of bolted joints. They are represented in Figure 3.

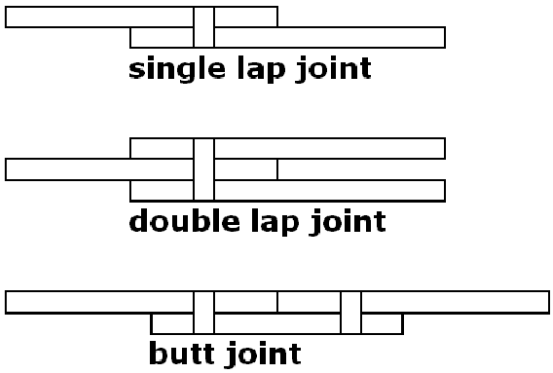

Figure 3 - Usual types of Overlapping Bolted Joints. Source: Wythers, 2012.

In aircraft structures, three types of joints are used, namely, mechanically fastened joints, adhesively bonded joints, and welded joints (Yucan, 2015). In addition, they are commonly top or overlapping joints. Their main objective is to resist the forces applied on them, also transfer efforts, attending to the needs they were projected to (Xavier, 2006).

Despite the kind of joint chosen, it is important to remember they have to be cautiously designed to guarantee a great fatigue life for the components they attach. Thus, the joint has to avoid excessive stress concentration that leads to crack propagation. It happens due to the drilling process to join the plates.

In this work, the joint chosen was an overlapping one – in which case the boundary of metal plates contains a middle plane created by a continuous surface between the edges of the overlapped plates. The material picked was 7050 enriched Aluminum alloy with T7451 heat treatment – it means that the plate was solution heat-treated, stress-relieved by controlled stretching from 1.5% to 3%, and naturally aged –, and the plates were put together as a mechanically fastened joint by four rivets. The model design, presented in Figure 4 below, is a reference to the specimen used during the destructive tests.

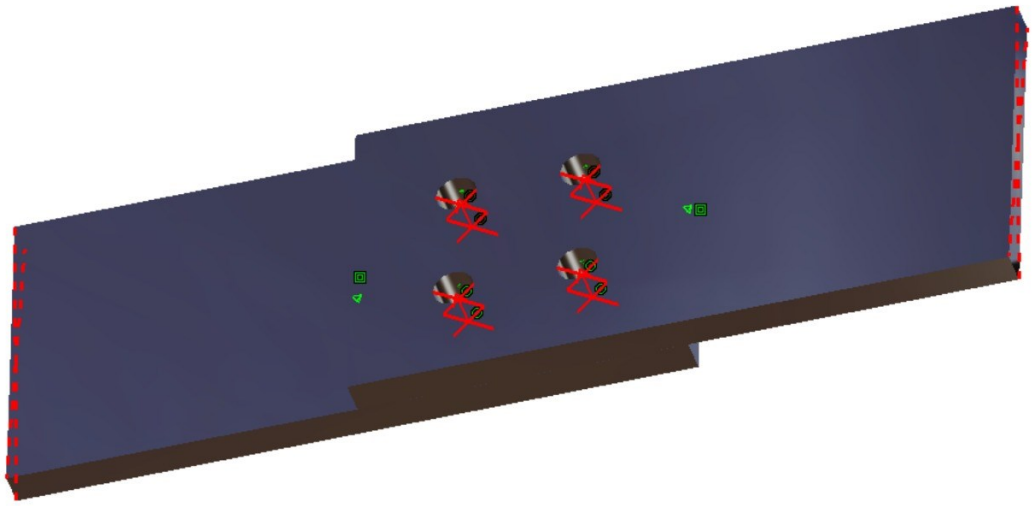

Figure 4 - Specimen model. Source: author.

This representation required the software CATIA® to be done – a CAD simulation-based software –, and presents the joint of two aluminum alloy plates, through pulled rivets, available for simulation in the software platform.

It is important to remark the mainly parameters for drilled plates, as shown in Figure 5, in which:

- h is the thickness of the plate;
- d is the hole diameter;
- e is the distance from the hole center to the specimen boundary along the width direction;
- $^{e}/_{d}$ is the edge distance ratio.

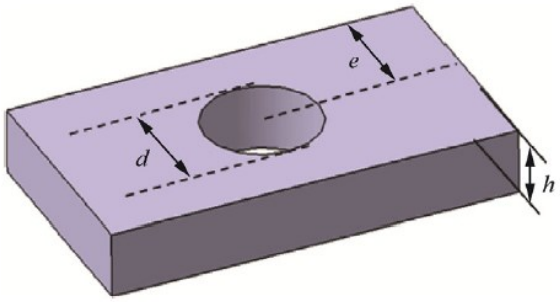

Figure 5 - Main dimensions of a part with a hole. Source: Yucan, 2015.

2.1.2 Fasteners and load transfer

With the special requirements on safety and durability, mechanical connection including bolts and rivets is still the dominant connection mechanism in primary aircraft structural components (Skorupa, 2014).

Fasteners are commonly used in the aeronautical field to attach structures, acting like load transfer elements. The aerospace industry utilizes all sort of standard fastener types, including screws, rivets, bolts, pins and collars. For the specific use of rivets, there are three main types, known as solid rivets, full tubular rivets, and semi-tubular rivets, which can be broken down into several configurations (IEEE, 2018).

Solid rivets have solid shafts with no internal cavities. This rivet type is more difficult to attach than the others and requires powered machinery to insert. Moreover, tubular rivets have a coaxial cylindrical hole in the headless end. In this case, the riveting process does not require a pre-drilled hole. Finally, semi-tubular rivets have a coaxial cylindrical or tapered hole in the end opposite the head. They require much less insertion force and are used in impact riveting applications (IEEE, 2018).

Furthermore, aeronautical applications can commonly use split rivets, blind rivets, compression rivets, and drive rivets, as an alternative to the solid rivets. The first has two shanks that are spread apart once the rivet has been inserted; the second one is used when the rivet is not accessible from both sides; the third is formed by female and male halves, which are placed in a pre-drilled hole, with each half on a different side; and the last has a pin that protrudes through the head of the rivet (IEEE, 2018).

Along with the rivet type, there are different riveting processes that interfere on the manufacture of the structural part. According to IEEE, 2018, there are three main types of riveting: compression, impact, and nonimpact riveting. In compression riveting, the head of the rivet is formed as a result of pulling or squeezing the rivet shank. In impact riveting, an impacting to the top of the shank forms the head of the rivet, often achieved using riveting hammers. Finally, in the nonimpact type, a rolling or spinning action to the end of top of the shank forms the head of the rivet.

Accordingly to the utilization on the aeronautical field, also the interference desired, there are some types of rivets and pins most commonly applied. The interference fit is a consequence of forced installation of a fastener that has a shank purposely larger than the hole it is intended for, which increases significantly the fatigue resistance of assembled structures subject to alternative loading (LISI, 2018).

For cases where there is a need for clearance, or low interference fit throughout the aircraft, from wings to fuselage, or in engine fairings, the HI-LITE pins are applied. This sort of pin is an evolution from HI-LOK pins, and has been strongly used for one-side assemblies in the aerospace industry (LISI, 2018). Figure 6 shows the comparison between the HI-LITE and HI-LOK pins.

Figure 6 - HI-LITE and HI-LOK pins. Source: LISI, 2018.

It is possible to notice that the HI-LITE saves weight for the parts where it is being applied, since its size is reduced from the size of the HI-LOK pin. Accordingly to LISI, 2018, it is possible to notice a weight saving up to 13% in comparison to the previous generation models. Moreover, its assembly is done by inserting the pin with a collar onto the piece it will mate, providing a precise diameter that accommodates insertion of the pin through the prepared hole to normal interference levels. Figure 7 illustrates this process.

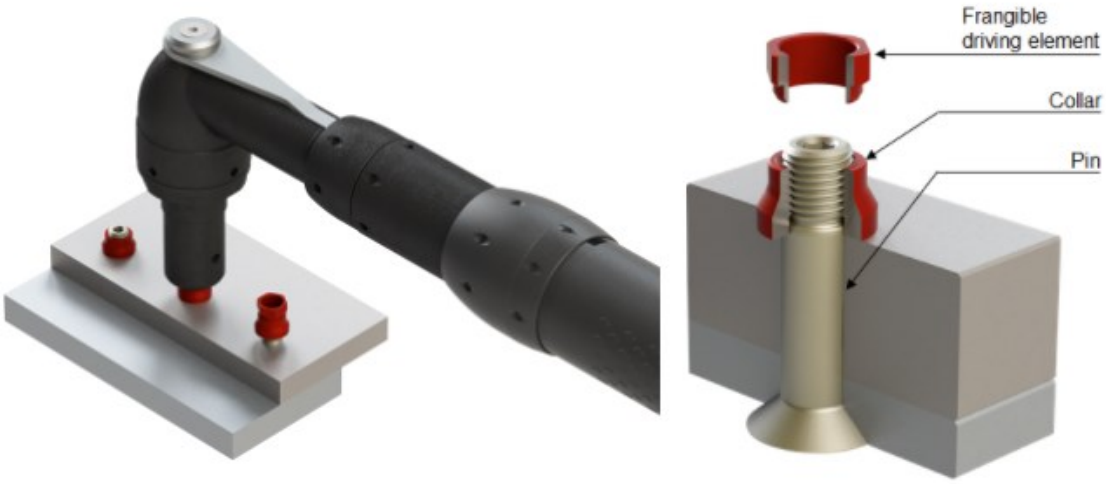

Figure 7 - HI-LITE pin installation using conventional power tool. Source: LISI, 2018.

For the case of rivets and pins on huge parts, or width structural components, the most used are PULL-STEM, HSL, and PULL-IN, HPL, that have been developed for average and high interference fit applications. In both cases, their design guarantees a lack of clamping, scratching, and further damages to the structure during the riveting process. It happens through

the pull mechanism applied on these fasteners. Figure 8 shows an example of these uses for a specific case of a wing-to-wing assembly.

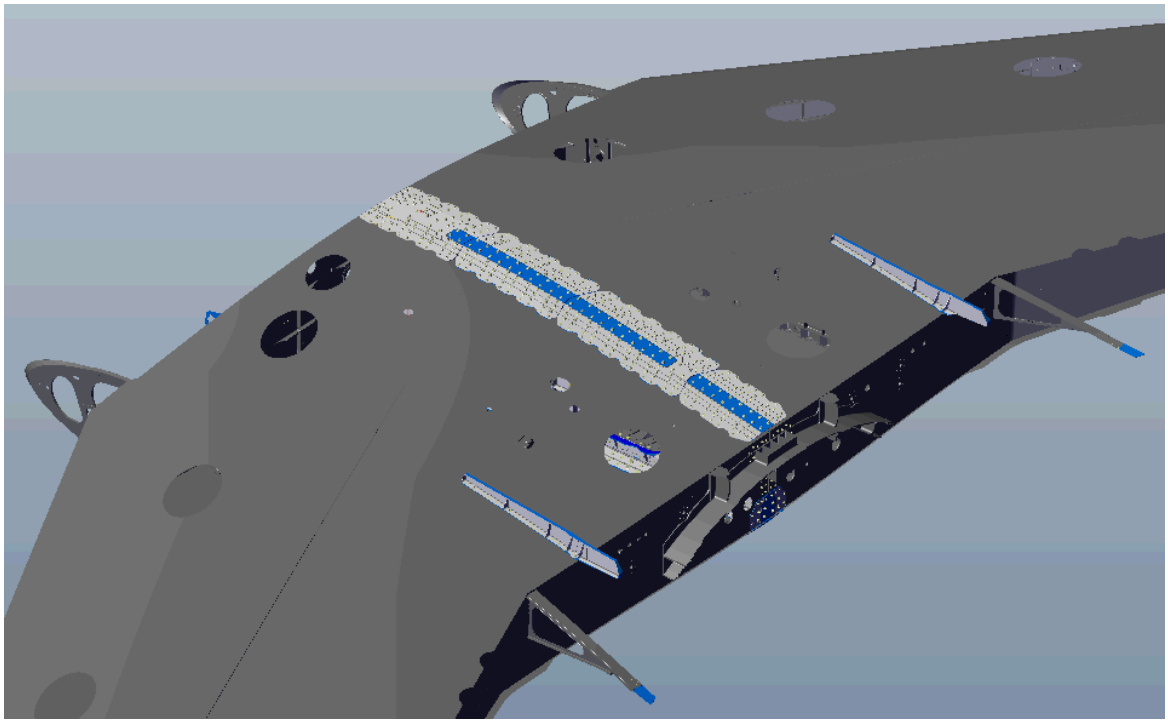

Figure 8 - Wing-to-wing assembly through the use of fasteners. Source: EMBRAER, 2018.

On the other hand, while using the traditional method of riveting the fasteners, through impact, the chances of clamping, scratching, and damaging the structural components were high. Thus, to avoid these problems, heavy machinery is used to pull these pins inside the hole, providing a solution for shear applications and high loaded structure junctions (LISI, 2018).

In this work, the joints were separated in two types, according to the pins used and the interference level achieved. Thus, for the first half of the cases, PULL-STEM rivets HSL1416NKA12-9, made of Titanium alloy 6Al-4V were used, and HI-LITE rivets HST12BJ-12-9, made of Titanium alloy 6Al-4V, for the other half. Figure 9 shows the sample of HSL and HPL pins, similar to the ones chosen for the construction of the first half the specimens. The Appendixes A and B brings the datasheet information about HSL and HST pins, respectively.

Figure 9 – HSL and HPL samples. Source: LISI, 2018.

It is important to remark the fasteners mainly parameters, which are described below and illustrated in Figure 10:

- *Max grip* represents the length of the shank;
- *Grip + B* represents the length of the shank plus the pin head length;
- *ØD* represents the shank diameter;
- *ØA* represents the head diameter;
- *H* represents the pin head length.

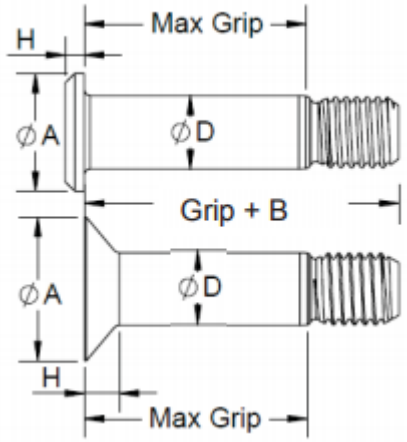

Figure 10 - Main dimensions for HSTR/HLR Protruding and Flush Head pins. Source: LISI, 2018.

Wronicz and Kaniowski, 2016, analyzed rivet parameters that influence the residual stress on the plate and the component structure. Using some process specifications, they related the rivet shape, clearance between the rivet shank and the hole, and distance from the rivet to the compressive stresses generated around the hole.

Joints attached by bolts, to transfer axial loads, or by rivets, to transfer shear loads, are commonly applied in aeronautical structures. The transfer of forces acting on the joints, when

submitted to tension on the longitudinal axis, represented in Figure 11, happens through three different modes:

- Squeeze of the rivet body against the hole walls;
- Friction between the plates contact surfaces on the region under rivet compression influence;
- Friction generated due to the contact between plates.

Figure 11 - Tensile loading acting on longitudinal axis of a specimen. Source: Xavier, 2006.

This way, applying the Force $\boldsymbol{F_0}$ on the plates, the forces $\boldsymbol{F_{BP}}$ and $\boldsymbol{F_{LT}}$ start acting. These forces are, respectively, Bypass Force – transferred straight through friction caused by contact between plates –, and Load-transfer force – sum of the force transferred through rivet squeeze against the hole walls and the friction force due to the plates contact on the spot under rivet compression influence –. Figure 12 represents these acting forces.

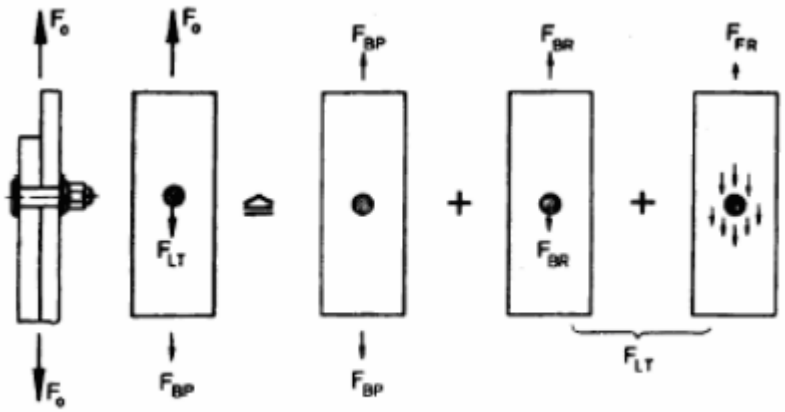

Figure 12 - Acting forces on a double plate riveted joint. Source: Xavier, 2006.

According to Sedlacek and Müller, 2005, the existent residual stress around the drill spots on the plates highly influences the load transfer. It is a consequence of three factors:

- Squeeze force applied;
- Eventual deformity that can occur during the attachment process;
- Secondary moment due to the joint eccentricity and the rivet flexibility.

Studies done by Rijck and Fawaz, 2004, about the load transfer along the rivets rows, considering the neutral line equations below, and applying inner moments, showed a great method to compare real tests with theory. It is important to remember that the neutral line is found at the centroid of the shape of isotropic homogeneous beam, also for a homogeneous doubly symmetric section, it is located at half of the beam.

$$\bar{y} = \frac{A_1\overline{y_1} + A_2\overline{y_2} + \cdots + A_n\overline{y_n}}{A_1 + A_2 + \cdots + A_n} \tag{2.1}$$

$$\bar{x} = \frac{A_1\overline{x_1} + A_2\overline{x_2} + \cdots + A_n\overline{x_n}}{A_1 + A_2 + \cdots + A_n} \tag{2.2}$$

In Equation 2.1 the component $\bar{y}$ represents the distance on the vertical axis from the absolute zero until the centroid of the beam. This way, it is a sum of the centroid distance of each part that forms the beam, multiplied by its area, divided by the sum of all areas.

Similarly, Equation 2.2 brings the $\bar{x}$ component, which is the distance from the absolute zero horizontal axis to the centroid of the beam.

Rijck and Fawaz, 2004, used finite elements models and destructive tests on hybrid joints of aluminum and thread-metal composite. These tests focused on obtaining the relation between the headset diameter and the squeeze force for different types of rivets. It is important to notice, at this point, that the mathematical model developed by Swift, 1971 – that correlates a spring and a beam formula –, determinates the inertia of the beam element as a good alternative for the representation of the rivets.

2.1.3 Fatigue fracture process

According to Tec Eurolab, 2018, the fatigue fracture process is divided into three stages, including fatigue fracture initiation, propagation, and final rupture. They happen under repeated

or fluctuating stresses having a maximum value less than the tensile strength. Moreover, according to Yucan, 2015, fatigue life usually consists of the initiation life and the propagation life of a fatigue crack.

The first stage, fatigue initiation, is the phase in which the cumulative damage, characterized by the accumulation of microchanges over a large number of load applications, happens. In this phase, the irreversible changes in the material are caused by repetitive shear stresses. The second stage, or fatigue propagation, then starts and is described as the stage in which the microcrack changes direction and grows perpendicular to the tensile stress. It continues, gradually reducing the cross-sectional area of the part, eventually weakening it. Finally, the last stage, or final rupture, starts. It is characterized by the complete fracture that can occur with only one more load application. It represents the last load applied to break the part (Tec Eurolab, 2018).

The fatigue damage often occurs in a stress concentration position, such as the specimen surface or defect, or a hole. The maximum compressive residual stress occurs at the hole edge near the middle plane, whereas the smallest compressive residual stress occurs at the entrance face. Results suggest that all specimens with a hole broke at the plane of the smallest cross section, according to Figure 13.

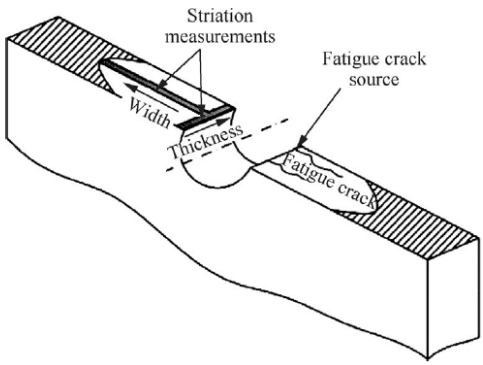

Figure 13 - Fractography analysis of a metal fatigue specimen Source: Yucan, 2015.

The crack propagation life is longer than the crack initiation life. In order to increase the fatigue life effectively, crack propagation time needs to be extended as long as possible using anti-fatigue manufacture approaches. It is suggested that the size of the crack propagation area increases with the increasing of the expansion degree. In addition, the residual stress may be explained using a fatigue crack closure model in which compressive residual stress reduces the effective stress intensity factor, consequently reducing the crack growth rate (Yucan, 2015).

The effective stress intensity factor, K_{eff}, is equal to the residual stress intensity factor, K_{res}, plus the stress intensity factor caused by the external applied load, K_{app}. In order to estimate the residual stress intensity factor along the crack plane, the closure-based method and the weight function technique are used, in which the effective stress intensity factor is a solution to the problem of crack propagation, being a relation between fatigue life and residual stress field. This is helpful for the study of fatigue life which is strengthened by the cold expansion technology (Yucan, 2015).

Two different approaches can be taken to analyze the fatigue life of structures. The first one is based on the S-N approach, which deals with the Miner damage accumulation rule, and the second one is based on fracture mechanics (Huang, 2012). The Miner's Rule is a simple cumulative damage model that states the following Equation:

$$\sum_{i=1}^{k} \frac{n_i}{N_i} = C \tag{2.3}$$

Where n_i is the number of cycles accumulated at stress, S_i, N_i is the average number of cycles to failure at the i^{th} stress, and C is the fraction of life consumed by exposure to the cycles at the different stress levels. Then, commonly when C is equal to one, failure occurs.

2.1.4 Stress forces and fatigue life

2.1.4.1 Stress forces acting on joints

According to Xavier, 2006, joints are the greater spot of stress, commonly the responsible for structural element failure. Under efforts that cause eccentricity – in this case, tension forces that can misalign the plates –, a secondary moment appears, originating offsets out of the middle plane of the joint.

Schijve, 1972, analyzed this moment effects and verified that, in addition to the residual stresses – developed during the insertion of the fastener inside the hole due to the interference in the hole, also the friction between the joined plates –, it causes non-linear displacements and plastic deformation in the plates and fasteners. These effects can interfere in the joint behavior and the load transfer by the fasteners.

Tate and Rosenfeld, 1946, developed studies to determine the forces acting on the rows of fasteners. They used different configurations on top joints and found out that the outside rows of fasteners absorb more loading than the inner rows during the elastic regime, for the

same thickness plates and symmetrical joints. It can be seen in Figure 14, where the splice plate used has the highest load carried by the end fasteners.

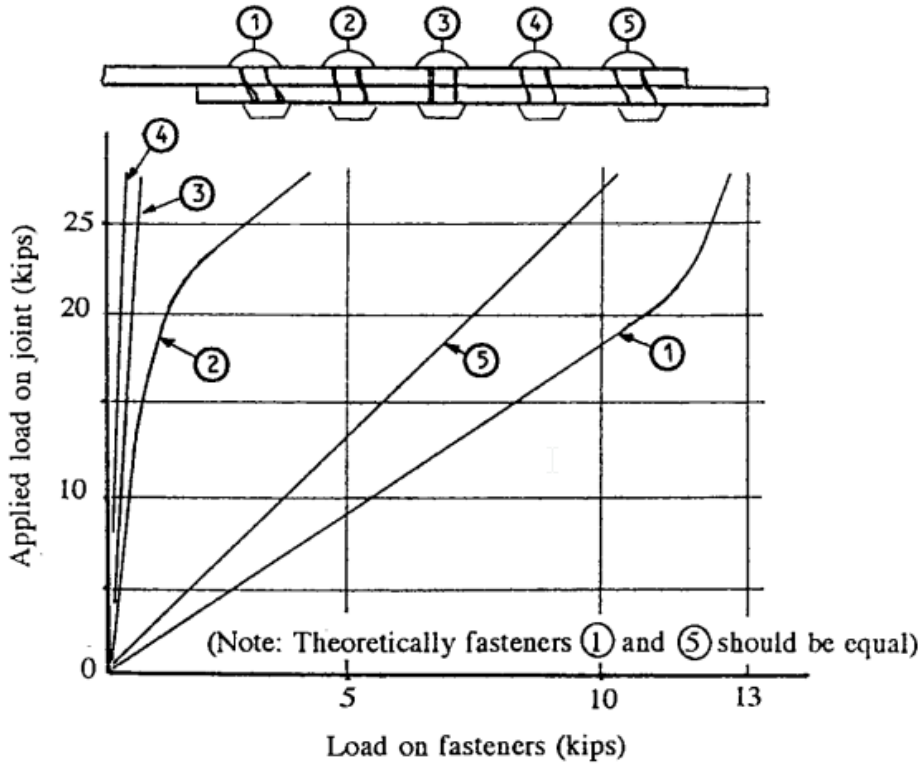

Figure 14 - Test Results for Fastener Load Distribution on a Lap Joint. Source: Niu, 1999.

In order to minimize the variation observed, result of splice eccentricities, fastener hole imperfections, and fastener preload, every fastener installation should be tightly controlled per a specification on the engineering drawing. Moreover, the finite element model, FEM, is the most accurate analysis to obtain the best fastener load (Niu, 1999). A sample of structural finite element modeling for a lap joint of four fasteners is given by Figure 15.

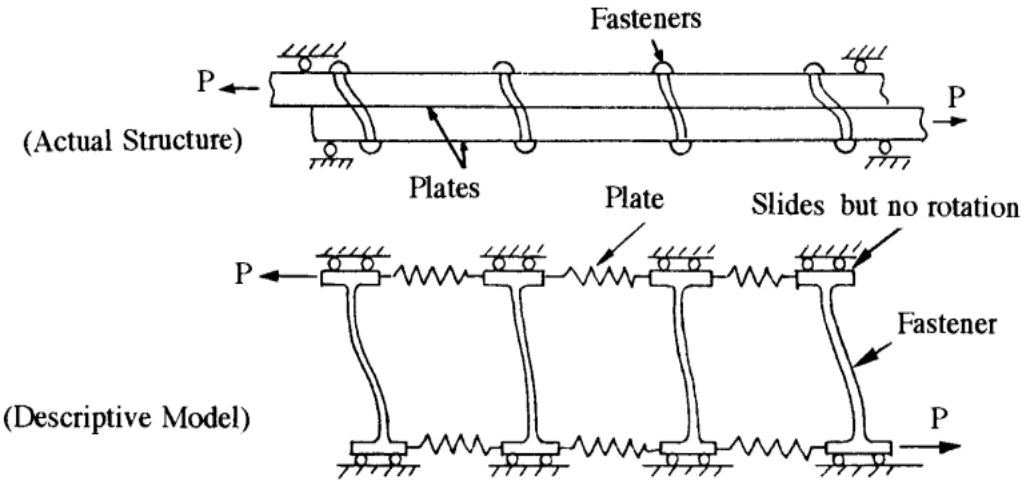

Figure 15 - Four fastener lap joint. Source: Niu, 1999.

Looking forward to the loads distribution through the fasteners on symmetrical top joints, Tate and Rosenfeld, 1946, confirmed that there is an unequal distribution along them. It happened on plates double attached with two or three bolts, during and after the elastic zone. Moreover, it was shown that the load distribution achieved an equality level only nearby to the joint failure.

Tate and Rosenfeld, 1946, assumed that the relation between stress and deformation was constant, while the stress had a uniform distribution along the transversal sections. Besides, the friction was considered negligible and the bolt adjustment neither caused damage to the plates, nor residual stresses, like inferred for the drilling process of the plates. Finally, the relation between fastener displacement and load applied was considered linear in the elastic zone.

According to Huth, 1985, there is no important variation in the flexibility of thick plates when you compare static and cycle loads.

2.1.4.2 Fatigue analysis

Rijck and Fawaz, 2002, concluded that the electronic microscope is the best tool for analysis and reconstruction of the major portion of the crack due to fatigue. However, this method takes more time to be executed. Moreover, they verified that the mesh shape varies along with the fatigue-life and it depends on the stress intensity factor, *K*.

This factor has originally been developed in the context of fracture mechanics, and describes the stress level around the singularity, being possibly superimposed by the crack-parallel non-singular T-stress – the constant stress acting parallel to the crack line direction –. Besides, the local three-dimensional stress singularity at a definite point of the crack or slit front

can generally be described by superimposition of three two-dimensional stress singularities corresponding to three independent loading or opening modes of crack tip: transverse tensile loading (mode I), in-plane shear loading (mode II), and out-of-plane shear loading (mode III). (Radaj & Vormwald, 2013). For the specific case of the present work, action was taken in order to guarantee only the tensile loading (mode I) happening on the joint.

The three tensile loading modes produce the asymptotic stress distribution around the crack tip as written in the equation below:

$$\sigma_{ij} = \frac{1}{\sqrt{2\pi r}}[K_I f_{I,ij}(\theta) + K_{II} f_{II,ij}(\theta) + K_{III} f_{III,kz}(\theta)] \tag{2.4}$$

Where "i, j" are equivalent to "x, y", or "r, θ", and "k" is equal to "r, θ". The mode-related K_I, K_{II},K_{III}depend on the magnitude of the load, the crack length and further geometrical parameters of the considered configuration. The mode-related angle-dependent functions $f_{I,ij}$, $f_{II,ij}$, and $f_{III,iz}$ describe the angular distribution of the stresses at the crack tip. (Radaj & Vormwald, 2013). These stresses are given in Figure 16 in polar coordinates.

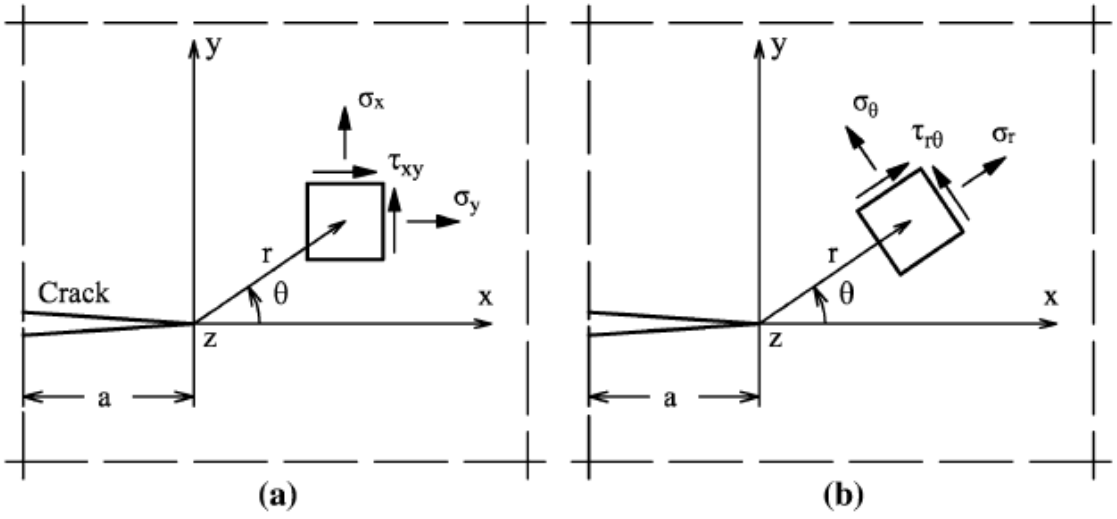

Figure 16 - Cartesian (a) and polar (b) coordinate systems with correspondingly defined stresses at the crack tip. Source: Lazzarin and Tovo, 1998.

Moreover, the mode of interest for the present study, the tensile loading, can be given by polar coordinates, described by the equations below:

$$\begin{pmatrix} \sigma_r \\ \sigma_\theta \\ \tau_{r\theta} \end{pmatrix} = \frac{K_I}{4\sqrt{2\pi r}} \begin{pmatrix} 5\cos\left(\frac{\theta}{2}\right) - \cos(\frac{3\theta}{2}) \\ 3\cos\left(\frac{\theta}{2}\right) + \cos(\frac{3\theta}{2}) \\ \sin\left(\frac{\theta}{2}\right) + \sin(\frac{3\theta}{2}) \end{pmatrix} \tag{2.5}$$

$$\sigma_z = 0 \ (plane\ stress) \tag{2.6}$$

$$\sigma_z = \nu(\sigma_r + \sigma_\theta) = \frac{2\nu K_I}{\sqrt{2\pi r}} \cos\left(\frac{\theta}{2}\right) (plane\ strain) \tag{2.7}$$

In Equation 2.6 "ν" is the Poisson Coefficient, which represents the ratio between the transversal and longitudinal strains, result of the change in length of the elementary form. It is important to notice that, for high values of *K*, the cracked surface is very irregular. This fact turns the crack marks detection hard, while for low values of *K*, the discrimination between crack marks and other kinds of striation on the cracked surface is the problem. It happens due to the similar value they have for ΔK_f, the variation in the effective stress intensity factor for cycling load, fatigue notch factor. (Rijck and Fawaz, 2002).

Moreover, according to Niu, 1999, it is feasible to estimate the joint fatigue life, based on the severity factor, SF, which is the local peak stress caused by load transfer and bypass load, as shown in Figure 17. This procedure, used to determine the fatigue life of the component, is described afterwards.

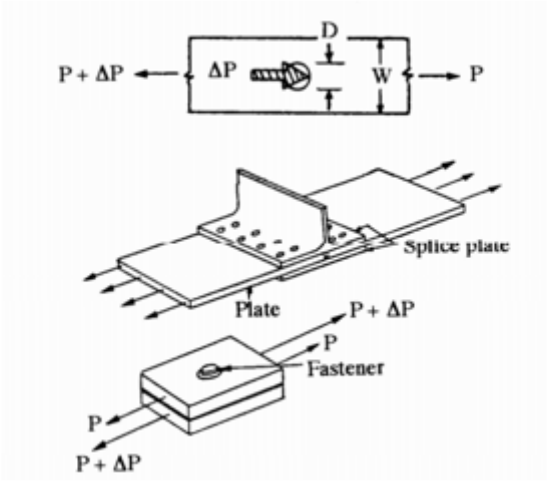

(a) Loads in a Fastener

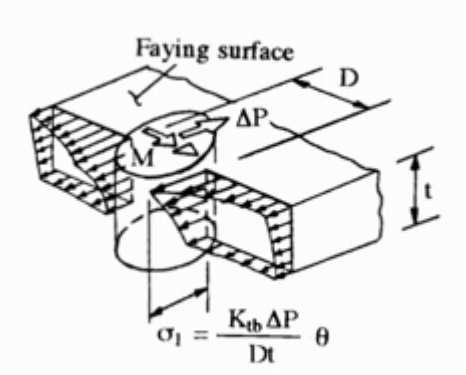

(b) Local Stress caused by Load Transfer, ΔP

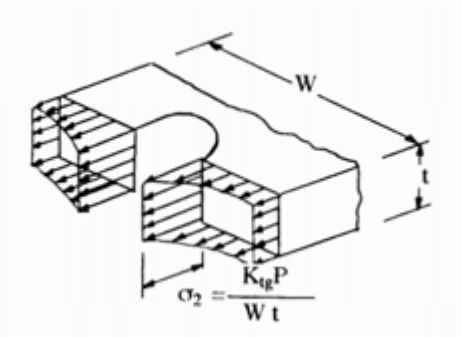

(c) Local Stress caused by Bypass Load, P

Figure 17 - Stresses at a Loaded Fastener Hole. Source: Niu, 1999.

To continue the fatigue analysis through the proposed model, the severity factor is given by the Equations:

$$SF = \left(\frac{\alpha\beta}{\sigma}\right)[\sigma_1 + \sigma_2] \tag{2.8}$$

$$SF = \left(\frac{\alpha\beta}{\sigma}\right)[(\frac{K_{th}\Delta P}{Dt})\theta + (\frac{K_{tg}P}{Wt})] \tag{2.9}$$

Where, α is the fastener hole condition factor – 1.0 for standard drilled hole and 0.7 or 0.8 to cold worked hole –, β is the hole filling factor – 1.0 for an open hole and 0.75 to bolts and rivets –, σ is the reference stress in the structure, σ_1 is the local stress caused by load transfer, σ_2 is the local stress caused by bypass load, P is the bypass load, ΔP is the load transfer through the fastener, D is the fastener diameter, t is the splice plate thickness, W is the width

of the plate, K_{th} is the bearing stress concentration factor, θ is the bearing distribution factor, and finally, K_{tg} is the stress concentration factor.

Those bearing stress concentration factor, bearing distribution factor, and stress concentration factor should be find through the correlative curves, similar to the ones shown in Figures 18, 19, and 20.

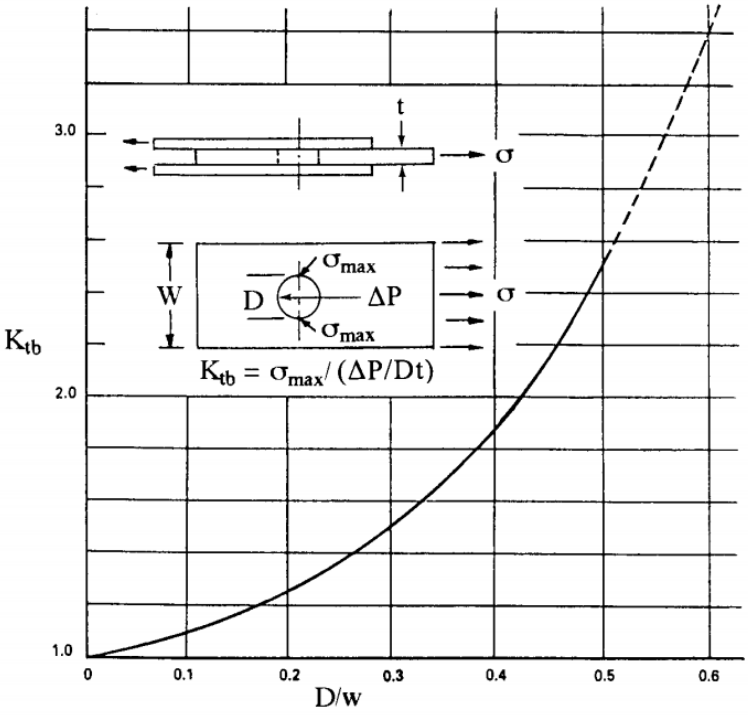

Figure 18 - Bearing stress concentration factor. Source: Niu, 1999.

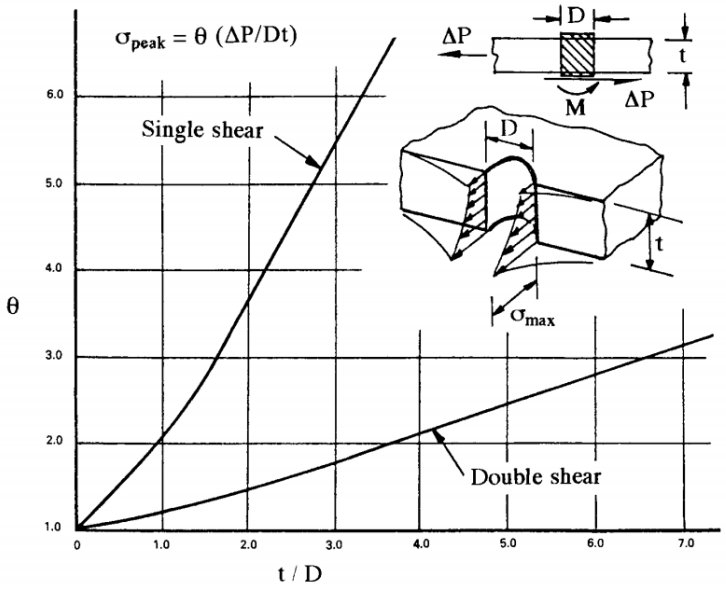

Figure 19 - Bearing distribution factor. Source: Niu, 1999.

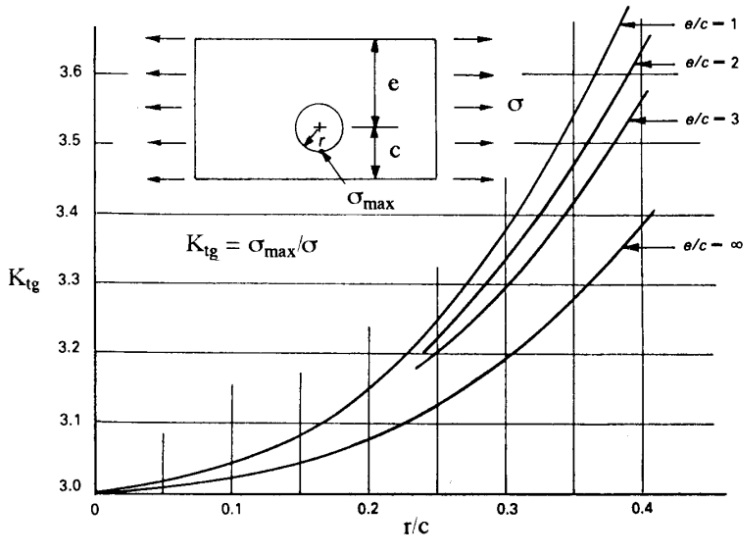

Figure 20 - Stress concentration factor. Source: Niu, 1999.

Once those parameters are found, it is necessary to get the fatigue quality index, *K*, also available on a comparative curve, given by the sample Figure 21.

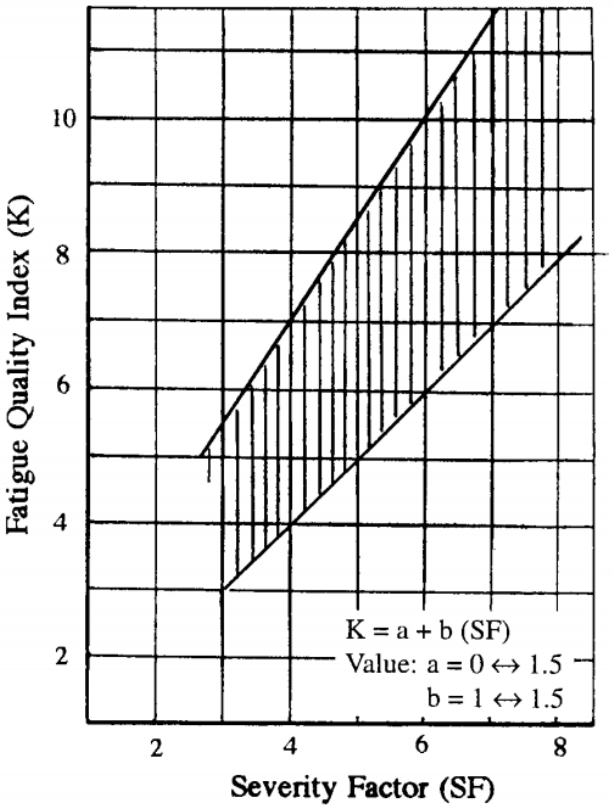

Figure 21 - Discrepancy factor given by the Severity Factor vs. Fatigue Quality Index (K). Source: Niu, 1999.

Finally, it is necessary to select the appropriate S-N curve – which is given through the method described in section 2.1.3 –, to use in calculating joint fatigue, knowing the theoretical stress concentration factor value, K_t, that is equivalent to the maximum stress over the nominal stress. Figure 22 shows the relation between these parameters.

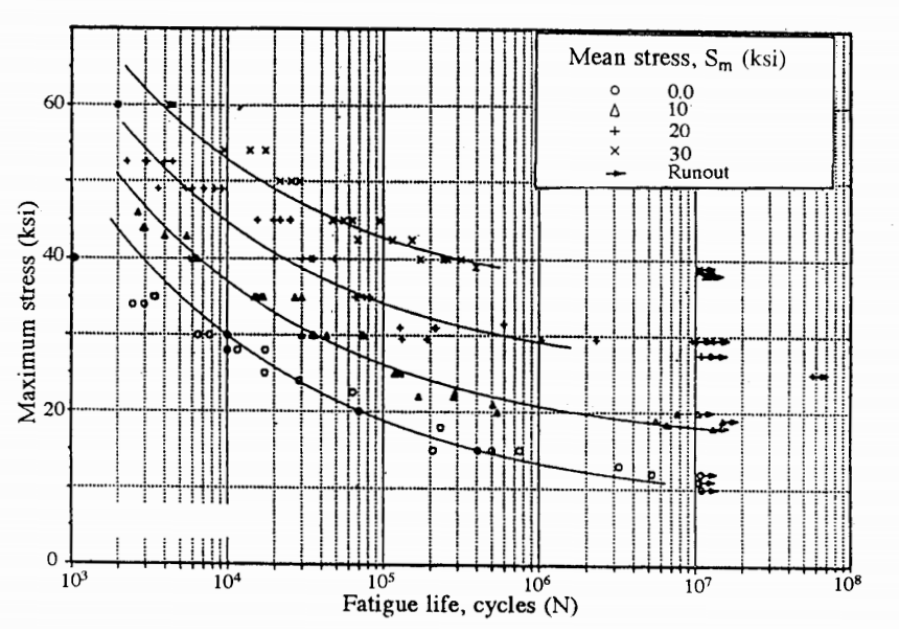

Figure 22 – S-N curve for a notched, K_t=2. Source: Niu, 1999.

2.1.4.3 Types of fatigue damages

The damage caused by generalized fatigue or Widespread Fatigue Damage, WFD, is a consequence of multiple-site damage, MSD, and multiple-element damage, MED. FAA with along manufacturers and operators identified WFD-susceptible structure, as shown in Table 1. This list does not exclude any particular structure that may suffer with WFD.

Table 1 – WFD-susceptible structure (Adapted from Hoggard, 2012).

Structure	Damage type
Fuselage frames; String to Frame Attachments; Over-Wing Fuselage Attachments	MED
Lap Joints with Milled, Chem-milled, or Bonded Radius; Skin Splice at Aft Pressure Bulkhead	MSD
Longitudinal Skin Joints, Frames, and Tear Straps; Circumferential Joints and Stringers; Shear Clip End Fasteners on Shear Tied Fuselage Frames; Aft Pressure Dome Outer Ring and Dome Web Splices; Abrupt Changes in Web or Skin Thickness – Pressurized or Unpressurized Structure; Window Surround Structure; Latches and Hinges of Non-plug Doors; Wing or Empennage Chordwise Splices; Rib-to-Skin Attachments; Typical Wing and Empennage Construction	MED/MSD

An example of a structure susceptible to WFD damage determined by FAA is shown in Figure 23, in which the process occurs through MSD.

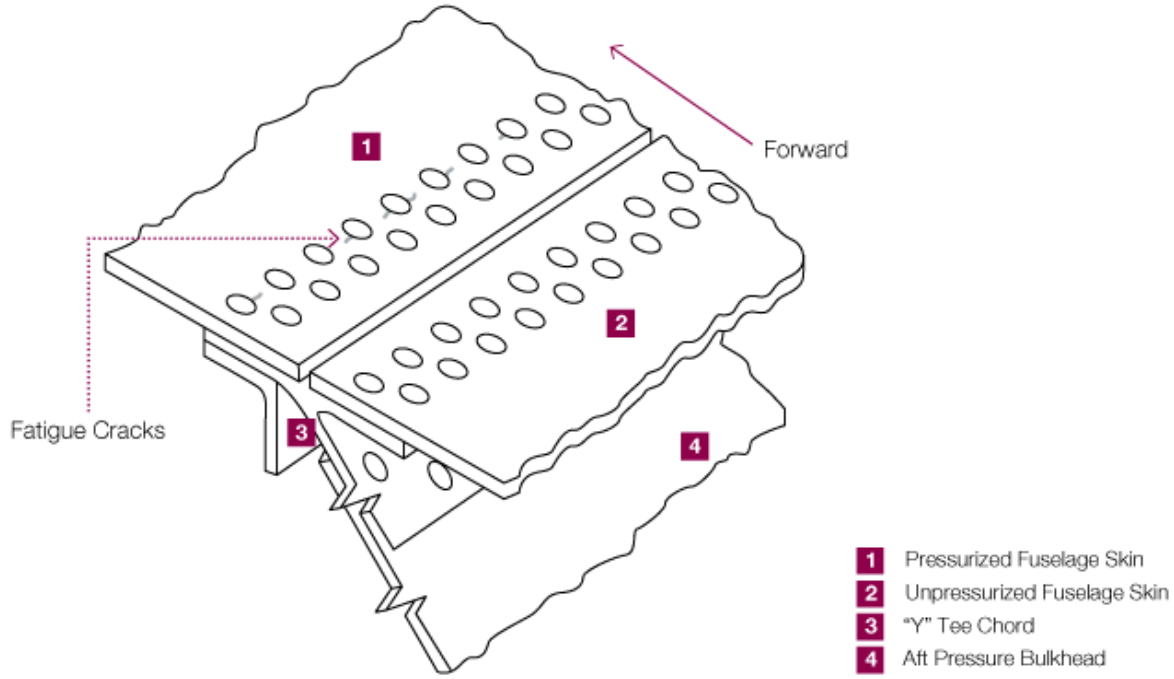

Figure 23 - Skin Splice at Aft Pressure Bulkhead susceptible to WFD damage. Source: Hoggard and Johnson, 2012.

WFD in a structure of an airplane is defined as the simultaneous presence of cracks at multiple locations that are of enough size and density that the structure will no longer meet

required damage tolerance and will not maintain required residual strength after partial structural failure (Hoggard and Johnson, 2012). An example of WFD is shown in Figure 24.

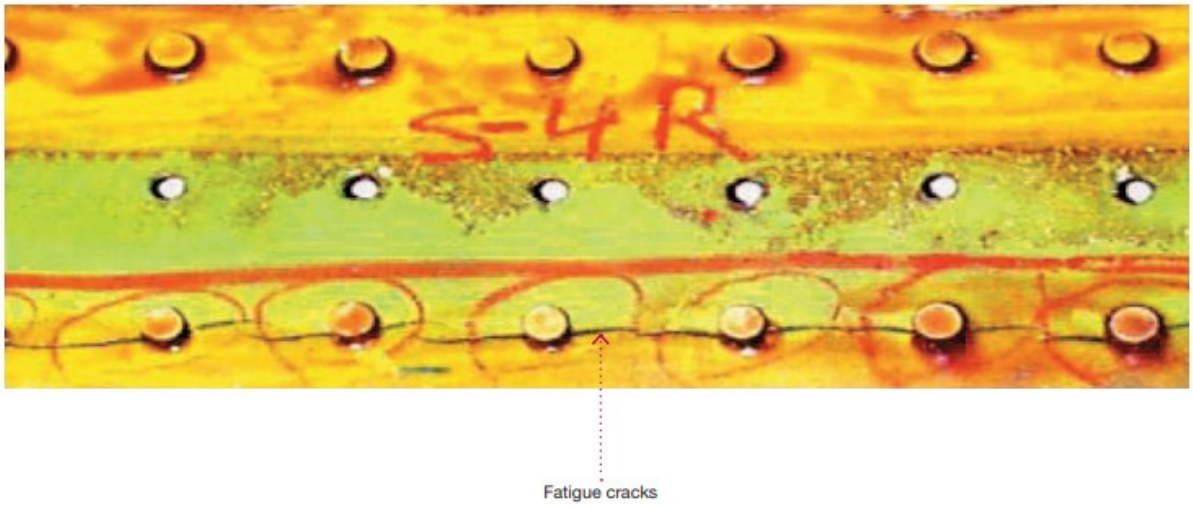

Figure 24 - Cracks on a lap splice characterizing a WFD example. Source: Hoggard and Johnson, 2012.

For riveted aeronautical structures, the WFD happens because of the stress slopes generated due to the contact between rivets and holes. For the specific case of overlapping joints, the load transfer suffers influence of the displacement limitation outside the joint plan due to the presence of the rivets. Therefore, the residual stress field influences the cracks propagation caused by fatigue in the drilling spot, due to the rivets insertion process.

Finally, Szolwinski and Farris, 1994, studied the riveting process and its residual stress field creation. It was concluded that the circumferential stress distribution along with high squeeze force values creates a compressive residual stress zone, prevalent nearby the holes outskirts. At the same time, a tension residual stress zone, created along the hole, causes deep impact in the nucleated cracks propagation on the rivet-hole interface and the plates contact surface.

2.1.5 Strength of riveted joints and failure modes

The strength of a riveted joint is evaluated through the analysis of all possible failure paths in the joint, considering one pitch length of the plate. This way, there are four possible ways a single riveted joint may fail: tearing of the plate, shearing of the rivet, crushing of rivet, and tearing of the plate at edge (NPTEL, 2018).

The first, tearing of the plate, happens when the force is too large that causes the plate to fail in tension along with the row, as shown in Figure 25. For this specific case, the maximum force allowed is described by equation below.

$$P_1 = s_t(\mathrm{p} - \mathrm{d})\mathrm{t} \tag{2.10}$$

Where s_t is the allowable tensile stress of the plate material, p is the pitch, d is the diameter of the rivet hole, and t is the thickness of the plate.

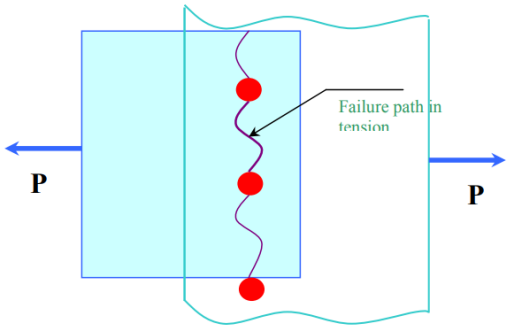

Figure 25 - Failure of a plate in tension (tearing). Source: NPTEL, 2018.

Moreover, a failure caused by the rivet by shearing occur when the shear stress is elevated that the rivet is no capable of absorbing that. It is illustrated in Figure 26. Also, the maximum force withstood by the joint to prevent this failure is described by equation:

$$P_2 = s_s(\frac{\pi d^2}{4}) \tag{2.11}$$

Where s_s is the allowable shear stress of the rivet material, and d is the hole diameter. For a single lap strap butt joint, the equation used is the 2.11, but for a double one, it should be multiplied by two.

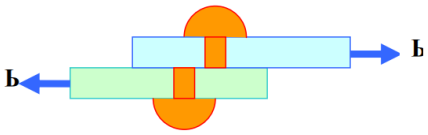

Figure 26 - Failure of a rivet by shearing. Source: NPTEL, 2018.

Besides, there is still the failure caused by the crushing of the rivet, when the bearing stress on the rivet is too large that the contact surface between the rivet and the plate gets damaged, as shown in Figure 27. To avoid this problem, it is necessary to assume that the contact stress is uniform, resulting in a maximum allowed force described by equation:

$$P_3 = s_c dt \tag{2.12}$$

Where s_c is the allowable bearing stress between the rivet and the plate material, d is the hole diameter, and t is the plate thickness.

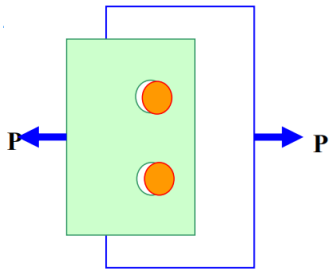

Figure 27 - Failure of a rivet by crushing. Source: NPTEL, 2018.

Finally, there is the joint failure due to the tearing of the plate edge, when its margin is too small, that the plate fails as demonstrated in Figure 28. To avoid this problem to happen, it is required a minimum margin described by equation:

$$m = 1.5d \tag{2.13}$$

Where m is the allowable minimum margin between the rivet and the plate material border, and d is the hole diameter.

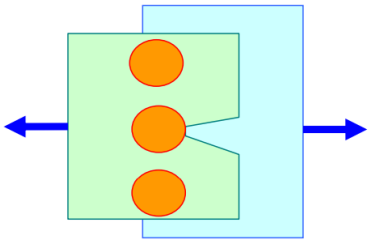

Figure 28 - Failure by tearing of the plate at the edge. Source: NPTEL, 2018.

Considering these failure modes, it is possible to define the maximum force that can be applied to the joint and its design constrains. The equation below defines the efficiency of a single riveted joint, as a ratio between the maximum of the critical loads that the joint can resist, and the load carried by a solid plate.

$$efficiency\ (\eta) = \frac{\min\{P_1, P_2, P_3\}}{s_t pt} \tag{2.14}$$

Where $s_t pt$ represents the load carried by a solid plate, when s_t is the allowable tensile stress of the plate material, p is the pitch, and t is the thickness of the plate.

Then, it is possible to define the mainly parameters for the joint based on plate thickness, resulting on the holes diameter, pitch and margin. Considering a thickness of the plate greater than 8mm, the diameter is obtained according to equation:

$$d = 6\sqrt{\mathrm{t}} \tag{2.15}$$

For a thickness of the plate smaller than 8mm, the diameter is obtained according to equation:

$$s_c t = \frac{\pi}{4} d s_s \tag{2.16}$$

In the second case, the diameter is provided by equating crushing strength to the shear strength, once the thickness is low. However, it is important to notice that the diameter should not be less than thickness, in any case.

Finally, in order to define the pitch, it is necessary to equate the tearing strength of the plate to the shear strength of the rivets. However, the pitch should be assumed as at least to two times the diameter value. Also, the margin is assumed as 1.5 times the diameter size.

2.2 Limits of Validity

Limits of validity or LOV, are the operational limits established through services actions necessary to preclude the onset of WFD. This way, the limits are based on fatigue test evidence, which supports the maintenance program of an aircraft. According to FAA, LOV is "the period of time – in flight cycles, flight hours, or both – up to which it has been demonstrated by test evidence, analysis and, if available, service experience and teardown inspections, that widespread fatigue damage will not occur in the airplane structure." It is further defined as the point in the structural life of an airplane at which there is significantly increased risk of uncertainties in structural performance and probable development of WFD. (Hoggard and Johnson, 2012).

FAA determines through AC 25.571-1D that the applicant must establish inspections and maintenance actions as necessary to avoid catastrophic failure during the operational life of the airplanes. It is based on the results of the evaluations required on all structure that can contribute to catastrophic failure with respect to the susceptibility to fatigue, corrosion, and accidental damage. Then, the LOV is required as the definition of the operational life of the airplane, being identified in the structural-maintenance program.

The fatigue-life prediction of an airplane defines directly the LOV, and all the modifications and requests from aeronautical authorities directly affects the manufacturers and operators of aircrafts, which need to comply with those requirements. This way, the main sources of fatigue test evidence held by the manufacturer include full-scale fatigue test, full-scale component tests, teardown and refurbishment of a high-time airplane, statistical fleet-proven life techniques, evaluation of in-service problems/test data experienced by this model

or other airplanes with similar design concepts, and analysis methods that have been parametrically developed to reflect fatigue test and service experience.

2.3 Cold work

"Coldworking", cold work or cold expansion is a studied alternative to countervail the fatigue life problem in notched components. These joints have high stress concentration under exposure to loadings that generate fatigue, which can cause crack initiation and propagation on the riveted component structure. It happens due to the load cycling that the airplane is subjected to. For the specific cases of wing-to-wing joint, the wings bend up and down several thousand times a year during take-off and landing, also during the flight maneuvers themselves. The weakest part of the component, where the fatigue cracks can initiate, are the holes, originated from the drilling process to join parts.

In order to improve the fatigue life of aircraft structures, extensive research has been carried out in two areas: advanced materials and manufacturing processes, by scholars and aviation manufacturing enterprises. On one hand, novel titanium alloys and composites as representatives of advanced materials are widely used in modern aircraft structures, reducing the overall weights of aircraft structures and improving the fatigue resistance performances of structures during service periods. On the other hand, using structure optimization and different anti-fatigue manufacturing process methods, the fatigue life of aircraft is improved and the service time is prolonged effectively (YUCAN, 2015).

Implementing riveted or bolted joints needs the components to be drilled to create fastener holes, which causes geometrical discontinuities and entail local stress (or strain) concentration during loading. Investigations showed that there were a number of accidents caused by fatigue failures initiating from fastened joints (YUCAN, 2015).

This way, techniques such as laser shock, shot peening, interference fitting, and cold expansion are being studied, as a contravention to the hole drilling effects to the fatigue-life of the structural component.

Laser shock is a compressive residual stress reduction technique to improve the fatigue and corrosion properties. However, there is a high cost of laser and operation, and a difficulty of application in the productive process, due to its lack of stability.

Shot peening modifies the surface and the characterizing parameters near to the surface substrate. It includes mainly the elastic residual stress distribution, increased surface hardness, higher near-surface dislocation density, and alternated surface topography. Over high surface

roughness caused by the process, a residual stress is generated, contributing to prolong the fatigue life. In addition, there is a reduction in the assembly stiffness of an aircraft structure.

Interference fitting is a method that implies in a high interference level, but difficult to control due to its instability. Moreover, the high interference level can easily damage the hole surface, and the protuberance generated in installation can be harmful to the strength of joints. It can also cause reduced strength on the connection and affect the structure regular assembly.

Cold expansion is a technique that applies an oversize tapered mandrel through the hole. During this process, there is an elastic-plastic deformation that creates a compressive residual stress zone along the hole area, as shown in Figure 29. The residual stress can reduce the concentration stress and delay the initiation and propagation of fatigue cracks. This alternative is considered highly effective in preventing premature fatigue failure undergoing cycling loading (PAPANIKOS, 1998).

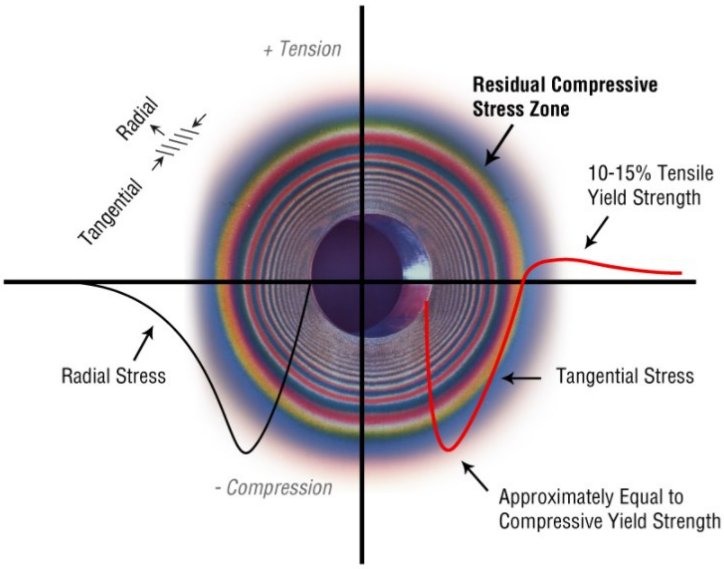

Figure 29 - Forces acting around a drilled hole. Source: Fatigue Technology, 2018.

2.3.1 Cold expansion process

The cold expansion process is not related to the temperature used during the process, since it is performed at normal room temperature. Thus, it is called cold expansion because there is no need of high temperatures to cause modifications on the material properties.

Khodabakhshi, 2016, analyzed the effects of cold work process between aging and solution heat treatment on the microstructure of a copper-beryllium alloy C17200 focusing on

its wear behavior. It was concluded that the formation of fine-grained structure and γ phase particles enhances the mechanical properties of the alloy without reducing the wear rate.

Many cold expansion approaches have been developed and investigated according to the diverse expansion tools. The most widely used methods in practice are four cold expansion techniques: hole edge expansion, direct mandrel expansion (without sleeve), ball expansion, and split sleeve expansion processes (Yucan, 2015).

The hole edge expansion uses a high-hardness tapered indenter or a rigid ball to extrude or hammer the hole edge through an axial force *F*, shown in Figure 30.

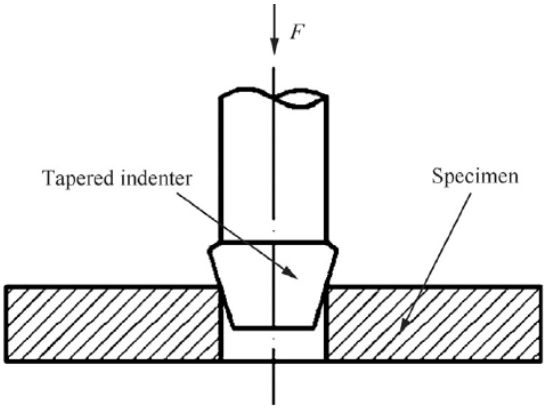

Figure 30 – Hole edge expansion process. Source: YUCAN, 2015.

During the process, there is a plastic deformation in the material near the edge of the hole, generating a compressive residual stress zone in the same area. However, this approach is limited by the center of the hole that is not directly strengthened. Thus, the process is not suitable for thick-plate and needs to carry out multiple expansions for holes in order to enhance the component fatigue life.

Furthermore, the direct mandrel expansion process consists of pushing a pre-lubricated tapered mandrel through the hole from the entrance side of the specimen and removing it from the other side, as shown in Figure 31.

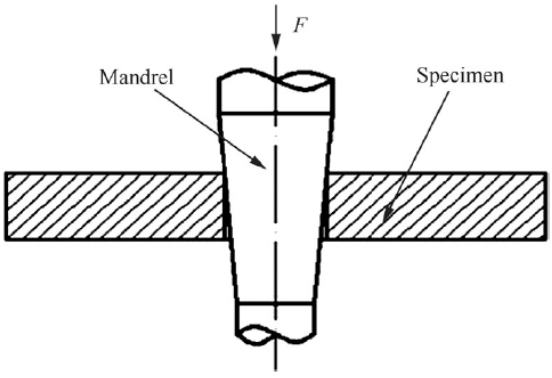

Figure 31 – Direct mandrel expansion process. Source: Yucan, 2015.

In this case, the hole suffers permanent plastic deformation and there is a proper distribution of compressive residual stresses around the fastener hole. This effect is generated during the mandrel removal, because of the material surrounding elastic material attempt to return to its non-deformed state. Moreover, this method has advantages of burnishing and smoothing the hole surface, due to the direct contact between the mandrel and the hole surface.

Besides, the ball expansion is another alternative to the mandrel expansion process, by inserting an oversized hard steel ball in the hole, instead of the mandrel, and removing it from the other side, as demonstrated in Figure 32. Withal, this method produces a localized interference ring between the steel ball and the hole surface, causing less friction than in the mandrel expansion process. Therefore, its benefits are smaller than in the other expansion methods.

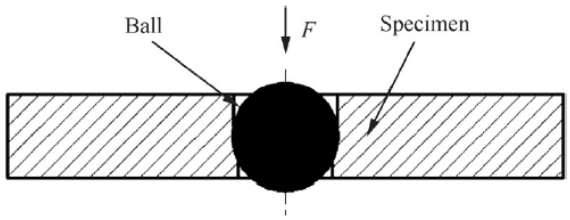

Figure 32 – Ball expansion process. Source: Yucan, 2015.

Finally, the split sleeve expansion represents an alternative to solve the problem with the mandrel or ball problem caused during its introduction, which is the surface damage at the interface. A scheme of this process is shown in Figure 33.

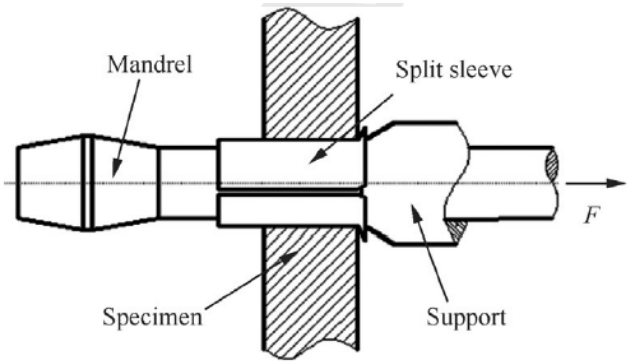

Figure 33 – Split sleeve expansion process. Source: Yucan, 2015.

This process works using a solid tapered mandrel and an internally lubricated stainless-steel split sleeve. The split sleeve is placed over the mandrel, and the mandrel/sleeve assembly is inserted into the hole. When the larger diameter part of the mandrel moves through the sleeve, it generates plastic deformation of the material. In addition, when the mandrel is withdrawn

from the sleeve, some elastic recovery can take place. Besides, a permanent enlargement of the hole with along a desired compressive residual stress is left when the split sleeve is removed from the hole.

Due to the split in the sleeve, there is a formation of a pip on the bore of the surface of the hole that needs to be removed in order to avoid the occurrence of cracks near to it. A reaming operation does this function, sizing the hole accurately after cold work.

Finally, this method presents great advantages, being good for adaptability and production efficiency, but also causes small damage around the hole surface after expansion.

2.3.2 Residual stress

Residual stress is produced when a metal or other material is plastically deformed under an applied tensile or compressive stress. When plastic deformation occurs, not all of the metal undergoing that stress has been deformed in the same manner or to the same extent. These differences may be due to the distribution of the applied stress. As is the case in bending, where one side of the object will have been deformed in tension and the other in compression, or they may be due to the fact that the yield stress of an individual grain in a metal sample depends in part on its crystallographic orientation and that therefore different grains in a sample are likely to undergo different amounts of yield for a given macroscopic stress. When the applied stress is removed, the macroscopic stress on the sample will return to zero. However, significant internal compressive and tensile residual stresses may remain within the sample provided that the sum of the internal forces is zero (Makar, 2000).

The Stress-Strain Curve is a visible way of noticing the response of the body-proof to the tensile test when one end is clamped in a loading frame and the other is subjected to a controlled displacement, δ, as shown in Figure 34. The load, $P(\delta)$, is obtained through electronic reading, in this case.

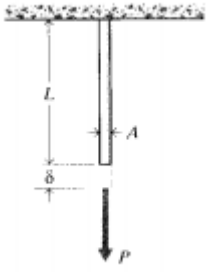

Figure 34 – Tension test according to controlled displacement. Source: Roylance, 2001.

For the Stress-Strain Curve, it is necessary to notice that the parameters of stress, σ_e, and strain, ϵ_e, are defined by measuring the load and deflection of the original specimen cross-sectional area, A_0, and length, L_0, as shown in equations below.

$$\sigma_e = \frac{P}{A_0} \tag{2.17}$$

$$\epsilon_e = \frac{\delta}{L_0} \tag{2.18}$$

Plotting ϵ_e against σ_e results in a curve similar to the one shown in Figure 35.

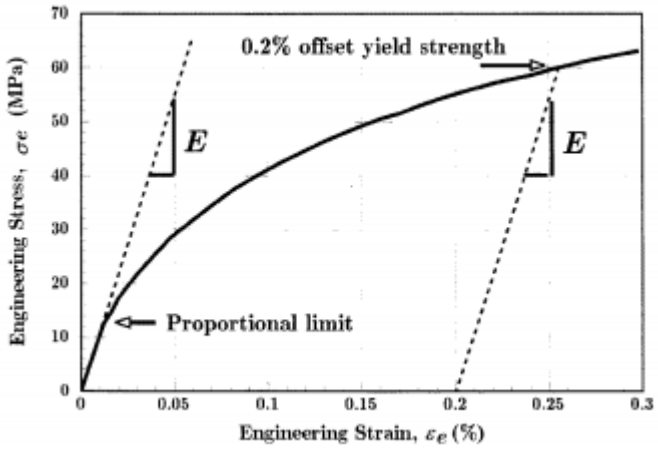

Figure 35 – Low-strain region of the engineering stress-strain curve for annealed polycrystalline cooper, typical of many ductile metals. Source: Roylance, 2001.

Roylance, 2001, states that in the early (low strain) portion of the curve, many materials obey Hooke's law to a reasonable approximation, so that stress is proportional to strain with the constant of proportionality being the modulus of elasticity or Young's modulus, E, as shown in equation below.

$$\sigma_e = E\epsilon_e \tag{2.19}$$

As strain is increased, many materials eventually deviate from this linear proportionality, the point of departure being termed the proportional limit. This nonlinearity is usually associated with stress-induced "plastic" flow in the specimen. Here the material is undergoing a rearrangement of its internal molecular or microscopic structure, in which atoms are being moved to new equilibrium positions. This plasticity requires a mechanism for molecular mobility, which in crystalline materials can arise from dislocation motion (discussed further in a later module). Materials lacking this mobility, for instance by having internal microstructures that block dislocation motion, are usually brittle rather than ductile. The stress-

strain curve for brittle materials are typically linear over their full range of strain, eventually terminating in fracture without appreciable plastic flow (Roylance, 2001).

The cold expansion technology utilizes the residual stresses caused by local plastic deformation strengthening process, to achieve anti-fatigue manufacture. It is important to notice that the strengthening effect depends on the size and distribution of the residual stress.

In order to measure this residual stress, different methods have been used, being classified as point measurement type – when the residual stress field is fitted with some point stress by repeated measurement –, or face measurement type – in which the problem with the accuracy is solved because the experimental measurements are averaged over a 1 mm x 1 mm area. Strain gage method, hole-drilling method, X-ray diffraction method, and single beam laser speckle interferometry are the most common point measurement methods used. Furthermore, moiré interferometry and photo elastic coating method are widely used face measurement methods.

Although, it is difficult to measure with accuracy this distribution, using finite element simulation through designs of meshes and material properties is a great way to obtain the desired measurement. The typical distribution of tangential residual stresses, σ_θ, around a cold circular hole is shown in Figure 36.

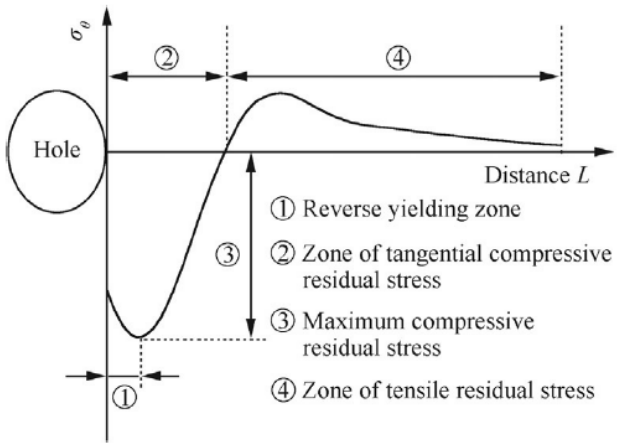

Figure 36 – Typical tangential residual stress distribution around an expanded hole. Source: Yucan, 2015.

The stress fields near a connection hole have a great influence on fatigue life under alternate loads. The residual stresses are also sensitive to the details of the process, particularly the expansion degree and the geometry relation (Yucan, 2015). This way, reaming showed up great results concerning the maximum value and distribution of residual stress (Kang, 2002).

Moreover, the mandrel speed, lubrication and expansion degree interfere in the stress fields. Finally, the geometry relation is fundamental for the component strength. Thus, the edge

distance ratio, $^{e}/_{d}$, influences the residual stress distribution around a cold expanded hole, when it is small, and stops acting on this character for values greater than 3.

2.4 Cold work due to drilling class changing

Cope and Lacy, 2000, studied the effects of changing the material of rivets for variated number of rows, and concluded that the interference in the intensity of stress factors was insignificant. However, they found evidence that the rivet diameter has an important effect on these factors. This way, they showed that increasing the interference between the rivet and the hole, there is a reduction in the stress factor, also in the initial crack growth rates.

This way, besides the cold work effect for fatigue life caused by an external tool, its benefits caused by the drilling class changing were also analyzed to visualize the structural component behavior. It happened because while installing the fastener, which requires higher interference in order to be inserted on the hole, the process generates the cold work itself, since the hole suffer plastic deformation.

Creating cold work through the fastener showed up as a potential solution to increase fatigue life while reducing the productive time that includes eight minutes for each drilled hole to receive the traditional cold work process (EMBRAER, 2018). With the late technique it is possible to cut one of the steps off – there is no need to use an external tool and spend time modifying the hole characteristics before the fastener installation –.

For the present study, half of the specimen with the special drilling class and PULL-STEM pins were tested to prove the effect of the cold work caused only by the class changing and its interference created. The other half, with the regular drilling class and HI-LITE pins, did not receive cold work as usually done by mandrel. The evaluation of the datum acquired was possible through comparison with results of a similar study done for the traditional cold work process in contrast to the straight holes without cold work.

2.5 Previous Works

A widely used technique for cold expansion fastener holes has been developed by Boeing Company in the early 1970s and was firstly used in F/A-18 and other aircraft components (BARTER, 2009). The technique has been applied to critical holes in highly loaded zones of structures, such as landing gears and engine mounting regions (Yucan, 2015).

The cold expansion technology has been used in key fastening holes of various aircraft, as shown in Table 2. Moreover, MIG aircraft in Soviet aviation industry used cold expansion in the girder holes of models like MiG-17, MiG-19, and MiG-21.

Table 2 – Application of the cold work in some aircraft (Adapted from Yucan, 2015).

Strengthening method	Aircraft type	Strengthening position
Cold expansion process	F-16, F-18, B-707, B-747, B-757, B-767, MD-82, F-15, Kfir	Main bearing components
Cold expansion process and interference fit bolting	J-5, DC-9, DC-10	Lower surface of central wing
Cold expansion process and interference fit riveting	B-707	Connection of stiffening profile and skin in the wing box spanner torque wall; connection of stringer and skin in the lower wing panel; connection of fuselage frame and skin

Studies using cold work were done looking for its benefits by changing different alloys. It was seen that the fatigue lives of aluminum alloys were increased more than those of other metals, because of their good ductility. Research results show that the fatigue life of 7050 high-strength aluminum alloy can be increased 6 times using the hole cold expansion process, while that of 7B50-T7451 can be increased 28 times (Yucan, 2015).

However, the gain coefficients of low-plasticity metal materials are relatively smaller. The fatigue lives of Ti6Al4V and 30CrMnSiNi2A can be increased 2.8 times and 1.7 times, respectively, according to the study analyzed. In addition, stress levels also affect the gain coefficient. For example, in the same conditions, the fatigue life improvement factor is about 3.2 and 1.5 for a degree of cold expansion of 5.58% when applying nominal stresses of 191 MPa and 300 MPa, respectively (Yucan, 2015).

Other practical studies focusing on the effects of class changing were done by EMBRAER. For the commercial jet E190-E2, the drilling class of the wing-fuselage assembly

was changed from C4 to C6. This change showed a great improvement in the component fatigue life. Its purpose was to increase the interference on the hole, as previously researched. This way, for three different hole diameters, the class was studied, and the prototype was certified through a real-scale prototype, as shown in Figure 37.

Figure 37 - Embraer E190-E2 certification ultimate load fatigue test. Source: EMBRAER, 2017.

The study concluded that the average fatigue life of class VI joints is equal or better than the average values for class IV joints. It allowed the application of class changing for the commercial aircraft in study. Using this principle, the greater interference caused by the cold work use while changing the usual C6 class to the new fastener special class, it is possible to predict a higher fatigue life for the component chosen.

3 CASES OF INTEREST

3.1 BOAC 1954 flight 781

3.1.1 Accident

The accident happened on 1954, when a de Havilland Comet flying from Rome to London, as shown in Figure 38, operated by British Overseas Airways Corporation – BOAC – as flight 781, suffered an explosive decompression and structural failure 15 minutes after takeoff. Months later, the Comet jet operated by South Africa Airways as flight 201, flying from London to Johannesburg, crashed into the Mediterranean Sea of Naples. (EIT, 2018).

Figure 38 – Accident with BOAC. Source: FLIGHTGLOBAL, 1951.

After both investigations and accident reconstruction, the cause was determined as an in-flight metal fatigue failure, which led to explosive decompression and midair breakup, and the Comet jets disintegrated in the air. The Comet was the first commercial jetliner and had a peculiar design, with squared windows shape. This shape caused the surrounding metal to have extra stress in high altitudes, leading to the metal fatigue.

3.1.2 Opportunities

After the accidents, studies regarding the stress concentration and fatigue failure were enhanced, resulting in new components development. This was one of the first approaches

towards the fatigue improvement in the civil aircraft history, highlighting the importance on new technology evolution and its compromising role on aviation.

3.1.3 Airworthiness improvements

After the accidents, the airplanes were regulated by the Aeronautical Authorities to receive only the windows with rounded corners. By this time, Authorities such as EASA and FAA did not exist, leading to lack of official regulatory documents, such as Service Bulletins, SB, or Airworthiness Directives, AD.

3.2 Aloha Airlines 1988 flight 243

3.2.1 Scenario

The accident happened on April 28, 1988, when a Boeing 737-200, N73711, operated by Aloha Airlines as flight 246, suffered an explosive decompression and structural failure at 24,000 feet, while in route from Hilo, to Honolulu, Hawaii, as shown in Figure 39. After the decompression, approximately 18 feet from the cabin skin and structure aft the cabin entrance door and above the passenger floor line separated from the airplane during flight. The airplane landed safely after an emergency descent to Kahului Airport on the Island of Maui (FAA, 2005).

Figure 39 – Overload separation during Aloha Airlines Flight 246. Source: Seelio, 2016.

According to The National Transportation Safety Board, the failure of the Aloha Airlines was due to an inadequate Maintenance Program, which did not detect the presence of significant disbonding and fatigue damage on the airplane, which lead to accident. Additionally, the FAA had failed to properly evaluate the Aloha Airlines maintenance program.

3.2.2 Opportunities

Since the accident, new failure modes due to fatigue were proposed and the MWD started being widely studied, generating new requirements for maintenance inspection. Also, the Alert Service Bulletin SB 737-53A1039 proposed by Boeing had a terminated action taken in order to inspect all the lap joints. Finally, the manufacturing difficulties found in the B-737 with respect to the cold bond lap joint, which resulted in low bond durability, corrosion, and premature fatigue cracking, were analyzed in order to prevent further failures.

3.2.3 Airworthiness improvements

Safety issues were proposed and required from FAA after the report regarding the accident, which ended in Airworthiness directives 89-09-03 and 89-11-06 R1. The first one requires a repair on all lap joints to prevent decompression of the airplane, while the second one anticipates the need for inspections, and modifying the Maintenance Program in order to prevent failure of the forward lower cargo compartment frames.

4 COMPUTATIONAL SIMULATION

4.1 Mathematical model

The mathematical model that represents the specimen itself was done based on a rigid-spring model, where the plates represents rigid bodies, and the pins were considered as spring bodies. Doing so, it was possible to neglect the pins mass, and assume that it acted as the freedom degree of the whole specimen, once the plates depend on them to react to any inputs of movements. This method is resumed by the forces acting on the body, resulting in the Bypass and Load-transfer forces described in section 2.1.2. Also, the K_T, which correlates the forces applied on the body, was found through the method explained on the items 2.1.4.1, and 2.1.4.2, where the curves of each parameter should be analyzed.

4.2 Loading definition

In order to run the real fatigue tests with the specimens, it was stablished that the fracture should happen after a number near to 100,000 cycles. Then, the load distribution was estimated based on the S-N curves, for a notched and an unnotched plate.

The load was analyzed based on the metallic material and fastener system allowables, according to FAA MMPDS04 Handbook, 2008, as previously explained in section 2.1.4.2. Looking throughout the tables provided by the handbook, it was possible to find out which was the force supported by the plates, when it had a geometrical discontinuity, considering that it was notched, with a $K_T = 3$. The curves plotted to this case are shown in Figure 40.

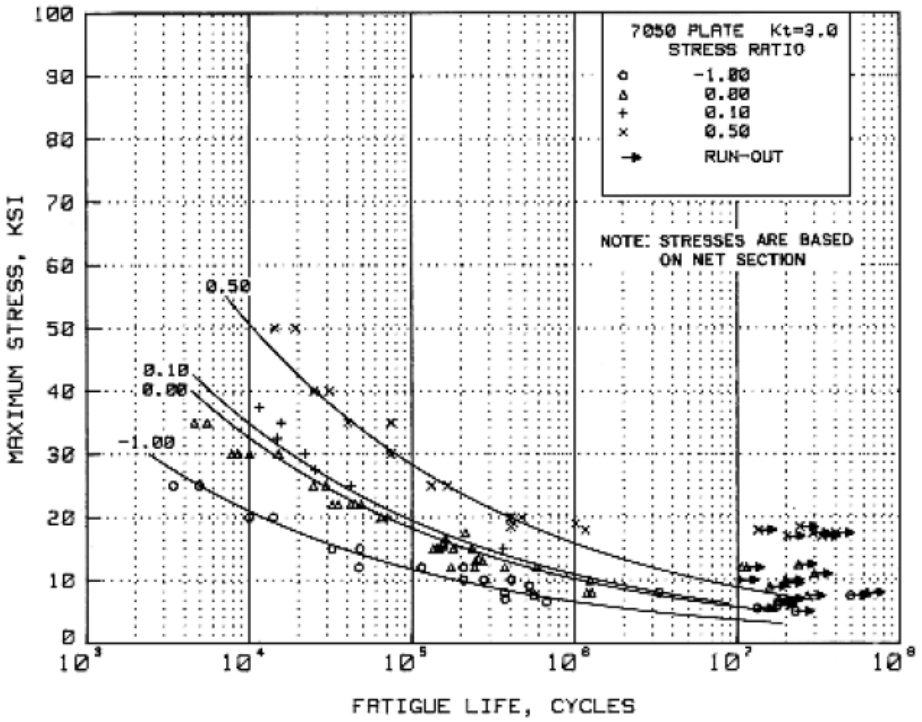

Figure 40 - Best-fit S-N curves for notched, K_T=3, 7050-T7451 plate, longitudinal and long transverse directions. Source: FAA, 2008.

The first analysis, for a stress ratio of 0.10 – which does not consider the buckling effects on the specimen, and make a good correlation to the real cases, where the ratio 0.00 could not be attained –, resulted on a load of 20ksi, for a damage on 100,000 cycles. Also, the value for the load in the case when the plate is unnotched, or does not have any geometrical discontinuity, was found from the curves shown in Figure 41.

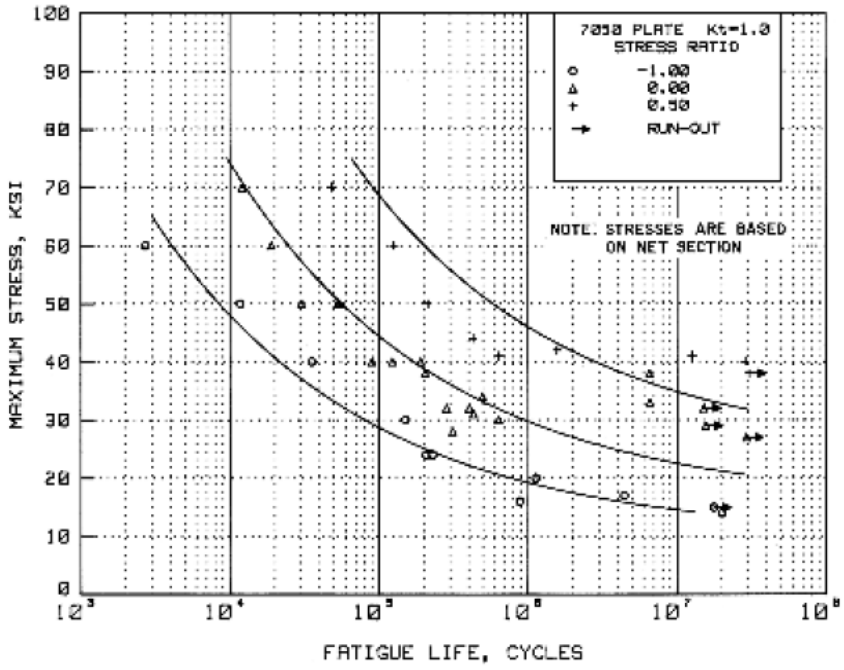

Figure 41 - Best-fit S-N curves for unnotched, 7050-T7451 plate, longitudinal and long transverse directions. Source: FAA, 2008.

For this case, the stress ratio used was 0.50, maintaining the same principle used for the first analysis, and the load for the 100,000 cycles that should lead to failure was found as approximately 45ksi. Then, it was assumed that the value in which the body should fail nearby the hole area would be close to 45ksi. This conclusion was based on the resistance variation increased by the pins inside the holes, which represents the geometrical discontinuities. With opened holes, the value is the minor of all the analyzed ones, since it reduces the resistance of the material, causing deformities that lead to the fatigue-fracture process.

It is important to notice that the HSL and HST pins datasheet, available at Appendixes A and B, respectively, show that both have a double shear equivalent to 21000ksi, which is higher enough than the calculated ultimate load for the fracture of the plates. This way, it is possible to assume the pins resist to the load of 45ksi, without compromising the validity of the tests, in compliance with the LOV presented in section 2.2.

Hence the load and the cycles were predicted, and it was possible to execute further simulations using Finite Element Model on CATIA®, and a more accurate number was calculated for the destructive experiment. Thus, the mesh size, force applied, and initial loading to make the cycling tests were searched, as it will be further explained. All the parameters had the uncertainty of the Software, for both manufacturing processes types. For this was assumed that all the models should support the quantity of imposed cycles, with same loading acting on

the specimens, going on the direction of the cold work theory about improving the fatigue life of a structural component.

4.3 Model definition

All the analysis described afterwards were done using the finite element model available on the software CATIA®.

During the first analysis part, the mesh size was defined, based on an aluminum alloy specimen, with a joint made of four fasteners of titanium alloy Ti-6Al-4V. The specimen was designed using CATIA® part design and assembly modes, containing two aluminum alloy plates, with dimensions based on a hole with 9.5 mm diameter, resulting in the dimensions shown in Table 3.

Table 3 – List of dimensions

Element	Size in diameters	Size in mm
Holes diameter	1	9.5
Distance between holes centers	4	38
Distance from hole center to plate border on width	2	19
Plates length	16	152
Plates width	8	76
Plates thickness	-	7.5

The type of plates union selected aimed to simulate the worst-case scenario, in which tension and shear stress act on the component. In the case of a multiple-joint, when there is a triple plate union, the tension force is worthless due to the third plate to stabilize the joint.

The mesh was defined by the following external conditions:

- Homogeneous applied forces distribution on the surfaces, through a smoothness tool available in the software;
- One of the aluminum plates had the external free surface clamped, through the longitudinal direction;
- Load application on the free surface of the other plate, along the longitudinal direction, ignoring momentum and displacement that could occur in the other axis – it was possible through another software tool.

Simultaneously, the inner conditions applied on the specimen were:

- Pins represented by rigid springs, ignoring the friction between them and the hole surface;
- Friction between the aluminum plates, as in the real model.

The specimen with the imposed conditions is shown in Figure 42.

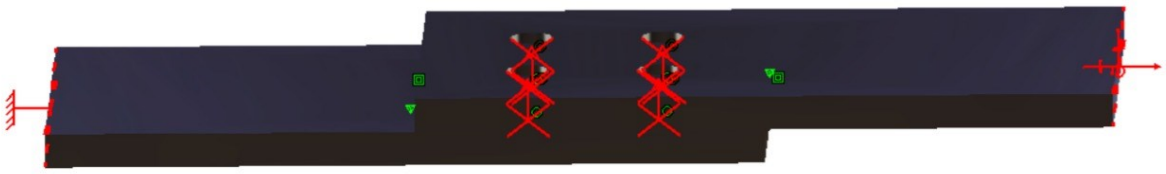

Figure 42 – Simulated specimen with the respective conditions applied. Source: author.

It is important to notice that the friction should be considered negligible for all the cases simulated, in order to analyze the worst-case scenario – once there is an acting force applied on the plates, it is only supported by the fasteners and plates, despite the friction resistance that is seen in the real case tests –. However, the software applies some restrictions on this type of simulation, creating a non-representative scenario when the friction between the plates is neglected. Although, there is a little margin between the real case – when the destructive test is executed, hence a friction force contributes to resist the loads happening on the specimen –, and the computational simulation, because the friction between the pins and holes was neglected.

4.3.1 Mesh size

Initially, the specimen was designed for a mesh with 5mm in global size, corresponding to 0.05 times the established size of the hole. Moreover, the mesh was calculated using a tetrahedral element with parabolic edges. Also, a local size of 1mm was put onto the holes area, looking for a better approximation. This local mesh was used for all the meshes simulated. It is important to notice that the inner and outer conditions imposed to the specimen were the same during all the modifications in this step.

The mesh had its size reduced in order to verify the analyzed data conversion, looking forward to the best simulation mesh size. The requirements imposed to achieve this size were the best precision and visibility of parameters.

A generic force of 10kN was applied for the first four sizes of mesh simulation, varying only the size of the mesh to find the best one based on its behavior – here it was considered the

convergence to regular values of stresses and displacements, amongst the minor error, which are the parameters given by the Software and further explained.

For the first simulation done, using a 5mm mesh, Figures 43, 44, and 45 show, respectively, the translational displacement suffered by the specimen; Von Mises forces acting on the specimen; and the principal stresses, all generated by the Software interface during the simulation.

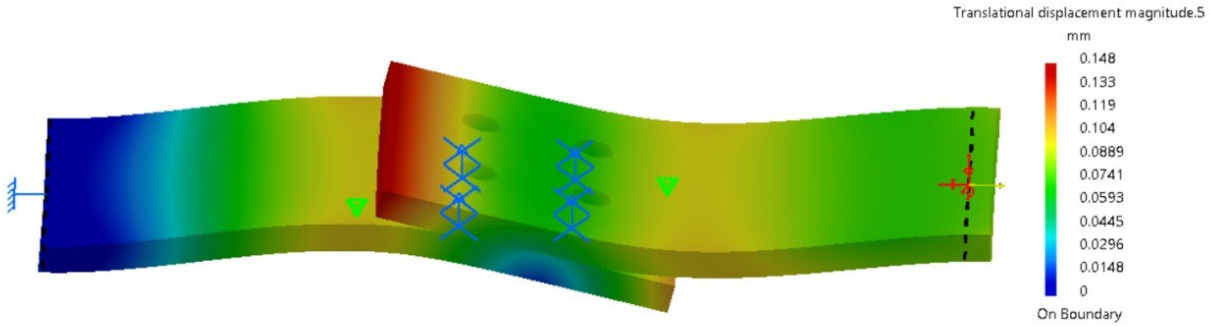

Figure 43 – Displacement observed for a 5mm mesh with 10kN force applied. Source: author.

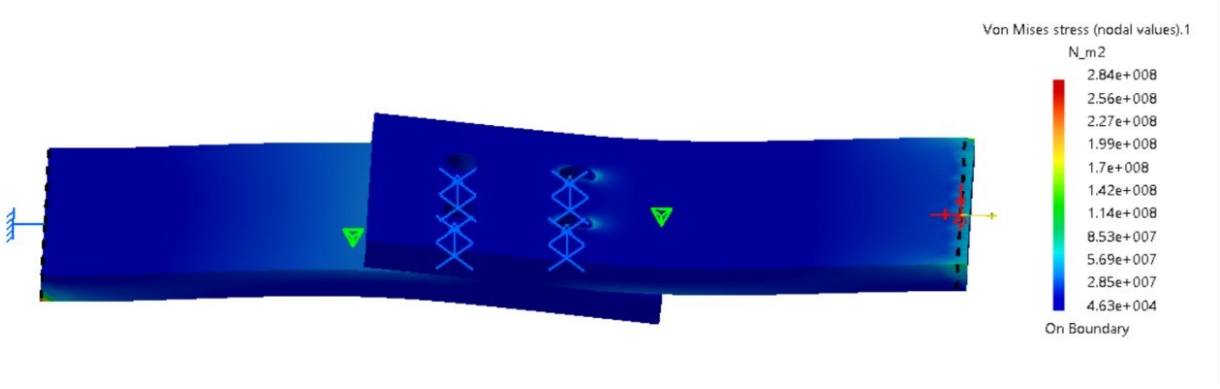

Figure 44 – Von Mises stress observed for a 5mm mesh with 10kN force applied. Source: author.

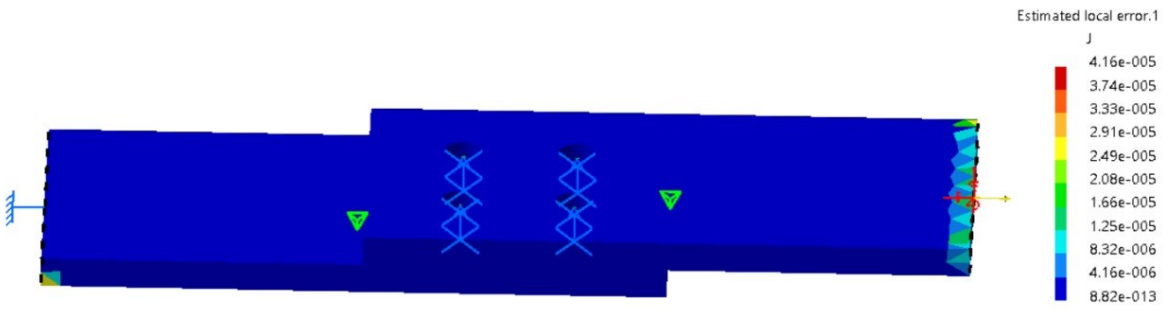

Figure 45 – Error observed for a 5mm mesh with 10kN force applied. Source: Author.

Furthermore, the second test was done in a specimen with a 4mm mesh, also using the same force of 10kN applied on the first case; the third sample was a specimen with a 3mm mesh; and the fourth specimen had a 2mm mesh, all with the same force of 10kN. The results were similar, and after the analysis, the maximum values obtained for each mesh size were put in Table 4.

Table 4 – Maximum values for parameters of different mesh sizes

Mesh size [mm]	Von Mises Stresses [N/m^2]	Displacement[mm]	Error [J]
5	2.84e+8	0.148	4.16e-5
4	2.91e+8	0.148	2.61e-5
3	2.8e+8	0.146	8.78e-6
2	3.02e+8	0.146	4.33e-6

Through this process, it was possible to conclude that the most precise size – when the values trend to converge –, with the minor error, was found for the 2mm mesh. With new attempts to reduce the mesh size, it was possible to notice that the improvement in the parameters analyzed was not significant and the error was not reduced, due to software limitations.

4.3.2 Force definition

After this first approach, using the chosen mesh size of 2mm, the second phase of simulation consisted of applying different values of forces, in order to obtain the best approximation to the load calculated as 45 Ksi, or 3.10e+8 N/m^2, within the requirements in visualization and precision given by the Software. The parameters analyzed during this step refer to the Von Mises Stress achieved on the holes area and the precision attained.

For the first case, the new force applied was equivalent to 50kN, and the illustrative results are presented in Figures 46, 47 and 48.

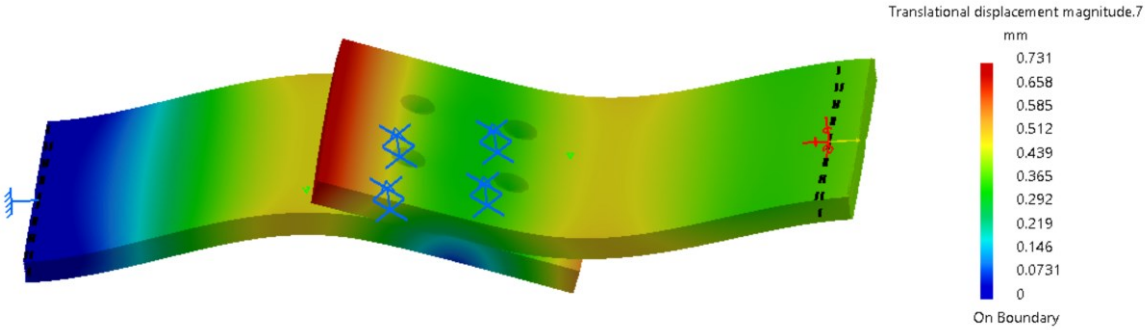

Figure 46 – Displacement observed for a 2mm mesh with 50kN force applied. Source: author.

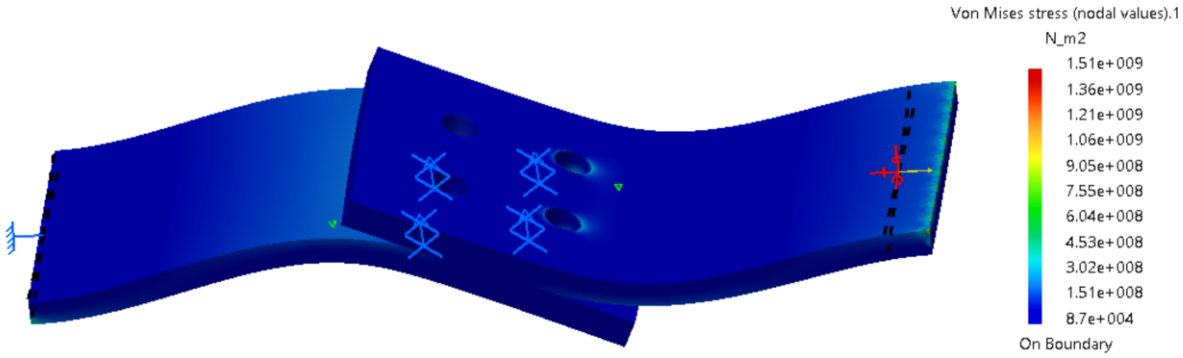

Figure 47 – Von Mises stress observed for a 2mm mesh with 50kN force applied. Source: author.

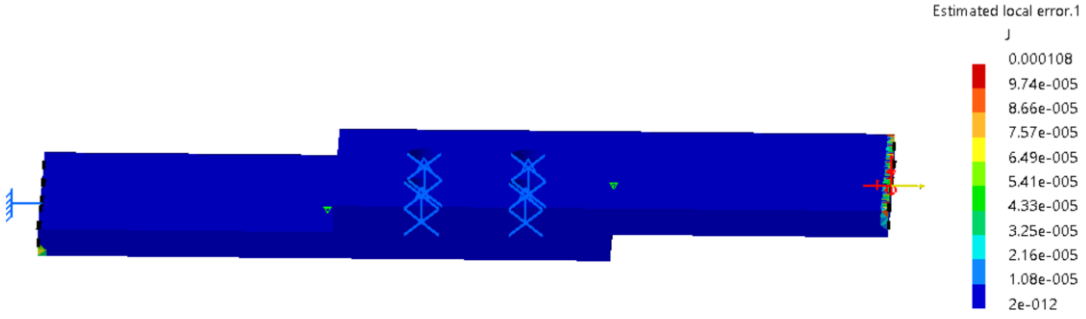

Figure 48 – Error observed for a 2mm mesh with 50kN force applied. Source: author.

Once the 50kN load caused a stress superior than the $45Ksi$ around the hole, a new simulation was done for an applied force of 25kN, acting in the 2mm mesh specimen. New force of 30kN was also applied, and all the results are show in Table 5.

Table 5 – Maximum values on hole area for 2mm mesh parameters with different forces applied

Force applied [kN]	Von Mises Stresses $[N/m^2]$	Displacement[mm]	Error [J]
25	3.02e+8	0.175	5.59e-9
30	4.26e+8	0.248	3.16e-8
50	7.17e+8	0.409	2.25e-6

It was possible to conclude that a minor error occurred when the force of 25kN was applied to the specimen. However, for the 30kN force, the Von Mises stresses observed on the specimen were closer to the calculated value, followed by a quicker conversion of the error than in the cases of a bigger force applied.

The maximum value for Von Mises stress was not considered, since it was visible that the hole had the maximum stresses, representing the fracture beginning, once it achieved the values between the blueish and greenish area on label. Thus, these were the values analyzed, and the highest of them was put into Table 4.3. For the chosen value of 30kN force, it was possible to see a zone of stresses varying from 1.83e+8 N/m^2 and 4.26e+8 N/m^2 inside the blueish-greenish area, which includes the searched value of 3.10e+8 N/m^2. All the comparisons were made for the same mesh size of 2mm and Figures 49, 50 and 51 show the Von Mises stress on the specimen, the zoomed area around the hole in cut, and a comparative figure with the Von Mises Stress, Displacement, and deformation of the specimen, respectively.

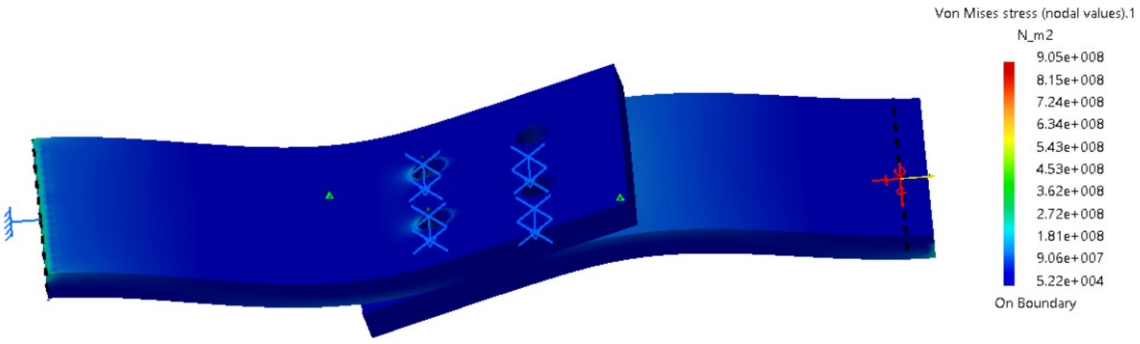

Figure 49 – Von Mises stress observed for a 2mm mesh with 30kN force applied. Source: author.

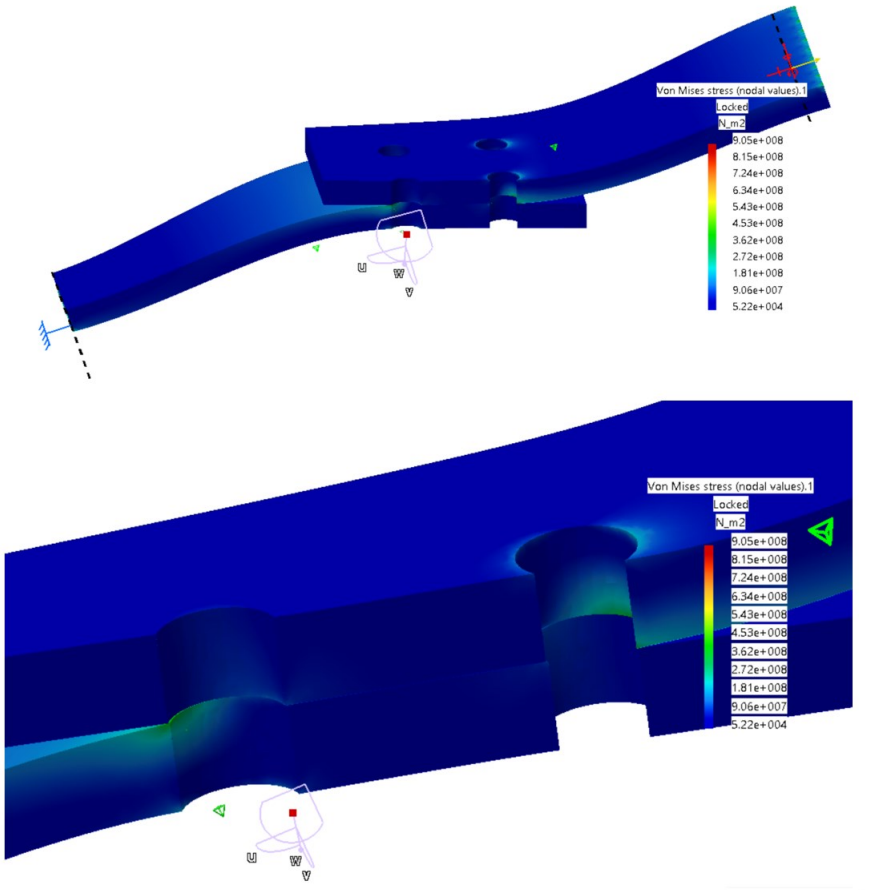

Figure 50 – Cut section of the specimen for a 2mm mesh with 30kN force applied. Source: author.

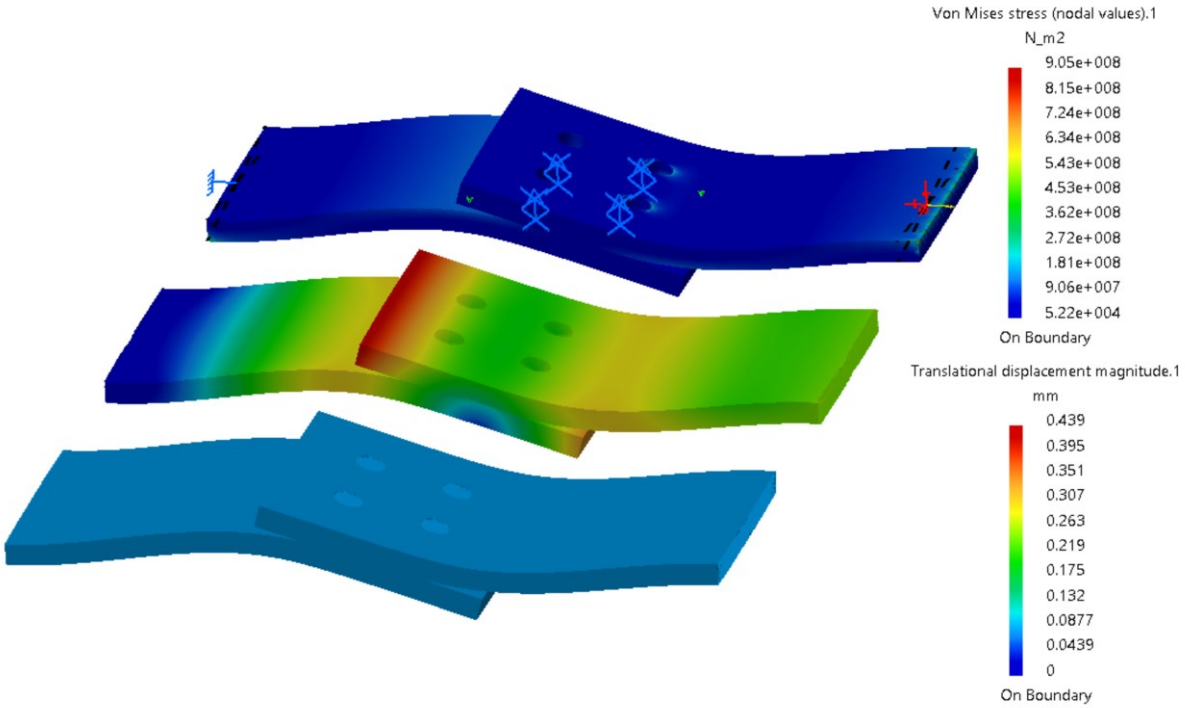

Figure 51 – Comparative Von Mises Stress, Displacement and Deformation of the specimen for a 2mm mesh with 30kN force applied. Source: author.

4.4 Load simulated

The next step was to compare the K_T obtained through the simulation and the one obtained through NIU, 1995, calculations, using computation in Appendix C, and this yielded a result of a $K_T = 4.99$. This step aimed for the best correspondence between the software FEM and the literature calculation.

Using the maximum value of Von Mises Stresses given to the hole area while applying a 30kN load to the model, or 4.26e+8 N/m^2, and the net stresses in the region between the holes, or 8.5e+7 N/m^2, it was possible to find $K_T = 5.01$. However, there is no predicted S-N curve by NIU,1999, that describes the joint behavior for this value. By extrapolating the values given by a $K_T = 1$ and using the computation in Appendix D, it was possible to find a K_T stress value equivalent to 55 Ksi, or 3.52e+8 N/m^2, and a net stress equivalent to 10.17 Ksi, or 7.01e+7 N/m^2. Multiplying the net area by the net stress – which leads to a relative error of 2.1e+6 N/m^2 compared to the same simulated value –, through theory described on topic 2, it is possible to find a 32.5kN load. Thus, the software gave an absolute error of 2.5kN, in comparison to the background calculation.

5 MATERIALS AND METHODS

5.1 Specimen construction

5.1.1 Plates tooling

The first step of the experimental analysis was to build the model. This way, the plates were machined out of a bigger piece of 7050 enriched aluminum alloy, totalizing 72 individual plates. The width was reduced to achieve 7,5mm as defined on project, and machined till they had the dimension of 154mm per 72mm, as shown in the sketch used for manufacturing script, in Figure 52.

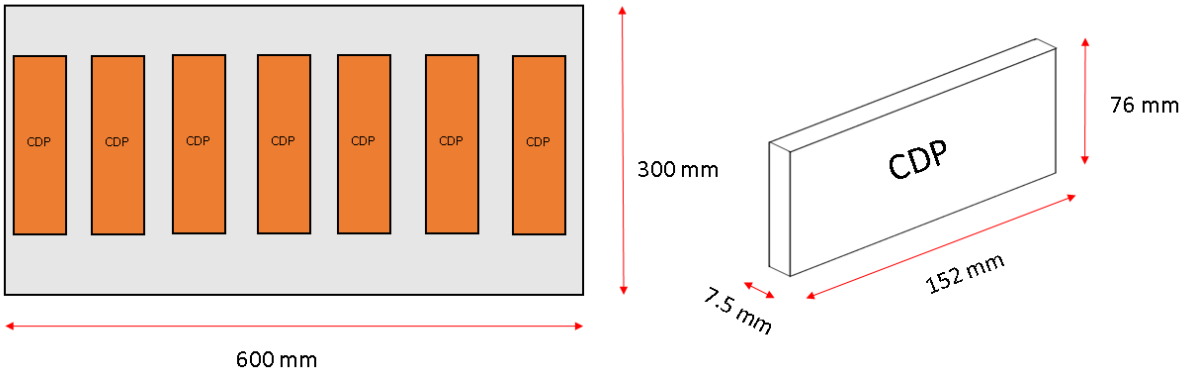

Figure 52 - Plate schematic tooling. Source: author.

Figure 53 shows the real plates after tooling.

Figure 53 - Plates ready to be drilled. Source: author.

5.1.2 Plates drilling

The following step after machining was to separate half of the plates as HST class and HSL class. Subsequently, they were marked according to the project design, shown in Figure 54, following the dimensional tolerances. Moreover, they were measured with an ABS Digimatic Caliper Series 500, Mitutoyo, as shown in Figure 55.

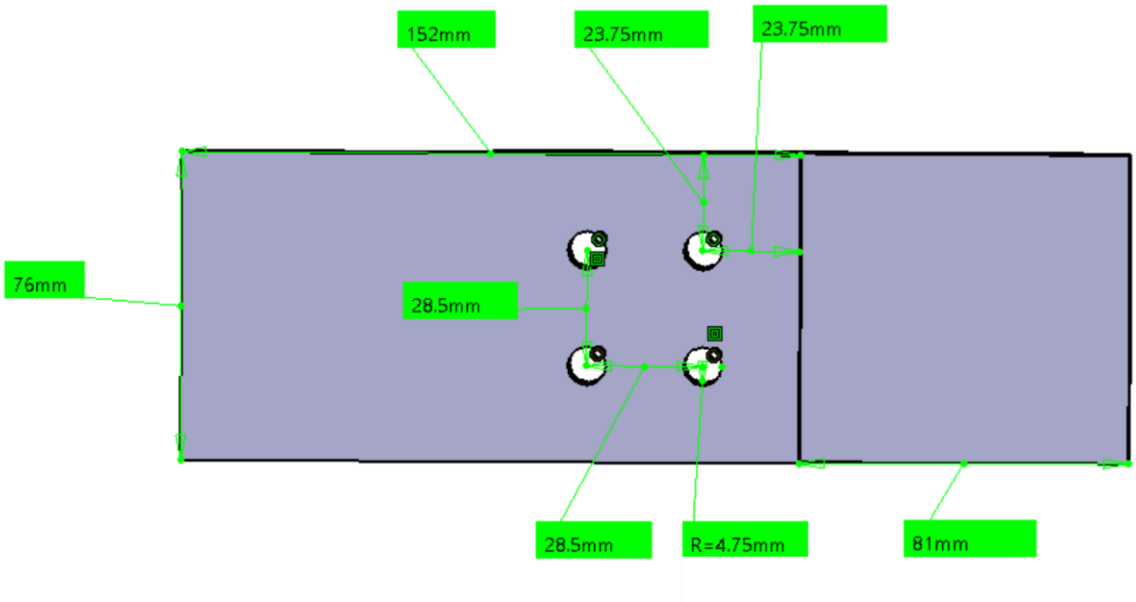

Figure 54 - Plates dimension, done through CATIA®. Source: author.

Figure 55 - Plates marking and measurement. Source: author.

The technical data of the caliper is:

- Accuracy: Refer to the list of specifications;
- Resolution: 0.01mm or .0005"/0.01mm;
- Repeatability: 0.01mm / .0005”;
- Length standard: ABSOLUTE electrostatic capacitance type linear encoder.

In order to guarantee that the different interference classes are properly represented in the tests, the specimens were fabricated using drilling tools dimensioned to produce holes with sizes significantly different between configurations. According to the hole tolerance available on NE03-006, EMBRAER, 2018, for HST 3/8”, or nominal diameter of 9.5mm, class IV, the tolerance for diameter should vary from 9,462mm to 9,487mm, according to Figure 56, while for HSL 3/8”, or nominal diameter of 9.5mm, the tolerance for diameter, without over, should vary from 9,427mm to 9,467mm, according to Figure 57.

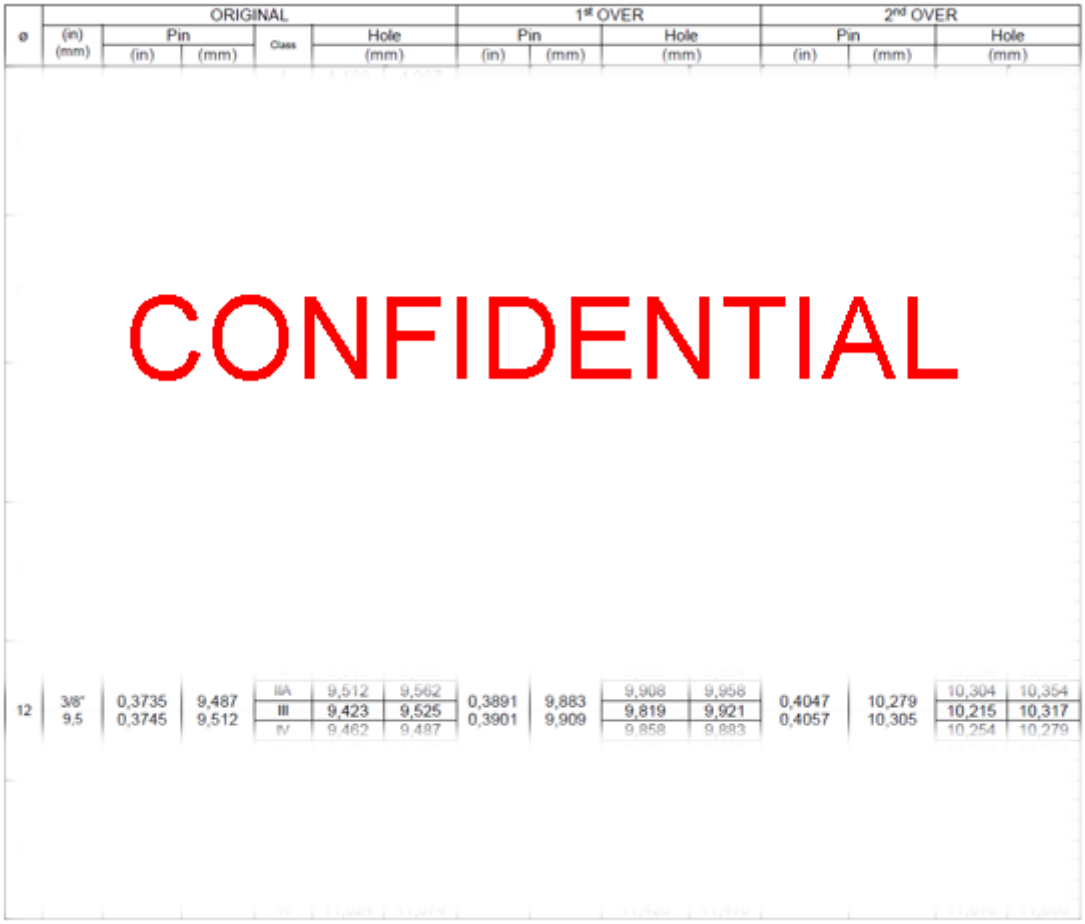

ø	(in) (mm)	ORIGINAL Pin (in)	Pin (mm)	Class	Hole (mm)	1st OVER Pin (in)	Pin (mm)	Hole (mm)	2nd OVER Pin (in)	Pin (mm)	Hole (mm)
12	3/8" 9,5	0,3735 0,3745	9,487 9,512	IIA	9,512	9,562	0,3891 0,3901	9,883 9,909	9,908 9,819 9,858	9,958 9,921 9,883	0,4047 0,4057	10,279 10,305	10,304 10,215 10,254	10,354 10,317 10,279
				III	9,423	9,525								
				IV	9,462	9,487								

Figure 56 - Dimensional limits of hole diameter for HI-LOK, HI-LITE and LOCKBOLT LGPL pins. Source: EMBRAER, 2018.

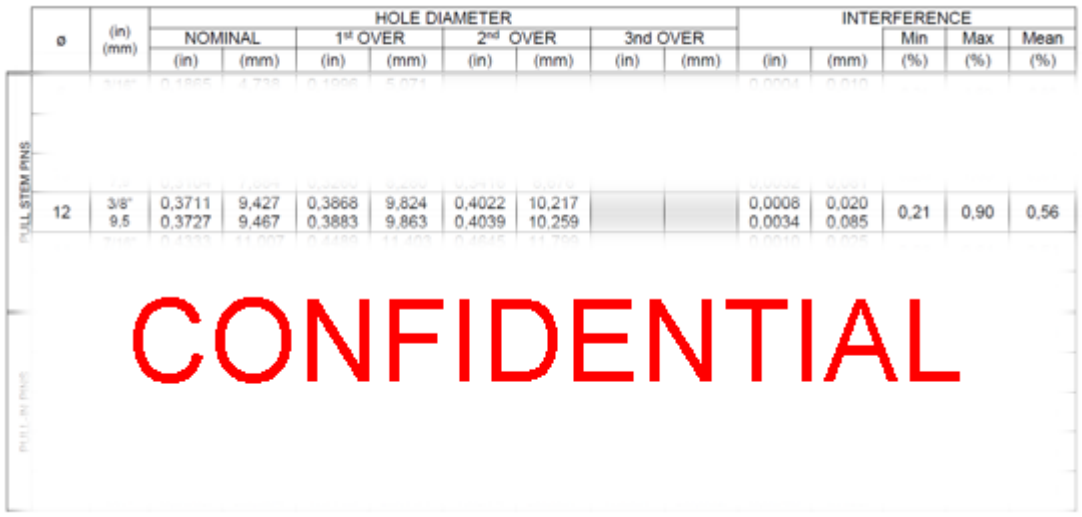

ø	(in) (mm)	HOLE DIAMETER NOMINAL (in)	NOMINAL (mm)	1st OVER (in)	1st OVER (mm)	2nd OVER (in)	2nd OVER (mm)	3nd OVER (in)	3nd OVER (mm)	INTERFERENCE (in)	(mm)	Min (%)	Max (%)	Mean (%)
12	3/8" 9,5	0,3711 0,3727	9,427 9,467	0,3868 0,3883	9,824 9,863	0,4022 0,4039	10,217 10,259			0,0008 0,0034	0,020 0,085	0,21	0,90	0,56

Figure 57 - Dimensional limits of hole diameter for HSL/HPL pins. Source: EMBRAER, 2018.

After the drilling process, all the holes of each specimen were measured by minimum and maximum diameter, in order to guarantee a correct configuration and interference fit level. The measurements were done using an S_Dial WORK Basic comparator, Sylvac, as shown in Figure 58.

Figure 58 - Comparator used to measure the holes diameter. Source: author.

The technical data of the comparator is:

- Measuring range: 50mm
- Resolution: 0.001mm or .0005"/0.01mm
- Repeatability: 2µm
- Maximum error: 7µm

The values measured were displayed on table 6.

Table 6 – Dimensional size of holes measured

Hole number	HST		HSL	
	MinØ (mm)	MaxØ (mm)	MinØ (mm)	MaxØ (mm)
1	9,476	9,477	9,445	9,445
2	9,475	9,476	9,443	9,446
3	9,475	9,478	9,446	9,446
4	9,475	9,476	9,442	9,444
5	9,476	9,476	9,454	9,459
6	9,476	9,477	9,460	9,460
7	9,476	9,477	9,441	9,441
8	9,476	9,477	9,450	9,454
9	9,487	9,487	9,444	9,446
10	9,486	9,487	9,442	9,447
11	9,486	9,487	9,443	9,446
12	9,485	9,486	9,445	9,445

Hole number	HST		HSL	
	MinØ (mm)	MaxØ (mm)	MinØ (mm)	MaxØ (mm)
13	9,471	9,474	9,443	9,444
14	9,475	9,477	9,446	9,447
15	9,476	9,476	9,443	9,449
16	9,474	9,474	9,456	9,458
17	9,473	9,474	9,461	9,461
18	9,476	9,476	9,453	9,453
19	9,475	9,475	9,448	9,449
20	9,476	9,476	9,462	9,463
21	9,475	9,477	9,461	9,466
22	9,473	9,474	9,460	9,463
23	9,473	9,474	9,463	9,467
24	9,473	9,474	9,458	9,461
25	9,475	9,476	9,440	9,443
26	9,476	9,477	9,442	9,447
27	9,478	9,487	9,440	9,441
28	9,477	9,477	9,443	9,444
29	9,475	9,475	9,444	9,448
30	9,474	9,474	9,443	9,444
31	9,474	9,474	9,444	9,445
32	9,475	9,475	9,444	9,445
33	9,476	9,476	9,445	9,446
34	9,476	9,476	9,445	9,446
35	9,476	9,476	9,445	9,445
36	9,475	9,475	9,445	9,446
37	9,476	9,476	9,445	9,445
38	9,476	9,476	9,444	9,444
39	9,476	9,476	9,446	9,447
40	9,475	9,475	9,442	9,447
41	9,476	9,485	9,446	9,448
42	9,474	9,476	9,442	9,446
43	9,476	9,476	9,443	9,446
44	9,478	9,484	9,448	9,448
45	9,475	9,476	9,443	9,443
46	9,475	9,476	9,444	9,445
47	9,474	9,475	9,458	9,461
48	9,474	9,478	9,448	9,459
49	9,474	9,478	9,448	9,448
50	9,474	9,474	9,447	9,448
51	9,482	9,482	9,448	9,449
52	9,474	9,474	9,447	9,448
53	9,474	9,474	9,447	9,447
54	9,475	9,475	9,446	9,446
55	9,475	9,475	9,447	9,448

Hole number	HST		HSL	
	MinØ (mm)	MaxØ (mm)	MinØ (mm)	MaxØ (mm)
56	9,475	9,479	9,447	9,448
57	9,487	9,487	9,443	9,443
58	9,485	9,486	9,441	9,441
59	9,485	9,485	9,442	9,442
60	9,486	9,486	9,441	9,443
61	9,487	9,487	9,444	9,444
62	9,487	9,487	9,444	9,445
63	9,487	9,487	9,443	9,444
64	9,487	9,487	9,443	9,444
65	9,486	9,486	9,443	9,443
66	9,485	9,486	9,444	9,444
67	9,485	9,486	9,442	9,443
68	9,486	9,486	9,443	9,444
69	9,487	9,487	9,443	9,445
70	9,487	9,487	9,443	9,443
71	9,484	9,485	9,443	9,444
72	9,483	9,485	9,443	9,445

Using the data acquired, Figures 59 and 60 were plotted showing that the dimensional limits were respected for all of the holes measured.

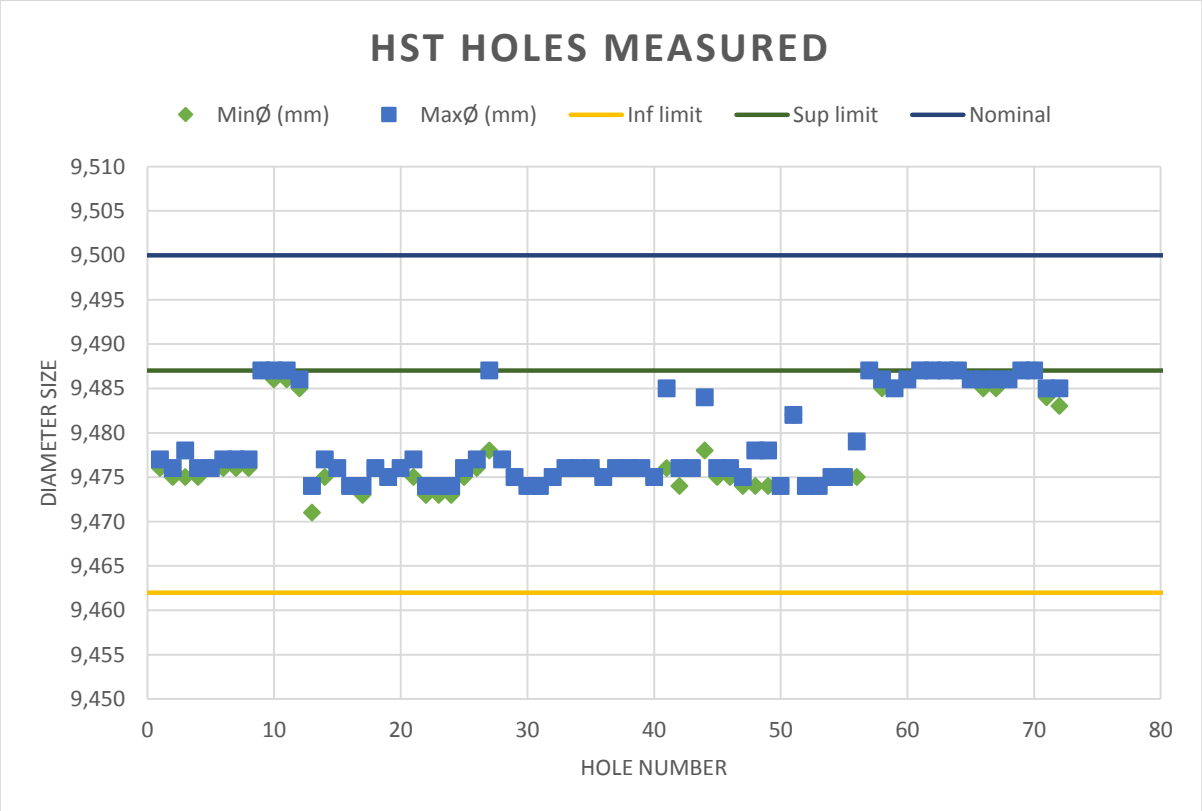

Figure 59 – HST holes diameter. Source: author.

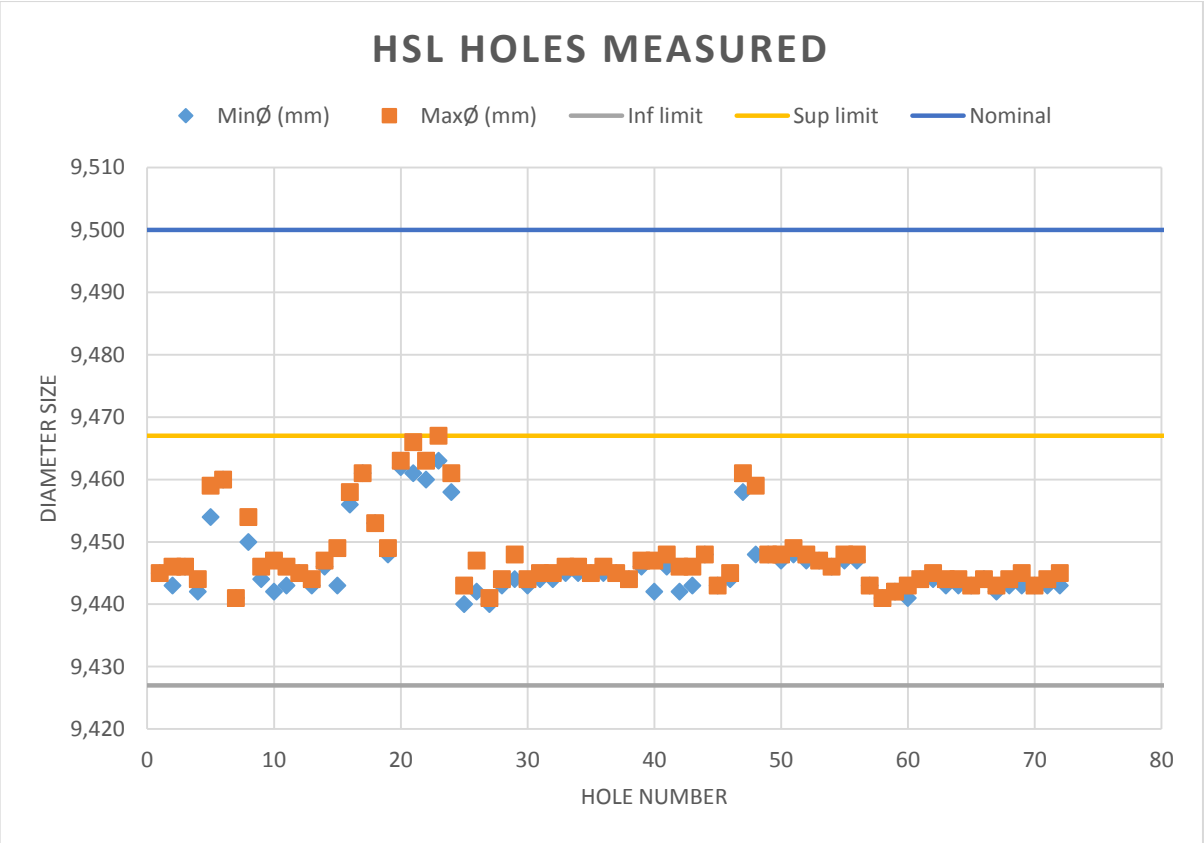

Figure 60 – HSL holes diameter. Source: author.

5.1.3 Cold work

The cold work process was only done for half of the specimens, through the elevated interference fitting between the HSL pins and the holes of the plates. This way, no additional work was needed, despite the process of riveting the plates, after cleaning and sealing. It is important to notice that since the level of interference fitting was higher for HLS than for HST pins, it was necessary to use machinery to pull the first type of pins inside the holes, different of the regular process made with a rivet gun, as it will be explained on the next item below.

5.1.4 Riveting

For the riveting process, the first step was to measure the shank diameter of each pin, looking for compliance with the tolerance described in Appendix A, for HSL pins, and in Appendix B, for HST pins. The tolerances adopted were the same, since the HST 3/8”, or 9.5mm nominal diameter, receives an aluminum coating, also there are no further specifications for HSL 3/8”. Then, the shank dimensions should vary from 9,4869mm to 9,5123mm for both the cases. The measurements were done using a Coolant Proof Micrometer Series 293-with Dust/Water Protection Conforming to IP65 Level, Mitutoyo, as shown in Figure 61.

Figure 61 - Micrometer used to measure the pins shank diameter. Source: author.

The technical data of the micrometer is:

- Resolution: 0.001mm or .00005"/0.001mm
- Flatness: 0.3µm/.000012”
- Parallelism: 1µm/.00004” for models up to 50mm/2”
- Dust/Water protection level: IP65

The measurement results were displayed on Table 7.

Table 7 – Dimensional size of pins measured

Pin number	HST12BJ-12-9			HSL1416NKA12-9		
	Ø1 (mm)	Ø2 (mm)	Ø3 (mm)	Ø1 (mm)	Ø2 (mm)	Ø3 (mm)
1	9,496	9,502	9,505	9,499	9,500	9,501
2	9,490	9,496	9,497	9,500	9,500	9,502
3	9,499	9,505	9,507	9,505	9,502	9,504
4	9,499	9,494	9,491	9,502	9,500	9,501
5	9,498	9,504	9,503	9,509	9,505	9,512
6	9,503	9,505	9,496	9,505	9,503	9,505
7	9,512	9,493	9,496	9,500	9,496	9,494
8	9,495	9,512	9,508	9,504	9,501	9,501
9	9,503	9,506	9,511	9,506	9,501	9,503
10	9,488	9,500	9,505	9,498	9,497	9,500
11	9,496	9,506	9,504	9,504	9,502	9,507
12	9,498	9,500	9,502	9,500	9,497	9,498
13	9,508	9,505	9,512	9,494	9,495	9,500
14	9,508	9,503	9,509	9,508	9,508	9,505
15	9,499	9,496	9,498	9,499	9,501	9,506
16	9,496	9,505	9,501	9,503	9,506	9,503
17	9,496	9,500	9,502	9,505	9,503	9,503
18	9,496	9,499	9,495	9,508	9,510	9,512
19	9,502	9,507	9,495	9,499	9,498	9,501
20	9,496	9,499	9,496	9,501	9,500	9,501
21	9,500	9,505	9,507	9,504	9,502	9,505
22	9,494	9,500	9,503	9,497	9,494	9,497
23	9,510	9,494	9,497	9,505	9,508	9,505
24	9,497	9,497	9,497	9,509	9,508	9,507
25	9,495	9,494	9,498	9,497	9,498	9,497
26	9,506	9,506	9,502	9,497	9,499	9,501
27	9,503	9,502	9,504	9,495	9,498	9,501
28	9,489	9,490	9,491	9,508	9,508	9,509
29	9,502	9,504	9,503	9,510	9,507	9,505
30	9,493	9,495	9,500	9,506	9,506	9,505
31	9,495	9,508	9,512	9,505	9,503	9,505
32	9,497	9,495	9,498	9,503	9,504	9,508
33	9,500	9,505	9,504	9,502	9,503	9,505
34	9,499	9,502	9,498	9,503	9,504	9,502
35	9,501	9,500	9,502	9,510	9,511	9,511
36	9,488	9,496	9,491	9,500	9,500	9,504
37	9,496	9,500	9,502	9,499	9,499	9,497
38	9,496	9,488	9,493	9,510	9,503	9,508
39	9,504	9,499	9,499	9,503	9,508	9,509
40	9,496	9,502	9,496	9,498	9,501	9,501
41	9,509	9,500	9,501	9,505	9,508	9,501

Pin number	HST12BJ-12-9			HSL1416NKA12-9		
	Ø1 (mm)	Ø2 (mm)	Ø3 (mm)	Ø1 (mm)	Ø2 (mm)	Ø3 (mm)
42	9,504	9,497	9,498	9,504	9,505	9,511
43	9,497	9,498	9,498	9,498	9,496	9,501
44	9,495	9,500	9,510	9,506	9,503	9,501
45	9,503	9,505	9,503	9,495	9,496	9,500
46	9,504	9,504	9,507	9,506	9,504	9,504
47	9,502	9,510	9,495	9,504	9,504	9,506
48	9,504	9,509	9,507	9,507	9,506	9,506
49	9,507	9,503	9,504	9,497	9,498	9,500
50	9,498	9,501	9,509	9,494	9,498	9,499
51	9,497	9,498	9,502	9,493	9,492	9,496
52	9,494	9,504	9,498	9,502	9,506	9,503
53	9,502	9,502	9,506	9,503	9,504	9,504
54	9,487	9,500	9,498	9,503	9,504	9,506
55	9,493	9,489	9,495	9,508	9,506	9,508
56	9,491	9,497	9,500	9,499	9,500	9,502
57	9,500	9,500	9,502	9,503	9,506	9,501
58	9,509	9,495	9,501	9,502	9,502	9,500
59	9,497	9,500	9,494	9,500	9,503	9,500
60	9,500	9,502	9,497	9,508	9,509	9,508
61	9,498	9,497	9,503	9,503	9,505	9,504
62	9,499	9,505	9,506	9,506	9,505	9,508
63	9,501	9,503	9,501	9,502	9,503	9,507
64	9,506	9,509	9,504	9,509	9,505	9,503
65	9,494	9,502	9,505	9,508	9,506	9,503
66	9,499	9,498	9,500	9,497	9,495	9,496
67	9,498	9,502	9,504	9,501	9,503	9,506
68	9,502	9,503	9,501	9,504	9,501	9,503
69	9,504	9,504	9,502	9,498	9,500	9,502
70	9,491	9,496	9,493	9,500	9,504	9,503
71	9,499	9,506	9,492	9,503	9,500	9,501
72	9,500	9,501	9,503	9,497	9,503	9,502

The measurements were displayed in Figures 62 and 63.

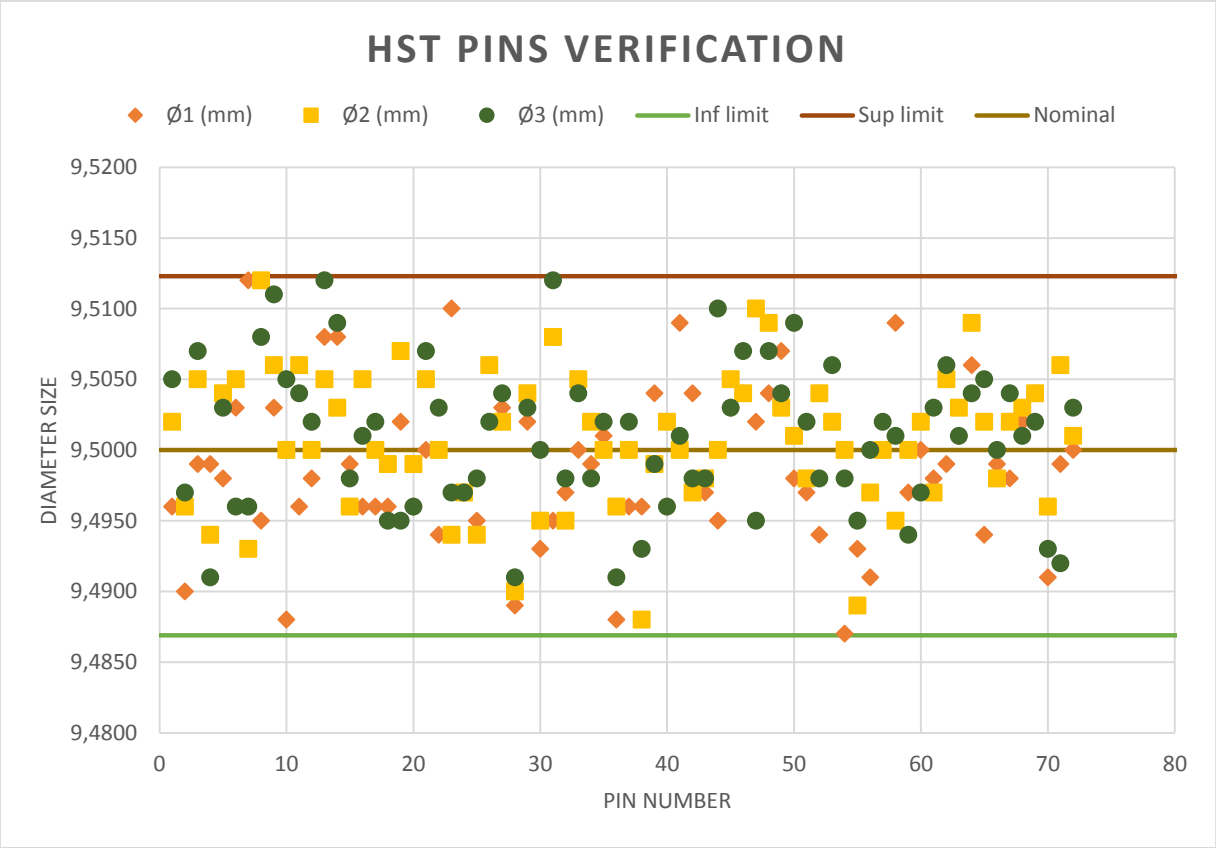

Figure 62 – HST pins diameter. Source: author.

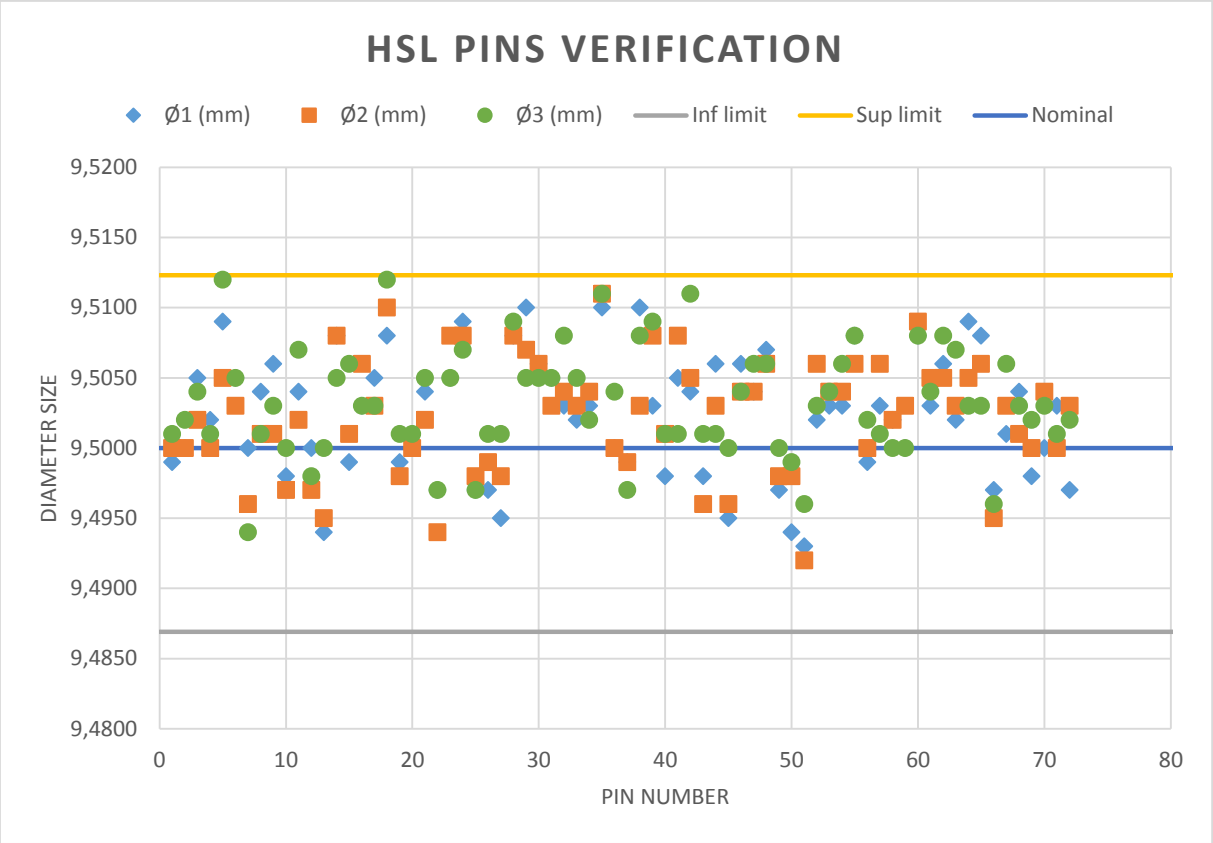

Figure 63 – HSL pins diameter. Source: author.

Moreover, with the data measured, it was possible to calculate the average interferences between pins and holes, based on the average values obtained from the measurements. The values were displayed in Table 8.

Table 8 – Average values and interference

Pins HST Ø (mm)	Pins HSL Ø (mm)	Holes HST Ø (mm)	Holes HSL Ø (mm)	Interference HST (mm)	Interference HSL (mm)
9,5010	9,5000	9,4765	9,4450	0,0245	0,0550
9,4943	9,5007	9,4755	9,4445	0,0188	0,0562
9,5037	9,5037	9,4765	9,4460	0,0272	0,0577
9,4947	9,5010	9,4755	9,4430	0,0192	0,0580
9,5017	9,5087	9,4760	9,4565	0,0257	0,0522
9,5013	9,5043	9,4765	9,4600	0,0248	0,0443
9,5003	9,4967	9,4765	9,4410	0,0238	0,0557
9,5050	9,5020	9,4765	9,4520	0,0285	0,0500
9,5067	9,5033	9,4870	9,4450	0,0197	0,0583
9,4977	9,4983	9,4865	9,4445	0,0112	0,0538
9,5020	9,5043	9,4865	9,4445	0,0155	0,0598
9,5000	9,4983	9,4855	9,4450	0,0145	0,0533
9,5083	9,4963	9,4725	9,4435	0,0358	0,0528
9,5067	9,5070	9,4760	9,4465	0,0307	0,0605

Pins HST Ø (mm)	Pins HSL Ø (mm)	Holes HST Ø (mm)	Holes HSL Ø (mm)	Interference HST (mm)	Interference HSL (mm)
9,4977	9,5020	9,4760	9,4460	0,0217	0,0560
9,5007	9,5040	9,4740	9,4570	0,0267	0,0470
9,4993	9,5037	9,4735	9,4610	0,0258	0,0427
9,4967	9,5100	9,4760	9,4530	0,0207	0,0570
9,5013	9,4993	9,4750	9,4485	0,0263	0,0508
9,4970	9,5007	9,4760	9,4625	0,0210	0,0382
9,5040	9,5037	9,4760	9,4635	0,0280	0,0402
9,4990	9,4960	9,4735	9,4615	0,0255	0,0345
9,5003	9,5060	9,4735	9,4650	0,0268	0,0410
9,4970	9,5080	9,4735	9,4595	0,0235	0,0485
9,4957	9,4973	9,4755	9,4415	0,0202	0,0558
9,5047	9,4990	9,4765	9,4445	0,0282	0,0545
9,5030	9,4980	9,4825	9,4405	0,0205	0,0575
9,4900	9,5083	9,4770	9,4435	0,0130	0,0648
9,5030	9,5073	9,4750	9,4460	0,0280	0,0613
9,4960	9,5057	9,4740	9,4435	0,0220	0,0622
9,5050	9,5043	9,4740	9,4445	0,0310	0,0598
9,4967	9,5050	9,4750	9,4445	0,0217	0,0605
9,5030	9,5033	9,4760	9,4455	0,0270	0,0578
9,4997	9,5030	9,4760	9,4455	0,0237	0,0575
9,5010	9,5107	9,4760	9,4450	0,0250	0,0657
9,4917	9,5013	9,4750	9,4455	0,0167	0,0558
9,4993	9,4983	9,4760	9,4450	0,0233	0,0533
9,4923	9,5070	9,4760	9,4440	0,0163	0,0630
9,5007	9,5067	9,4760	9,4465	0,0247	0,0602
9,4980	9,5000	9,4750	9,4445	0,0230	0,0555
9,5033	9,5047	9,4805	9,4470	0,0228	0,0577
9,4997	9,5067	9,4750	9,4440	0,0247	0,0627
9,4977	9,4983	9,4760	9,4445	0,0217	0,0538
9,5017	9,5033	9,4810	9,4480	0,0207	0,0553
9,5037	9,4970	9,4755	9,4430	0,0282	0,0540
9,5050	9,5047	9,4755	9,4445	0,0295	0,0602
9,5023	9,5047	9,4745	9,4595	0,0278	0,0452
9,5067	9,5063	9,4760	9,4535	0,0307	0,0528
9,5047	9,4983	9,4760	9,4480	0,0287	0,0503
9,5027	9,4970	9,4740	9,4590	0,0287	0,0380
9,4990	9,4937	9,4820	9,4485	0,0170	0,0452
9,4987	9,5037	9,4740	9,4475	0,0247	0,0562
9,5033	9,5037	9,4740	9,4470	0,0293	0,0567
9,4947	9,5043	9,4750	9,4460	0,0197	0,0583
9,4923	9,5073	9,4750	9,4475	0,0173	0,0598
9,4960	9,5003	9,4770	9,4475	0,0190	0,0528
9,5007	9,5033	9,4870	9,4430	0,0137	0,0603

Pins HST Ø (mm)	Pins HSL Ø (mm)	Holes HST Ø (mm)	Holes HSL Ø (mm)	Interference HST (mm)	Interference HSL (mm)
9,5017	9,5013	9,4855	9,4410	0,0162	0,0603
9,4970	9,5010	9,4850	9,4420	0,0120	0,0590
9,4997	9,5083	9,4860	9,4420	0,0137	0,0663
9,4993	9,5040	9,4870	9,4440	0,0123	0,0600
9,5033	9,5063	9,4870	9,4445	0,0163	0,0618
9,5017	9,5040	9,4870	9,4435	0,0147	0,0605
9,5063	9,5057	9,4870	9,4435	0,0193	0,0622
9,5003	9,5057	9,4860	9,4430	0,0143	0,0627
9,4990	9,4960	9,4855	9,4440	0,0135	0,0520
9,5013	9,5033	9,4855	9,4425	0,0158	0,0608
9,5020	9,5027	9,4860	9,4435	0,0160	0,0592
9,5033	9,5000	9,4870	9,4440	0,0163	0,0560
9,4933	9,5023	9,4870	9,4430	0,0063	0,0593
9,4990	9,5013	9,4845	9,4435	0,0145	0,0578
9,5013	9,5007	9,4840	9,4440	0,0173	0,0567

The average diameters for pins and holes, and the average interference obtained by those average values, were plotted in Figures 64, 65 and 66.

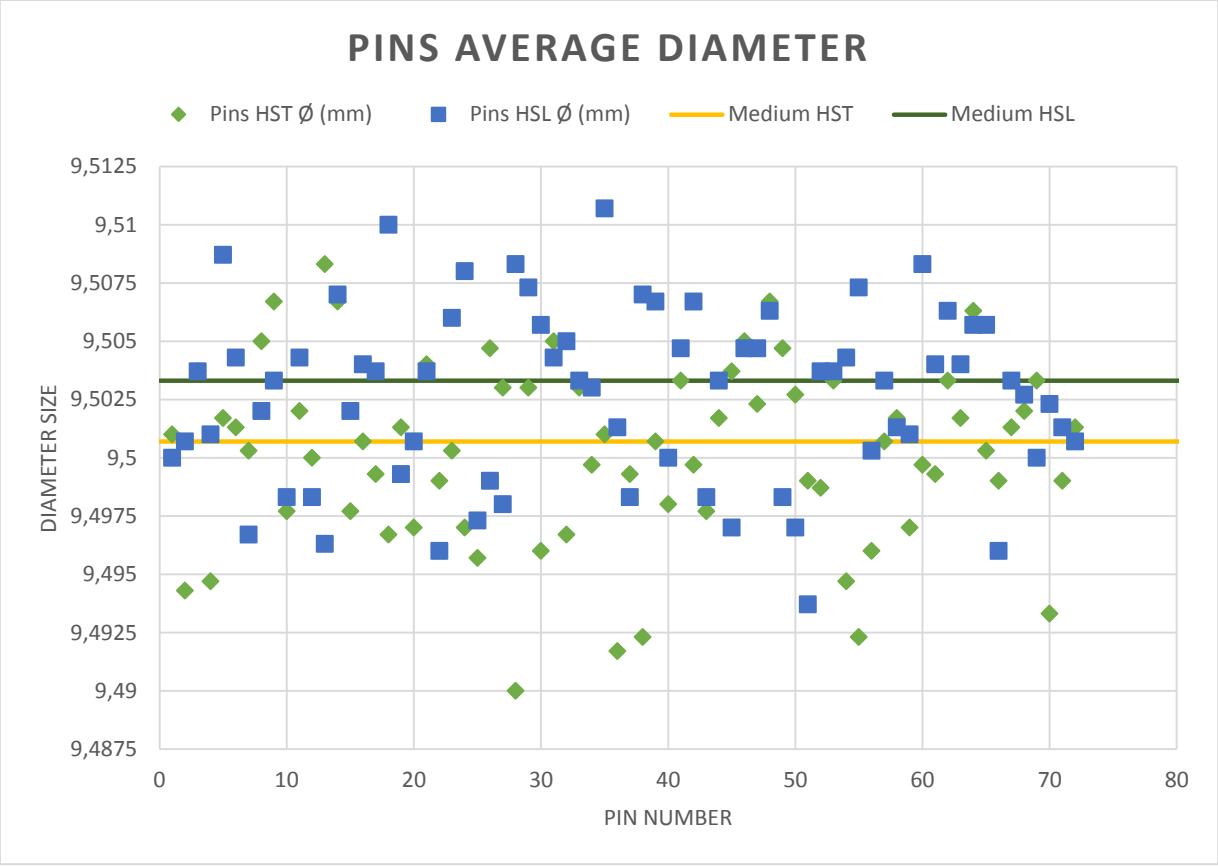

Figure 64 – Pins average diameter. Source: author.

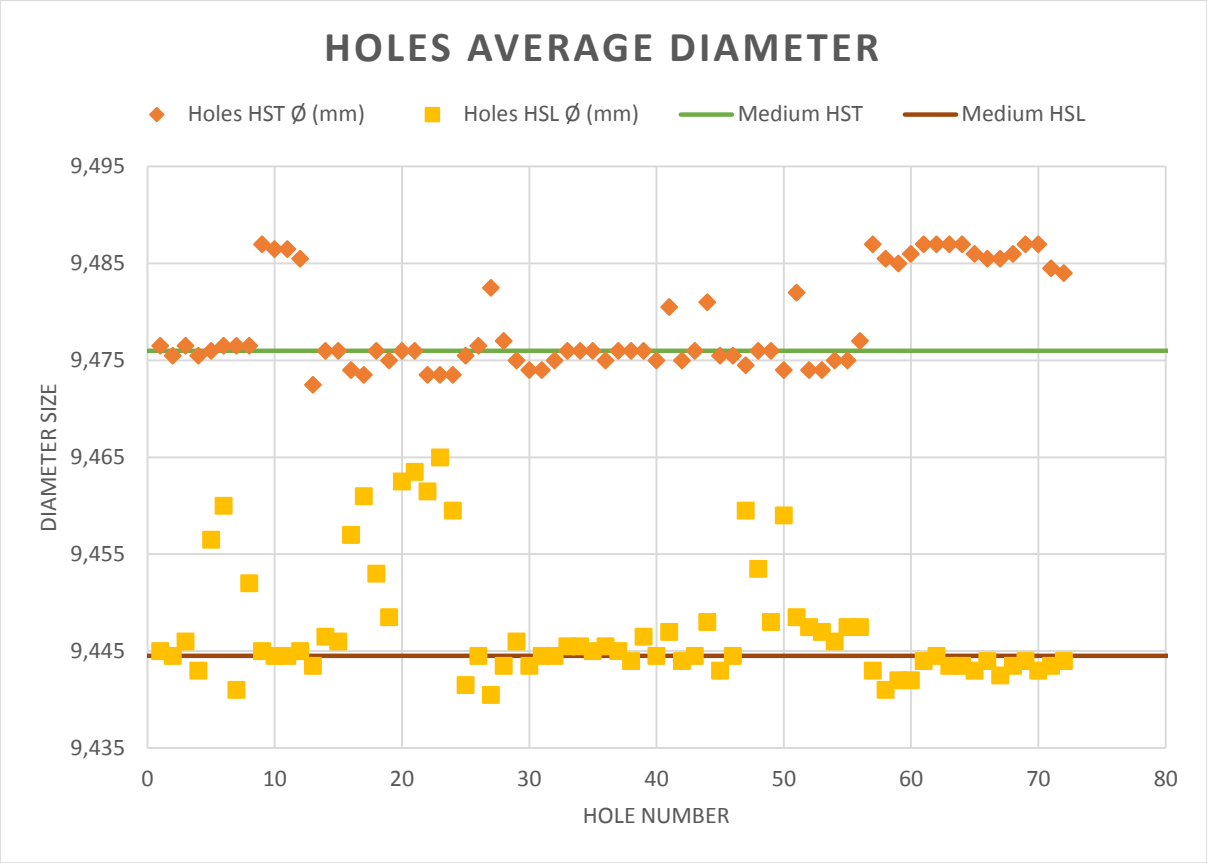

Figure 65 – Holes average diameter. Source: author.

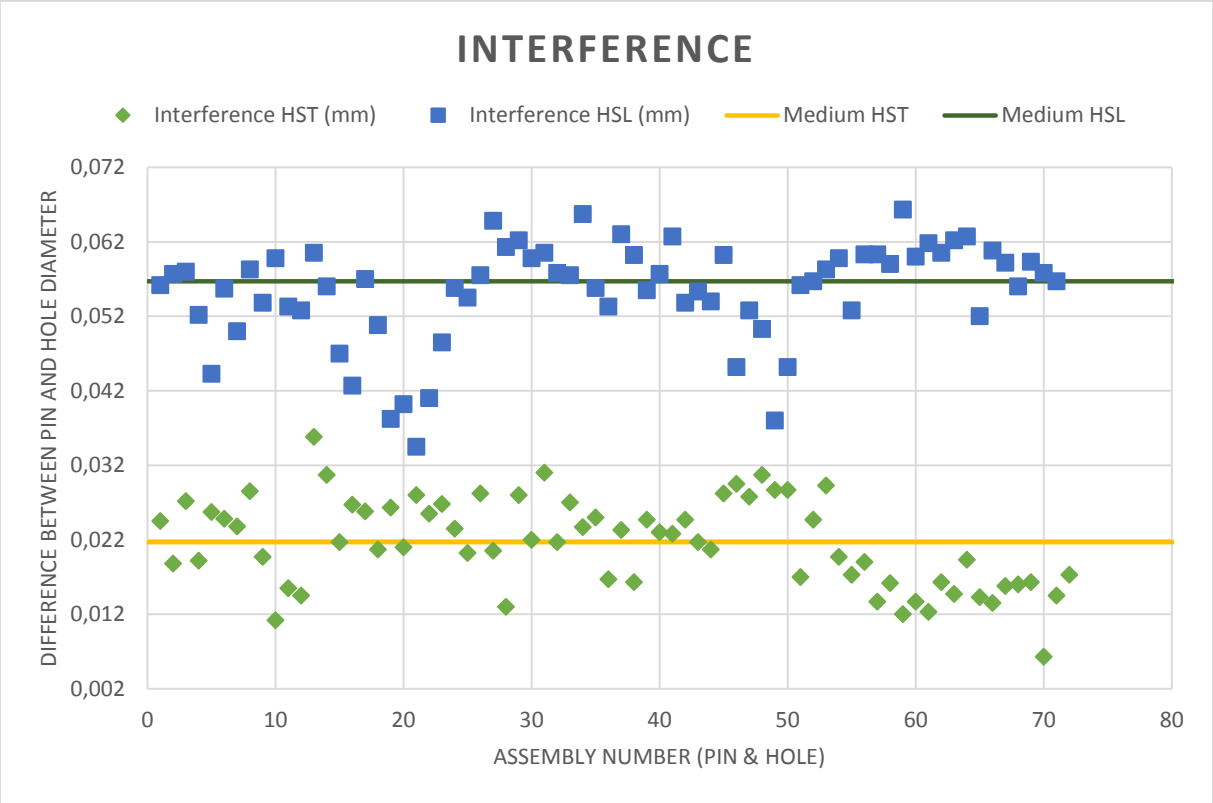

Figure 66 – Interference between pins and holes. Source: author.

Afterwards, it was necessary to prepare the specimen surface to receive the sealant. It was cleaned up using a sponge, after the scuffing. The sealant used was Naftoseal MC-780 C-12, applied respecting the time limit to execute the riveting process, which corresponds to 12 hours after application. It is important to notice that the sealant is used to promote the adhesion between the plates interface, also to assure a wet assembly for the pins.

For the drilling process performed on the specimens with HST pins, a rivet gun was applied, since the pins are already manufactured in its final form, needing just a pulling force, similar to a hit on its head. Then, they receive the nut on the other extremity, and the final torque is applied on the nut, corresponding to the EMBRAER requirements, from 200lbf.pol to 250lbf.pol.

Finally, using a pulling machine, the specimens containing HSL pins were inserted through a process that requires only the machine operation, once it is necessary a huge force to do the riveting process. Then, the nuts were also placed on the pins, in a similar process to the HSL ones. To end up the process, they also received final torque, following the same instructions and values for the HST pins.

The models done for both processes are illustrated in Figure 67.

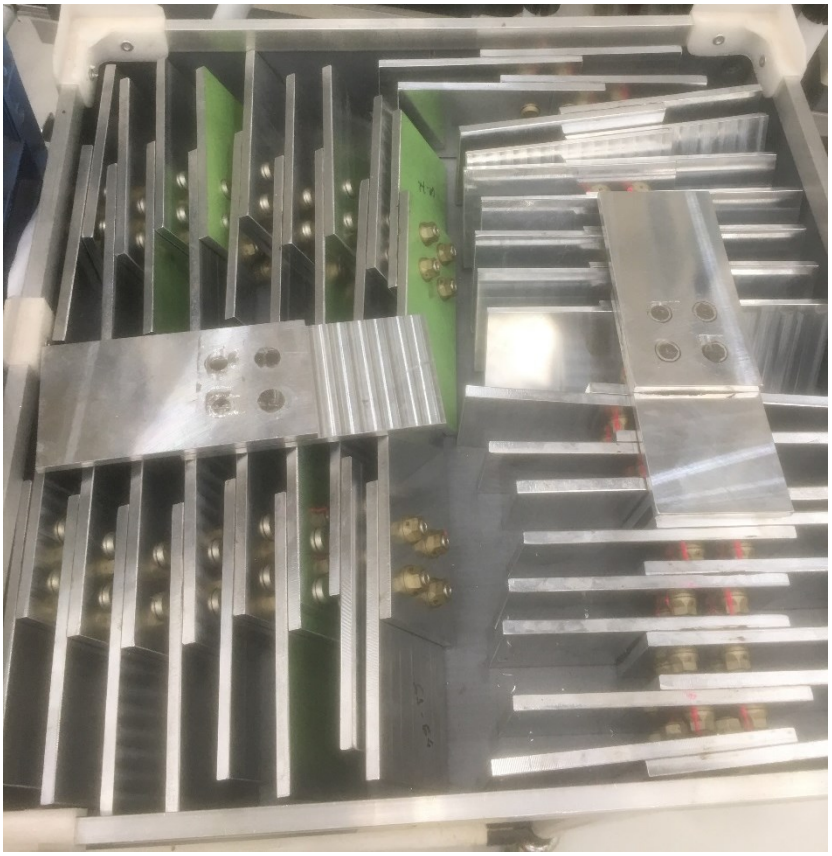

Figure 67 – Specimens after conclusion. Source: author.

For study and comparison, two specimens, one containing HST pins and one containing HLS pins, had the head of the pins removed by a machining process. This aimed to achieve a reading through specific machinery and software CATIA® of the real residual tension existent on the drilled holes. The analysis was made on Federal University of Uberlandia, in the Materials Laboratory, and the process is explained further on this work.

5.2 Tensile test machine

The first part of the experiments after software simulation was the specimens cycling. Table 9 brings the materials applied during this step.

Table 9 – List of equipment

Equipment	Manufacturer	Model
Aluminum plates	UFU	Single plate
Sandpaper	Klingspor	PS 8 A
Tensile Test Machine	MTS	647 Hydraulic Wedge Grip

5.3 Measurements procedure

As this work consists of experimental analysis, it was important to repeat the experiments in order to validate the results. The specimen configurations were tested for the two different diameters, including the different manufacturing process for cold working application. Hence, for each one, 16 models were tested, for the number of cycles and loading calculated.

Prior to each test, the model was fixed on the tensile test machine through a sandwich assembly, using one aluminum plate for each side and a piece of sandpaper between the specimen and the aluminum plate to guarantee the machine would correctly fix the specimen and avoid sliding. Figure 68 shows the assembly.

Figure 68 – Sandwich assembly on MTS machine. Source: author.

The next step was to adjust the pressure used to keep the specimen still during the test. It was set to 2300Psi, and then the first specimen, an HSL type, was tested for load, to assure a rupture close to the values calculated in section 4. Amplitude was calculated as 15kN, corresponding to half of the maximum force, in order to set the machine. It is important to notice that the first approach was to assume a 30kN load, equal to the simulated, aiming for a greater number of cycles.

Moreover, without an offset, the target was also calculated as 15kN, and the frequency applied was 30Hz, following the range of 10^{-2} to 10^{2} recommend by ASTM E466, 2018, due to the lack of interference on fatigue strength for most metallic material in this regime. Finally, the tests were restricted to 200,000 cycles and a maximum displacement of 10mm.

First test showed that the machine reduces the real force applied, as shown in Figure 69. This way, 200,000 cycles were needed to an equivalent force of approximately 26kN.

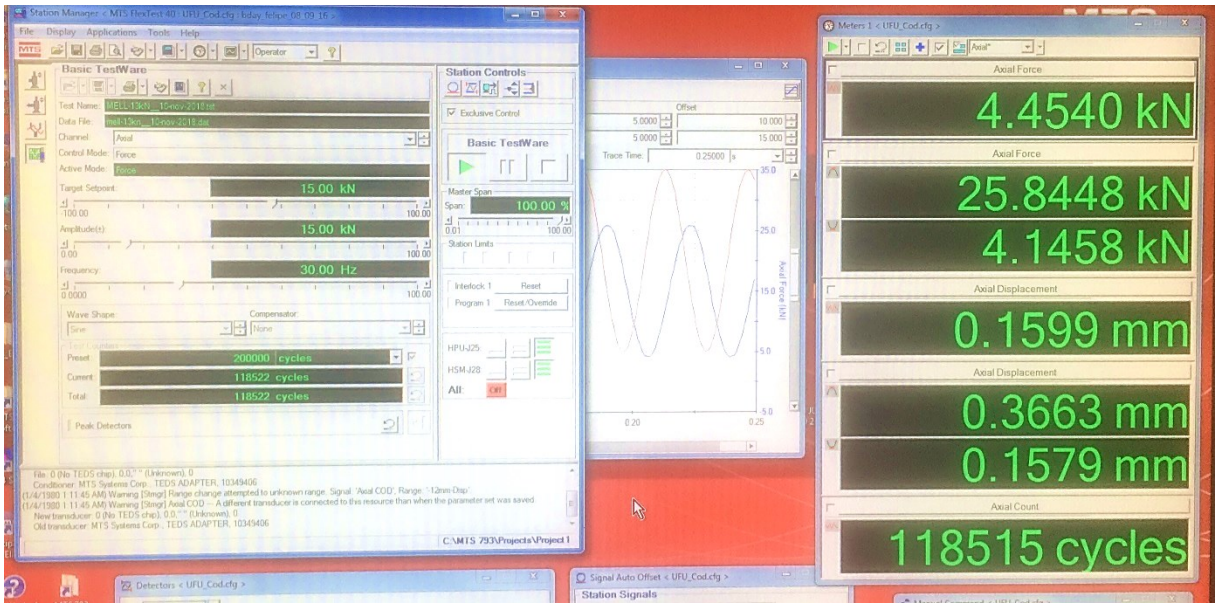

Figure 69 – Data input to MTS and respectively output. Source: author.

After that, the load was adjusted again to new values of 35kN, 40kN, 45kN, and 50kN, looking for 100,000 cycles breaking. While applying the input value machine of 50kN, after all the cycles the specimen was put through, the fracture happened on cycle number 29,797.

The second test was done for an HST specimen, using the adjusted load of 50kN, and it fractured after 58,461 cycles. As expected, this was the load picked for next tests, because of the ruptures happening before the planned 100,000 cycles.

5.4 Data reduction

The data acquired for the HSL and HST specimens within a 5.0 $tons$ or 50kN load applied were respectively displayed in Tables 10 and 11 and plotted in Figure 70.

Table 10 – Cycles until rupture for HSL specimens

Specimens with HSL pins	
Specimen number	Number of cycles until rupture
1	62316
2	73537
3	77639
4	66419
5	85823
6	45864
7	50332
8	68368
9	61955
10	59112
11	104790
12	54428
13	39176
14	65567
15	97080
16	57722

Table 11 – Cycles until rupture for HST specimens

Specimens with HST pins	
Specimen number	Number of cycles until rupture
1	34394
2	43060
3	55805
4	58469
5	34502
6	57287
7	47850
8	39119
9	43997
10	42491
11	78982
12	45961
13	38435
14	34853
15	57381
16	43824

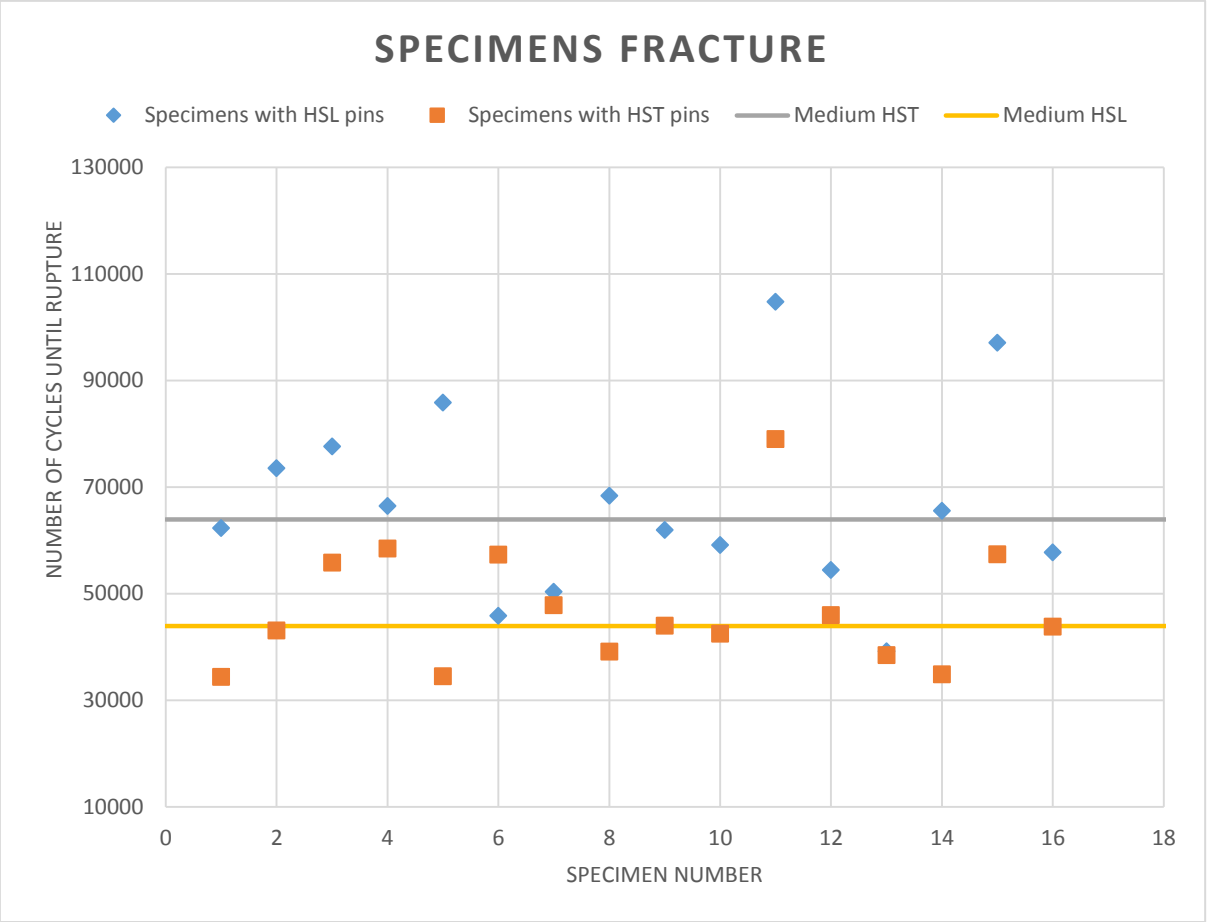

Figure 70 – Specimens fracture data. Source: author.

6 EXPERIMENTAL RESULTS AND ANALYSIS

6.1 Correction effects

Specimens were simulated and tested with bending effect, which was not predicted by the calculation in literature. This effect can contribute to accelerate the fatigue life and propagation crack.

There was an observed difference between the input load and the effective load applied, due to the machine procedure adopted in order to quickly reduce the load applied and then start applying it again. This way, the effective load for all the specimens corresponded to an average value of 4.6 $tons$. Also, the frequency adjusted during tests could have had interference on the machinery load, which can indeed contribute to a non-linear result during the tests.

Moreover, the sealant effect, as explained in section 5.1.4., was neither computed during simulation nor during literature calculation, which can lead to a significant difference between the expected load and the real load supported by the specimens.

Finally, there could be a minor misalignment effect associated to the sandwich assembly, causing eccentricity to the force applied.

Other source of errors that could lead to variation between the values expected and achieved could be associated to the specimen manufacturing and verification, due to measurement reading error. Furthermore, the variation between specimens assembly, i.e. different interference levels for same specimen type, could have yielded to the non-linear result accomplished. Lastly, the computations made regards the fatigue cycling could have its own error, due to software acquisition and reading.

6.2 Simulation comparison

The results obtained during simulation through CATIA® finite element model presented a close result to the calculated. Despite the absolute error of 2.5kN, which leads to a relative error of 83N, the approximated $\boldsymbol{K_T}$ had a relative error of 0.4%, which suggests a great representation of the model.

The average values for HST and HSL, or 63,942, and 43,911 cycles to rupture with a 46kN real load, respectively, were compared and extrapolated out of a linear function from the result obtained through software for 100,000 cycles, with a 30kN load. It was possible to see an average of 65,217 cycles for the condition proposed, which leads to 1.99% relative error for

HSL and 32.67% for HST. However, the curves used neither predict a single-shear joint, nor an accurate result by linear approximation, since they are an exponential function. For comparison, considering a linear function, it is possible to notice a reduction on the cycles for HSL, compared to the ideal curve. It can be easily explained by the bending effect previously mentioned.

6.3 Literature comparison

It was possible to see that the failure mode during tests corresponded to the tearing of the plate when it is under tension, mentioned on topic 2.1.5. This represents a failure due to fatigue, since the other failure modes – failure of a rivet by shearing or crushing, and failure by tearing of the plate at the edge –, happen usually due to static loads, which could have happened in a low cycle number during tests, and does not apply in the present experiment. Figure 71 shows an HSL specimen after the rupture, and Figure 72 focuses on the hole area after rupture, which shows the beach marks and the crack advancements, beginning on the plates interface area, as expected from simulations.

Figure 71 – HSL1 after rupture. Source: author.

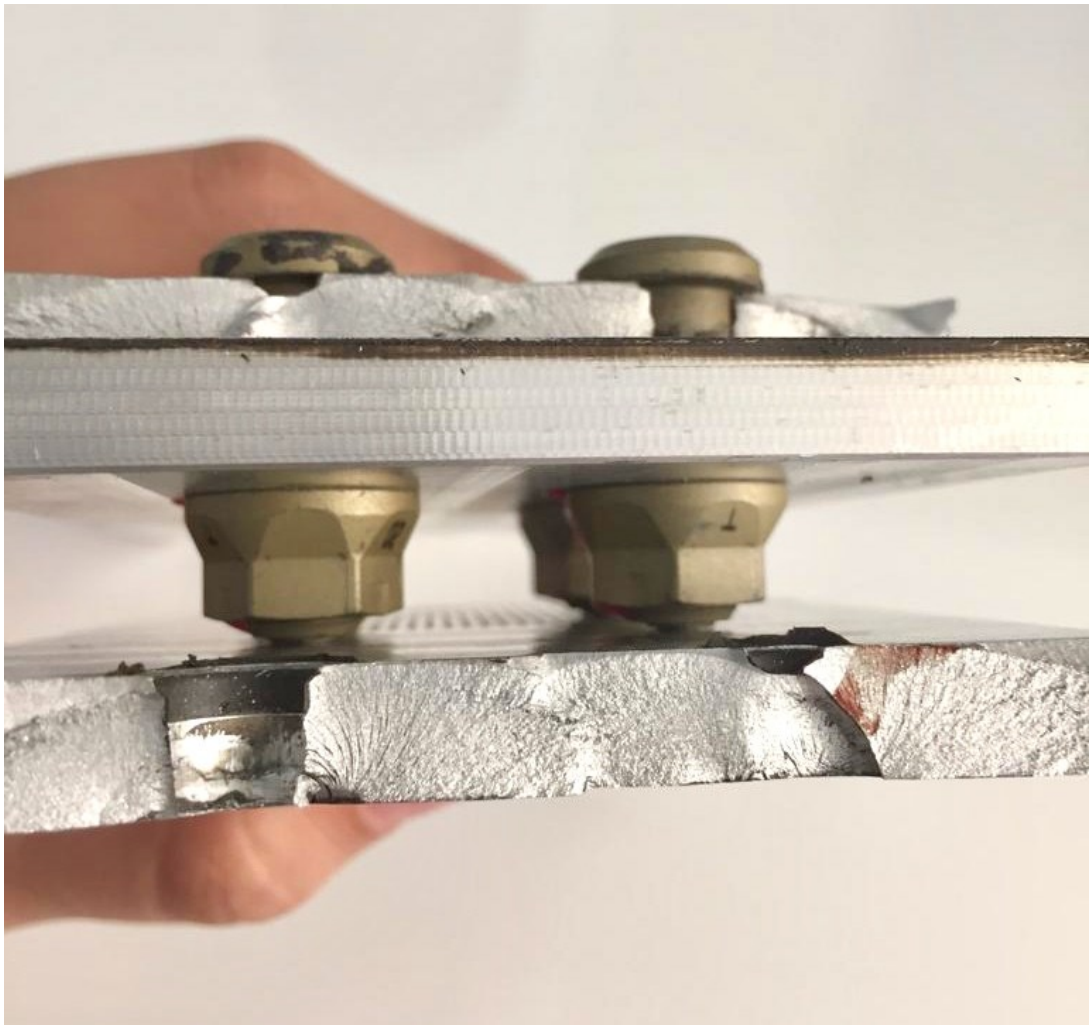

Figure 72 – HSL1 detail after rupture. Source: author.

Moreover, for a case of MWD, the multiple fatigue accelerates the crack propagation that happens perpendicular to the load applied on the joint, going from one hole to another, similar to the Aloha Airlines case mentioned in section 3.2.

Finally, the values calculated for failure for HSL type had a average value of 63,942 cycles, with a standard deviation of 17,701 cycles; while for HST type, 43,911 cycles until rupture, with a standard deviation of 11,830 cycles. Comparing both values, it is possible to notice a 45% improvement on fatigue life with the cold work use. Analyzing the values obtained on topic 2.5, it showed a minor improvement than the expected for a 7050 enriched aluminum alloy. However, the studies demonstrated that the improvement varies within the load applied, which could be the responsible for such reduction. Also, those studies were not done with a single shear joint, considering different conditions applied on the tests, not including bending effects.

7 CONCLUSIONS

7.1 General Remarks

Cold work presented significant improvements when compared to the lack of any procedure to enhance residual stress around a hole, withstanding 45% more in fatigue life for HSL in comparison to HST specimens. Values were minor than supposed by previous experiments due to different conditions applied in the tests, which included bending, error in machinery software reading and minor misalignments during specimens fatigue cycling.

The extrapolated values for 100,000 cycles and a 30kN simulated value, within relative errors of 1.99% and 32.67% for HSL and HST specimen types, respectively, can be explained by the exponential curve for $\boldsymbol{K_T}$ which neither predict accurate correlations for calculated $\boldsymbol{K_T} = \mathbf{5.01}$, nor a proper result for single shear joints. Moreover, none of the expectations considered the bending effect that naturally reduces fatigue life of the component. Considering the reduced fatigue life that should be seen, HSL behavior had result closer to the expected in comparison to HST specimens, proving that the gain in residual stress guarantees more fatigue life to the component.

Prediction of load for crack on the specimens was made by two different methods that yielded into a meticulous result, within relative errors of 83N to the load and 0.4% to $\boldsymbol{K_T}$. Despite the discrepancy, the model properly simulated the specimen fail mode and higher stresses zone, with the propagation crack happening due to the tear of plate on the contact surface, a mode of failure characterized by fatigue load cycling.

Withal, the results were satisfactory for the application of new cold work method, since the improvement could indeed increase fatigue life of the joint used on a wing-to-wing assembly, the model was representative and all the assumptions for errors and effects were in accordance to the theory.

7.2 Future Work

A more accurate study should be done regarding the cost analysis and feasibility to implement the modifications needed do apply this method in the production process. Also, an analysis comparison aiming for the best stress level to the model could be made.

The maximum interference level between pins and holes could be studied in order to avoid compromising the component structural function and the insertion process. Moreover,

analysis of the component loads during aircraft cycles and simulation for this specific stress level would help yield more precise results.

Furthermore, looking for a real measurement of the residual stresses around the drilled holes, as shown in section 2.3.2, an X-ray diffraction method could be used to compare structural properties of each type of specimen. With the references for 7050 aluminum enriched alloy, reading point by point nearby the hole, it would be possible to analyze if the space between atoms was reduced, indicating compression, or increased, indicating stress.

Finally, aiming for a better comparative result to the traditional cold work method, a new experiment within the same conditions applied in this one should be done.

8 REFERENCES

AEROTIME NEWS HUB, **History Hour: Aloha Airlines Flight 243 incident,** 2017. Available at: <https://www.aerotime.aero/yulius.yoma/18542-history-hour-aloha-airlines-flight-243-incident> Accessed on July, 2018.

ASTM E466, **Standard Practice for Conducting for Controlled Constant Amplitude Axial Fatigue Tests of Metallic Materials**, 2018.

BACON, D., DIETER, G. E., **Mechanical Metallurgy** (SI Metric Edition), McGraw-Hill, London, 1988. Available at: <http://stu.westga.edu/~bthibau1/MEDT%207477-Cooper/Calibre%20Library/Dieter_%20George%20Ellwood/Mechanical%20metallurgy%20(13)/Mechanical%20metallurgy%20-%20Dieter_%20George%20Ellwood.pdf> Accessed on May, 2018.

BARTER, S., DIXON, B., **Investigation using quantitative fractography of an unexpected failure in an F/A-18 – centre fuselage bulkhead in the FINAL teardown program**. Eng Fail Anal 2009, 16(3):833-48.

CALLISTER, W. D. **Ciência e Engenharia de Materiais: Uma Introdução**. 5. Ed. Rio de Janeiro: TLC, 2002.
Available at: <https://www.ebah.com.br/content/ABAAAgseMAD/ciencia-engenharia-dos-materiais-callister-7-ed> Accessed on May, 2018.

CATIA®. **CATIA V5R20**. [S.I.]: Dassault Systèmes ®, 1999.

COPE, D.A., LACY, T.E., **Modeling Mechanical Fasteners in Lap Joints for Stress Intensity Determination**, 4th Joint DOD/FAA/NASA Conference on Aging Aircraft, May 2000.

EMBRAER, Embraer normative engineering, **NE03-006/2018 Rivets and pins – drilling, countersinking and dimpling**, 2018.

EMBRAER, **Embraer E190-E2 passa no teste de carga crítica**, 2017. Available at: <http://www.defesaaereanaval.com.br/embraer-e190-e2-passa-no-teste-de-carga-critica/> Accessed on June, 2018.

ENGINEERING INSTITUTE OF TECHNOLOGY (EIG), **Sixteen Engineering Blunders**, 2018. Available at: <https://www.eit.edu.au/cms/news/industry/sixteen-engineering-blunders> Accessed on July, 2018.

FEDERAL AVIATION ADMINISTRATION (FAA), **Aircraft Accident Report – Aloha Airlines, Flight 243, Boeing 737-200, N73711, near Maui, Hawaii, April 28, 1988**. Washington, D.C., 1989. Available at: <https://www.faa.gov/about/initiatives/maintenance_hf/library/documents/media/human_factors_maintenance/aircraft_accident_report--aloha_airlines.flight_243.boeing_737-200.n73711.near_maui.hawaii.april_28.1988.pdf> Accessed on July, 2018.

FEDERAL AVIATION ADMINISTRATION (FAA), **MMPDS04 Handbook – Metallic Materials Properties Development**, 2008.

FLIGHTGLOBAL, **Aviation History Archive**, 1951. Available at: <https://www.flightglobal.com/pdfarchive/view/1951/1951%20-%200587.html> Accessed on July, 2018.

HOGGARD, A. W., JOHNSON, S. R., **Understanding the New Widespread Fatigue Damage Rule**, 2012. Available at: <https://www.boeing.com/commercial/aeromagazine/articles/2012_q4/pdfs/AERO_2012q4_article2.pdf> Accessed on July, 2018.

HUANG, W., WANG, T., Garbatov, Y., SOARES, C. **Fatigue reliability assessment of riveted lap joint of aircraft structures**. International Journal of Fatigue, 2012. Available at: <https://kundoc.com/pdf-fatigue-reliability-assessment-of-riveted-lap-joint-of-aircraft-structures-.html> Accessed on June, 2018.

HUTH, H., **The Influence of fastener Flexibility on the Prediction of Load Transfer and Fatigue Life for Multi-Row Joints**, LBF-FhG, ASTM Conference, Charleston, South Carolina, 1985. Available at: <https://ntrl.ntis.gov/NTRL/dashboard/searchResults/titleDetail/N8516219.xhtml> Accessed on August, 2018.

IEEE, Global Spec, **Fastener Standards**, 2018. Available at: <https://www.globalspec.com/learnmore/manufacturing_process_equipment/industrial_assembly/riveters_automated_riveting_tools> Accessed on May, 2018.

FATIGUE TECHNOLOGY, **What is cold expansion**, 2018. Available at: <http://www.fatiguetech.com/about-cold-expansion.asp> Accessed on June, 2018.

KANG, J. D., JOHNSON, W. S., CLARCK, D. A., **Three-dimensional finite element analysis of the cold expansion of fastener holes in two aluminum alloys**, 2002.

KHODABAKSHI, A., **Effects of cold working and heat treatment on microstructure and wear behavior of Cu-Be alloy C17200**, 2015. Available at: <https://www.tandfonline.com/doi/full/10.1080/17515831.2015.1107257?scroll=top&needAccess=true&> Accessed on May, 2018.

LAZZARIN, P., TOVO, R., FILIPPI, S., **Elastic stress distributions in finite size plates with edge notches**. Int J Fract 91:269–282, 1998.

LISI Aerospace, **Hi-lite pins**, 2018. Available at: <http://www.lisi-aerospace.com/products/fasteners/externally-threaded/pin/pages/hi-lite.aspx> Accessed on June, 2018.

LISI Aerospace, **Pull-in pins**, 2018. Available at: <http://www.lisi-aerospace.com/products/fasteners/externally-threaded/pin/Pages/pull-in.aspx> Accessed on June, 2018.

LISI Aerospace, **Installation Specification,** 2018. Available at:

<http://www.lisi-aerospace.com/_layouts/CentralDocConnector/DCConnector.aspx?id=1&listId=Documentation&downloaded=HSTR_HLR-IS01&type=Standard> Accessed on September, 2018.

MAKAR, J. M., TANNER, B. K., **Journal of Magnetism and Magnetic Materials**. 2000. Available at: <https://www.sciencedirect.com/science/article/pii/S0304885300005588> accessed on February, 2018.

SEDLACEK, G., MÜLLER, C., **The use of very high strength steels in metallic construction.** Proceedings of 1st International Conference Super-high Strength Steels, 2005.

NIU, M. C. Y., **Airframe Stress Analysis and Sizing**. California, 1999. - Available at: <https://soaneemrana.org/onewebmedia/AIRFRAME%20STRESS%20ANALYSIS%20AND%20SIZING%20BY%20MICHAEL%20C.Y.%20NIU.pdf> Accessed on January, 2018.

NIU, M. C. Y., **Airframe Structural Design.** California, 1995. Available at: < https://aeroknowledge77.files.wordpress.com/2011/09/62595839-structures-airframe-structural-design.pdf> Accessed on January, 2018.

NATIONAL PROGRAMME ON TECHNOLOGY ENHANCED LEARNING (NPTEL), **Design of permanent joints**, 2018.
Available at: <https://nptel.ac.in/courses/112105125/pdf/mod10les2.pdf> Accessed on April, 2018.

PAPANIKOS, P., MEGUID, S. A., STEPANOVIC, S., **Three dimensional nonlinear finite element analysis of dovetail joints in aeroengine discs**, 1998.

PINTO, D. **Estudo do efeito da classe de furação na resistência à fadiga em junta alumínio – fibra de carbono**. Guaratinguetá, 2011. Available at: <https://repositorio.unesp.br/bitstream/handle/11449/120594/pinto_dj_tcc_guara.pdf?sequence=1> Accessed on October, 2017.

RADAJ, D., VORMWALD, M., **Advanced Methods of Fatigue Assessment**, DOI: 10.1007/978-3-642-30740-9_2, Springer-Verlag Berlin Heidelberg, 2013.

RIJCK, J.J.M., FAWAZ, S.A., **Stress Analysis of Mechanically Fastened Joint and Stress Intensity Solutions for Countersunk Holes Under General Loading**, ICAF 2003, pp.455-476, 2004.

RIJCK, J.J.M., FAWAZ, S.A., **Stress Intensity Solutions for Countersunk Holes Subjected to Tension, Bending and Pin Loading**, 6th Joint DOD/FAA/NASA Conference on Aging Aircraft, 2002.

ROYLANCE, D., **Stress-Strain Curves.** Cambridge, MA, 2001. Available at: <http://web.mit.edu/course/3/3.11/www/modules/ss.pdf> Accessed on May, 2018.

SCHIJVE, J., **Some Elementary Calculations on Secondary Bending in Simple Lap Joints**, NLR TR 72036, National Aerospace Laboratory, Amsterdam, NL, 1972.

SEELIO, **Case Study on Aloha Airlines Flight 243 Accident**, 2016. Available at: <https://seelio.com/w/20bu/case-study-on-aloha-airline-flight-243-accident> Accessed on: July, 2018.

SKORUPA, A., SKORUPA, M., MACHNIEWICZ, T., KORBEL, A., **Fatigue crack location and fatigue life for riveted lap joints in aircraft fuselage**. Int J Fatigue; 58:209‑17, 2014.

SWIFT, T., **Development of Fail-Safe Design Features of the DC-10**, ASTM, STP 486, pp.164-214, 1091.

SZOLWINSKI, M. P., FERRIS, T. N., **Fretting fatigue Crack Initiation: Aging Aircraft Concerns**, 35th AIAA/ASME/ASCE/AHS/ASC Structures, Structural Dynamics, and Materials Conference - Part 4, Hilton Head, NC, AIAA, 1994.

TATE, M.B., ROSENFELD, S.J., **Preliminary Investigation on Loads Carried by Individual Joints, NACA-TN-1051**, Washington, 1946.

TEC EUROLAB, **Stages of Fatigue Failure**, 2018. Available at: <https://www.tec-eurolab.com/eu-en/stages-of-fatigue-failure.aspx> Accessed on September, 2018.

VENTURINI, S. N. **Estudo de junções aeronáuticas híbridas (metal-compósito) unidas mecanicamente**. 2010. 177p. Dissertação (Mestrado) – Escola de Engenharia de São Carlos, Universidade de São Paulo, São Paulo, 2010.
Available at: <http://www.teses.usp.br/teses/disponiveis/18/18148/tde-30072010-105737/publico/VENTURINI.pdf> Accessed on October, 2017.

WRONICZ, W., KANIOWSKI, J. **The analysis of the influence of riveting parameters specified in selected riveting instructions on residual stresses**. Institute of Aviation, Warsaw, Poland, 2014. Available at: <Wronicz_The-analysis_6_2014.pdf> Accessed on, January, 2018.

WYTHERS, M. C., **Joining of GFRP in marine applications**, 2012. Available at: <https://www.researchgate.net/publication/259480752_Joining_of_GFRP_in_Marine_Applications> Accessed on January, 2018.

XAVIER, Antônio Carlos de Barros. **Considerações Para Análise de Juntas**. 2006. 150 f. Tese (Mestrado) - Instituto Tecnlógico de Aeronáutica, São José Dos Campos, 2006. Available at: <http://www.bdita.bibl.ita.br/tesesdigitais/000542937.pdf> accessed on November, 2017.

YUCAN, F., ENDE, G., HONGHUA, S., JIUHUA, X., RENZHENG, L. **Cold expansion technology of connection holes in aircraft structures: A review and prospect**. Chinese Journal of Aeronautics, 2015. Available at: <https://www.researchgate.net/publication/279314307_Cold_expansion_technology_of_connection_holes_in_aircraft_structures_A_review_and_prospect/fulltext/5593457408ae1e9cb4299362/279314307_Cold_expansion_technology_of_connection_holes_in_aircraft_structures_A_review_and_prospect.pdf> Accessed on January, 2018.

9 APPENDIX A – HSL1416 DATASHEET

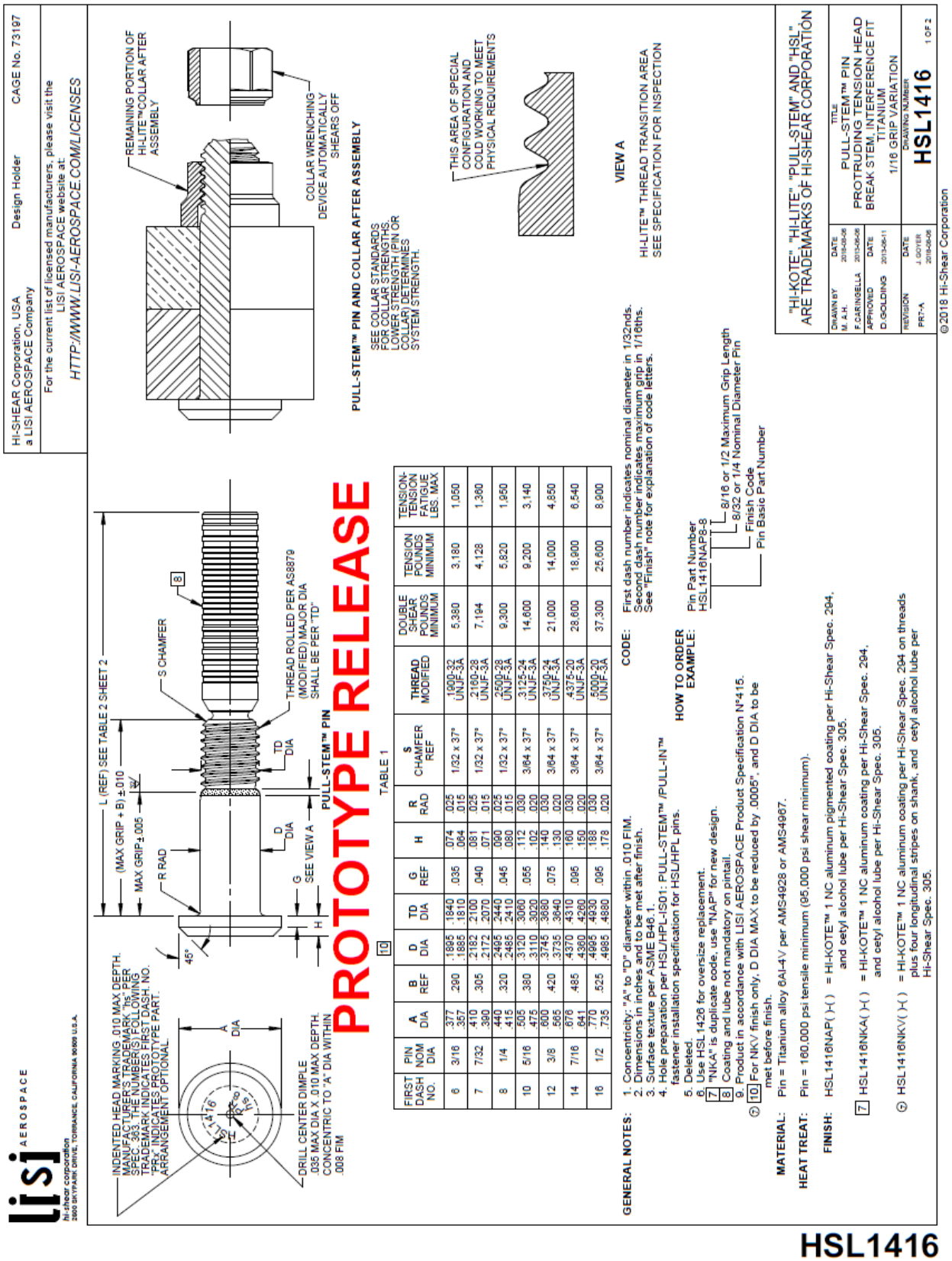

HSL1416

lisi AEROSPACE
hi-shear corporation
2600 SKYPARK DRIVE, TORRANCE, CALIFORNIA 90509 U.S.A.

TABLE 2

SECOND DASH NUMBER	L REF						
	-6 DIA.	-7 DIA.	-8 DIA.	-10 DIA.	-12 DIA.	-14 DIA.	-16 DIA.
1	-	-	-	-	-	-	-
2	1.000	1.000	1.000	-	-	-	-
3	1.125	1.125	1.125	1.250	-	-	-
4	1.250	1.250	1.250	1.375	1.375	-	-
5	1.375	1.375	1.375	1.500	1.500	1.625	-
6	1.500	1.500	1.500	1.625	1.625	1.750	1.750
7	1.625	1.625	1.625	1.750	1.750	1.875	1.875
8	1.750	1.750	1.750	1.875	1.875	2.000	2.000
9	1.875	1.875	1.875	2.000	2.000	2.125	2.125
10	2.000	2.000	2.000	2.125	2.125	2.250	2.250
11	2.125	2.125	2.125	2.250	2.250	2.375	2.375
12	2.250	2.250	2.250	2.375	2.375	2.500	2.500
13	2.375	2.375	2.375	2.500	2.500	2.625	2.625
14	2.500	2.500	2.500	2.625	2.625	2.750	2.750
15	2.625	2.625	2.625	2.750	2.750	2.875	2.875
16	2.750	2.750	2.750	2.875	2.875	3.000	3.000
17	2.875	2.875	2.875	3.000	3.000	3.125	3.125
18	3.000	3.000	3.000	3.125	3.125	3.250	3.250
19	3.125	3.125	3.125	3.250	3.250	3.375	3.375
20	3.250	3.250	3.250	3.375	3.375	3.500	3.500
21	3.375	3.375	3.375	3.500	3.500	3.625	3.625
22	3.500	3.500	3.500	3.625	3.625	3.750	3.750
23	3.625	3.625	3.625	3.750	3.750	3.875	3.875
24	3.750	3.750	3.750	3.875	3.875	4.000	4.000
25	-	-	-	4.000	4.000	4.125	4.125
26	-	-	-	4.125	4.125	4.250	4.250
27	-	-	-	4.250	4.250	4.375	4.375
28	-	-	-	4.375	4.375	4.500	4.500
29	-	-	-	-	4.500	4.625	4.625
30	-	-	-	-	4.625	4.750	4.750
31	-	-	-	-	4.750	4.875	4.875
32	-	-	-	-	4.875	5.000	5.000
33	-	-	-	-	5.000	5.125	5.125
34	-	-	-	-	5.125	5.250	5.250
35	-	-	-	-	5.250	5.375	5.375
36	-	-	-	-	5.375	5.500	5.500
37	-	-	-	-	5.500	5.625	5.625
38	-	-	-	-	5.625	5.750	5.750
39	-	-	-	-	5.750	5.875	5.875
40	-	-	-	-	5.875	6.000	6.000
41	-	-	-	-	6.000	6.125	6.125
42	-	-	-	-	6.125	6.250	6.250
43	-	-	-	-	6.250	6.375	6.375
44	-	-	-	-	6.375	6.500	6.500

10 APPENDIX B – HST12 DATASHEET

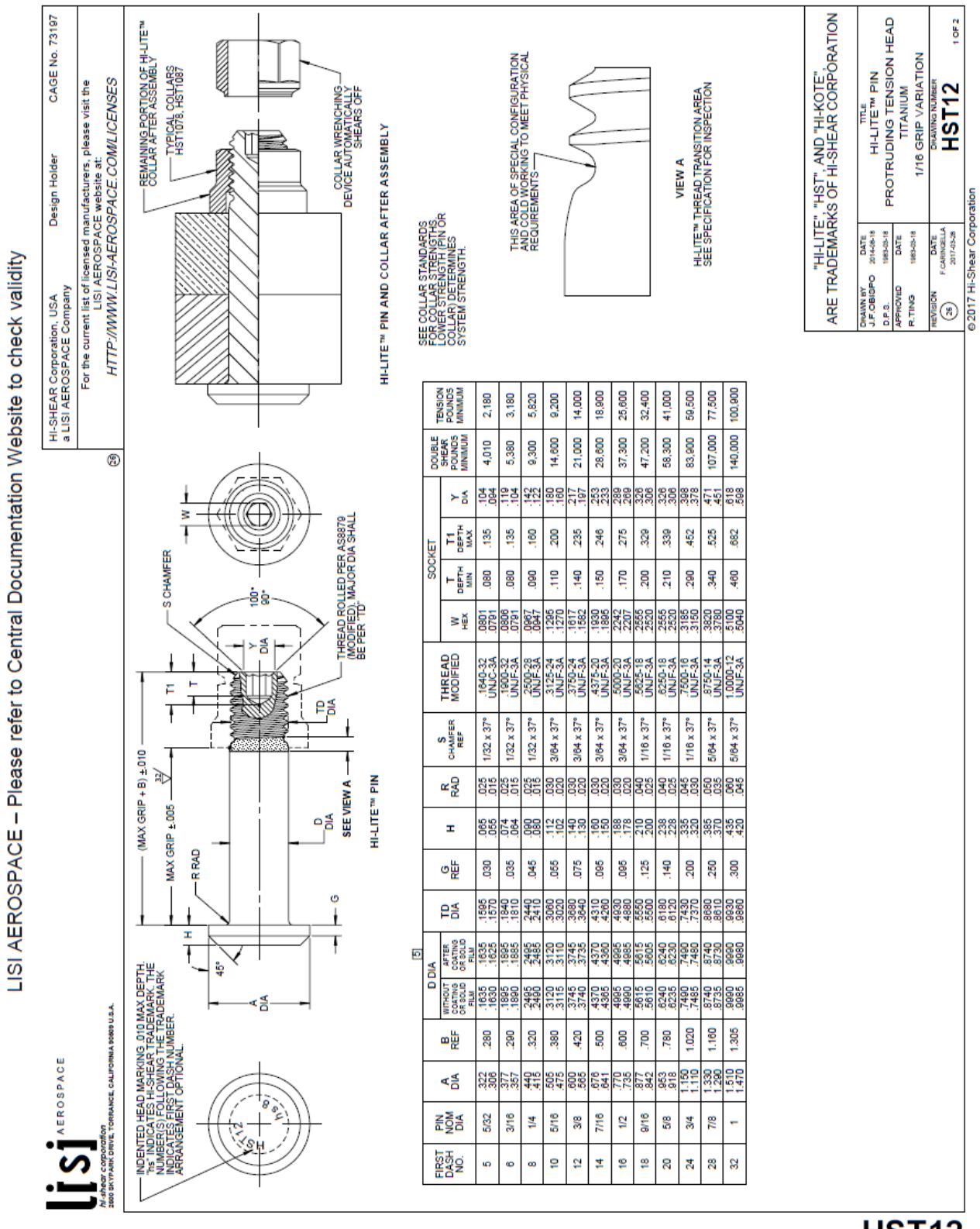

FIRST DASH NO.	PIN NOM DIA	A DIA	B REF	D DIA WITHOUT COATING OR SOLID FILM	D DIA AFTER COATING OR SOLID FILM	TD DIA	G REF	H	R RAD	S CHAMFER REF	THREAD MODIFIED	W HEX	T DEPTH MIN	T1 DEPTH MAX	Y DIA	DOUBLE SHEAR POUNDS MINIMUM	TENSION POUNDS MINIMUM
5	5/32	.322 .306	.280	.1635 .1630	.1635 .1625	.1595 .1570	.030	.065 .055	.025 .015	1/32 x 37°	.1640-32 UNJC-3A	.0801 .0791	.080	.135	.104 .094	4,010	2,180
6	3/16	.377 .357	.290	.1895 .1890	.1895 .1885	.1840 .1810	.035	.074 .064	.025 .015	1/32 x 37°	.1900-32 UNJF-3A	.0806 .0791	.080	.135	.119 .104	5,380	3,180
8	1/4	.440 .416	.320	.2495 .2490	.2495 .2485	.2440 .2410	.045	.090 .080	.025 .015	1/32 x 37°	.2500-28 UNJF-3A	.0967 .0947	.090	.160	.142 .122	9,300	5,820
10	5/16	.505 .475	.380	.3120 .3115	.3120 .3110	.3060 .3020	.055	.112 .102	.030 .020	3/64 x 37°	.3125-24 UNJF-3A	.1296 .1270	.110	.200	.180 .160	14,600	9,200
12	3/8	.600 .565	.420	.3745 .3740	.3745 .3735	.3680 .3640	.075	.140 .130	.030 .020	3/64 x 37°	.3750-24 UNJF-3A	.1617 .1582	.140	.235	.217 .197	21,000	14,000
14	7/16	.676 .641	.500	.4370 .4365	.4370 .4360	.4310 .4260	.095	.160 .150	.030 .020	3/64 x 37°	.4375-20 UNJF-3A	.1930 .1895	.150	.246	.253 .233	28,600	18,900
16	1/2	.770 .735	.600	.4995 .4990	.4995 .4985	.4930 .4880	.095	.188 .178	.030 .020	3/64 x 37°	.5000-20 UNJF-3A	.2242 .2207	.170	.275	.289 .269	37,300	25,600
18	9/16	.877 .842	.700	.5615 .5610	.5615 .5605	.5550 .5500	.125	.210 .200	.040 .025	1/16 x 37°	.5635-18 UNJF-3A	.2565 .2520	.200	.329	.326 .306	47,200	32,400
20	5/8	.963 .918	.780	.6240 .6230	.6240 .6230	.6180 .6120	.140	.238 .228	.040 .025	1/16 x 37°	.6250-18 UNJF-3A	.2565 .2520	.210	.339	.338 .308	58,300	41,000
24	3/4	1.150 1.110	1.020	.7490 .7485	.7490 .7480	.7430 .7370	.200	.335 .320	.045 .030	1/16 x 37°	.7500-16 UNJF-3A	.3185 .3150	.290	.452	.398 .378	83,600	59,500
28	7/8	1.330 1.280	1.160	.8740 .8735	.8740 .8730	.8680 .8610	.250	.386 .370	.050 .035	5/64 x 37°	.8750-14 UNJF-3A	.3820 .3780	.340	.525	.471 .451	107,000	77,500
32	1	1.510 1.470	1.305	.9990 .9985	.9990 .9980	.9930 .9860	.300	.436 .420	.060 .045	5/64 x 37°	1.0000-12 UNJF-3A	.5100 .5040	.460	.682	.618 .598	140,000	100,900

lisi AEROSPACE
hi-shear corporation
2600 SKYPARK DRIVE, TORRANCE, CALIFORNIA 90509 U.S.A.

GENERAL NOTES:
1. Concentricity: "A" diameter to "D" diameter within .010 FIM.
(28) 2. Dimensions are in inches and to be met after finish.
(29) 3. Surface texture per ASME B46.1.
4. Hole preparation per NAS618.
[5] Maximum "D" diameter may be increased by .0002 to allow for solid film or aluminum coating application.
[6] Broach petals removed.
7. Use HST112 for oversize replacement.
[8] After February, 21st of 2015, HI-KOTE™ 1 aluminum pigmented coating will be replaced by REACH compliant HI-KOTE™ 1 NC aluminum pigmented coating per Hi-Shear Spec. 294 on fasteners coated in European Union.
[9] After September 30th of 2015, HI-KOTE™ 4 coating per HS397 will be replaced by HI-KOTE™ 4 NC coating per HS397.

MATERIAL: 6AL-4V titanium alloy per AMS4928 or AMS4967.

HEAT TREAT: 160,000 psi tensile minimum (95,000 psi shear minimum for sizes up to 3/4; 90,000 psi shear minimum for 7/8 and larger).

FINISH:
HST12-( )-( ) = Cetyl alcohol lube per Hi-Shear Spec. 305.
(28) HST12AB( )-( ) = I.V.D. aluminum coating per BAC5315 with conversion coating (.0003-.0005 thick) per MIL-DTL-5541, Class 1A and cetyl alcohol lube per Hi-Shear Spec. 305.
[8] HST12AG( )-( ) = HI-KOTE™ 1 aluminum pigmented coating per Hi-Shear Spec. 294, with color orange on thread end, and cetyl alcohol lube per Hi-Shear Spec. 305.
[8] HST12AP( )-( ) = HI-KOTE™ 1 aluminum pigmented coating per Hi-Shear Spec. 294, and cetyl alcohol lube per Hi-Shear Spec. 305.
[8] HST12AZ( )-( ) = HI-KOTE™ 1 aluminum pigmented coating per Hi-Shear Spec. 294, with color black on thread end, and cetyl alcohol lube per Hi-Shear Spec. 305.
HST12BJ( )-( ) = I.V.D. aluminum coating per MIL-DTL-83488, Type II, Class 3, and cetyl alcohol lube per Hi-Shear Spec. 305.
[6] HST12CT( )-( ) = Color orange on thread end, and cetyl alcohol lube per Hi-Shear Spec. 305.
HST12CZ( )-( ) = Color black on thread end, and cetyl alcohol lube per Hi-Shear Spec. 305.
[8] HST12GD( )-( ) = HI-KOTE™ 1 aluminum pigmented coating per Hi-Shear Spec. 294 on threads only, and cetyl alcohol lube per Hi-Shear Spec. 305.
[9] HST12HK( )-( ) = HI-KOTE™ 4 NC aluminum coating per Hi-Shear Spec. 397.
[6] HST12K( )-( ) = Solid film lube per "Lubeco" 905.
[6] HST12MA( )-( ) = Solid film lube per KalGard RA.
HST12RP( )-( ) = Phosphate fluoride treat with color orange on thread end, and cetyl alcohol lube per Hi-Shear Spec. 305.
HST12RS( )-( ) = Phosphate fluoride treat, solid film lube per AS5272, Type I, and color orange on thread end.
HST12RV( )-( ) = Phosphate fluoride treat, HI-KOTE™ 2 solid film lube per Hi-Shear Spec. 292, and cetyl alcohol lube per Hi-Shear Spec. 305.
[8] HST12SU( )-( ) = HI-KOTE™ 1 aluminum pigmented coating per Hi-Shear Spec. 294, with color light blue on thread end, and cetyl alcohol lube per Hi-Shear Spec. 305.
HST12TB( )-( ) = HI-KOTE™ 2 solid film lube per Hi-Shear Spec. 292, and cetyl alcohol lube per Hi-Shear Spec. 305.
HST12UV( )-( ) = Surface coating per Hi-Shear Spec. 306, Type II, HI-KOTE™ 2 solid film lube per Hi-Shear Spec. 292, and cetyl alcohol lube per Hi-Shear Spec. 305.
HST12WF( )-( ) = Surface coating per Hi-Shear Spec. 306, Type I, color blue, with color black on thread end, and cetyl alcohol lube per Hi-Shear Spec. 305.
HST12YW( )-( ) = HI-KOTE™ 2 solid film lube per Hi-Shear Spec. 292 on threads only, with color white on thread end and cetyl alcohol lube per Hi-Shear Spec. 305.

SPECIFICATION: HI-LITE™ Product Specification 380.

CODE: First dash number indicates nominal diameter in 1/32nds. Second dash number indicates maximum grip in 1/16ths. See Finish note for explanation of code letters.

HOW TO ORDER
(28) **EXAMPLE:** Pin Part Number
HST12AP8-8
- 8/16 or 1/2 Maximum Grip Length
- 8/32 or 1/4 Nominal Diameter Pin
- Finish Code
- Pin Basic Part Number

HST12

DRAWING NUMBER
HST12 2 of 2

11 APPENDIX C – K_T CALCULATION

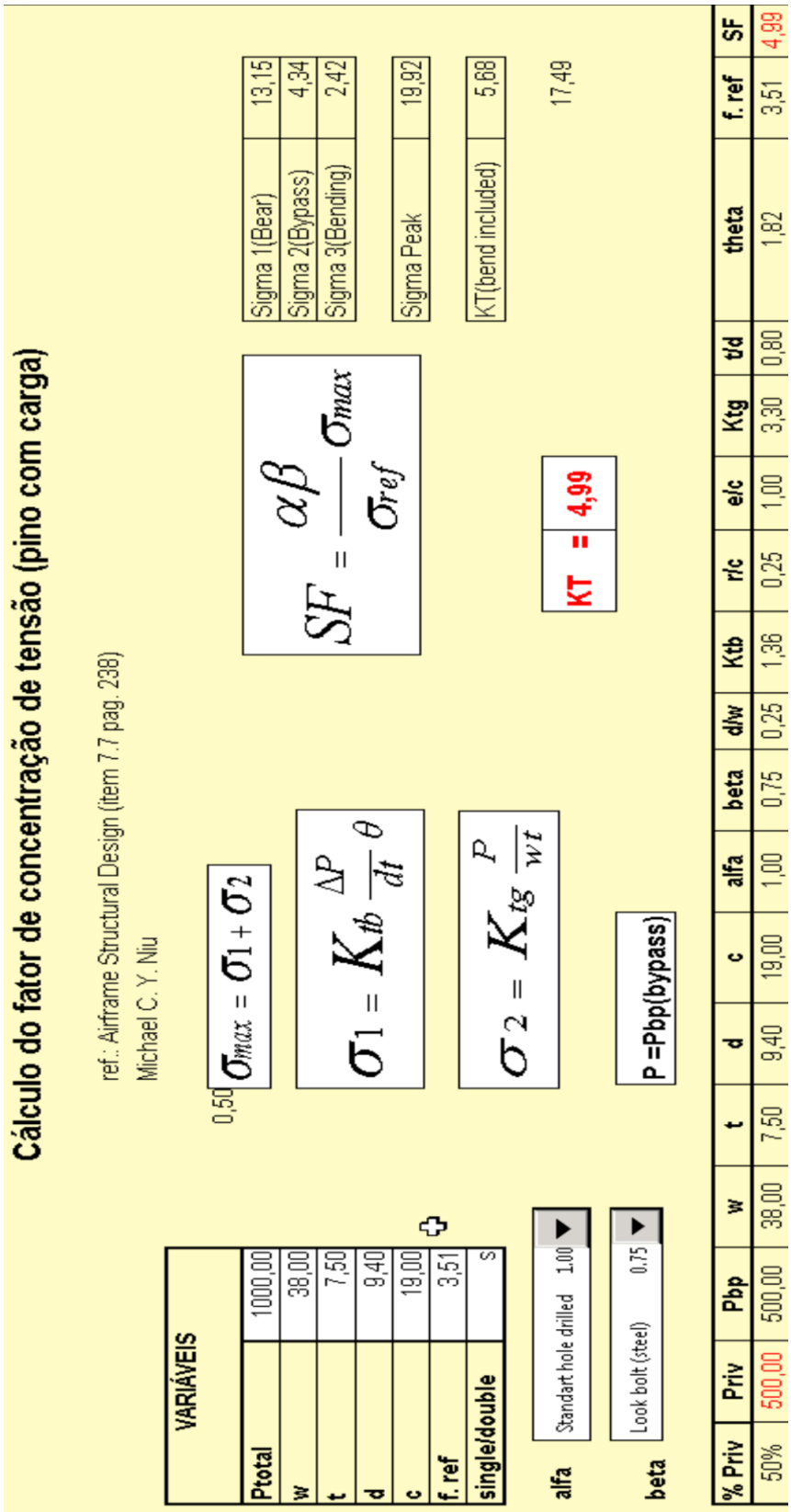

12 APPENDIX D – LOAD CALCULATION

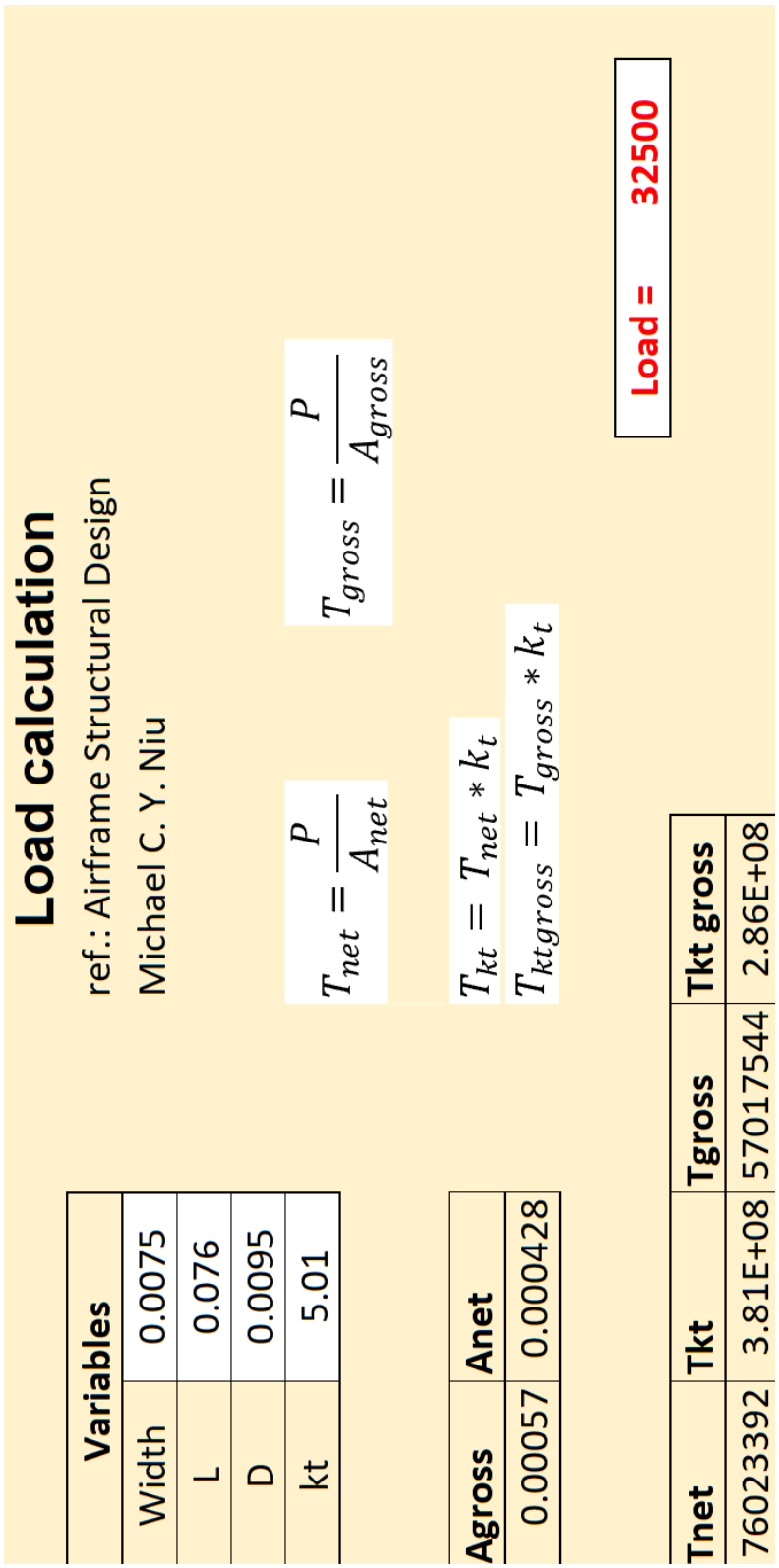

Variables	
Width	0.0075
L	0.076
D	0.0095
kt	5.01

Agross	Anet
0.00057	0.000428

Tnet	Tkt	Tgross	Tkt gross
76023392	3.81E+08	57017544	2.86E+08